

Winter 2009

# A computational study on novel carbon-based lithium materials for hydrogen storage and the role of carbon in destabilizing complex metal hydrides

Mohammed Minhaj Ghouri  
*Louisiana Tech University*

Follow this and additional works at: <https://digitalcommons.latech.edu/dissertations>



Part of the [Materials Science and Engineering Commons](#)

---

## Recommended Citation

Ghouri, Mohammed Minhaj, "" (2009). *Dissertation*. 473.  
<https://digitalcommons.latech.edu/dissertations/473>

This Dissertation is brought to you for free and open access by the Graduate School at Louisiana Tech Digital Commons. It has been accepted for inclusion in Doctoral Dissertations by an authorized administrator of Louisiana Tech Digital Commons. For more information, please contact [digitalcommons@latech.edu](mailto:digitalcommons@latech.edu).

A COMPUTATIONAL STUDY ON NOVEL CARBON-BASED  
LITHIUM MATERIALS FOR HYDROGEN STORAGE  
AND THE ROLE OF CARBON IN  
DESTABILIZING COMPLEX  
METAL HYDRIDES

by

Mohammed Minhaj Ghouri, B.Tech.

A Dissertation Presented in Partial Fulfillment  
of the Requirements for the Degree  
Doctor of Philosophy

COLLEGE OF ENGINEERING AND SCIENCE  
LOUISIANA TECH UNIVERSITY

March 2009

UMI Number: 3351360

### INFORMATION TO USERS

The quality of this reproduction is dependent upon the quality of the copy submitted. Broken or indistinct print, colored or poor quality illustrations and photographs, print bleed-through, substandard margins, and improper alignment can adversely affect reproduction.

In the unlikely event that the author did not send a complete manuscript and there are missing pages, these will be noted. Also, if unauthorized copyright material had to be removed, a note will indicate the deletion.

**UMI**<sup>®</sup>

---

UMI Microform 3351360

Copyright 2009 by ProQuest LLC.

All rights reserved. This microform edition is protected against unauthorized copying under Title 17, United States Code.

ProQuest LLC  
789 E. Eisenhower Parkway  
PO Box 1346  
Ann Arbor, MI 48106-1346

LOUISIANA TECH UNIVERSITY

THE GRADUATE SCHOOL

01/15/2009

Date

We hereby recommend that the dissertation prepared under our supervision  
by Mohammed Minhaj Ghouri

entitled "A COMPUTATIONAL STUDY ON NOVEL CARBON-BASED  
LITHIUM MATERIALS FOR HYDROGEN STORAGE AND THE  
ROLE OF CARBON IN DESTABILIZING COMPLEX METAL HYDRIDES"

be accepted in partial fulfillment of the requirements for the Degree of  
Doctor of Philosophy

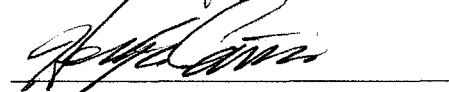
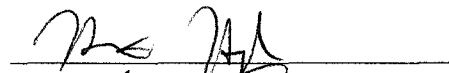
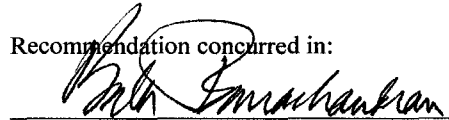


Supervisor of Dissertation Research

Head of Department  
Engineering

Department

Recommendation concurred in:



Advisory Committee

Approved:

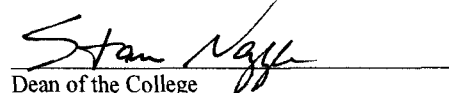


Director of Graduate Studies

Approved:



Dean of the Graduate School



Dean of the College

## **ABSTRACT**

One of the major impediments in the way of the realization of hydrogen economy is the storage of hydrogen gas. This involves both the storage for stationary applications as well as that of storage onboard vehicles for transportation applications. For obvious reasons, the system targets for the automotive applications are more stringent. There are many approaches which are still being researched for the storage of hydrogen for vehicular applications. Among them are the high pressure storage of hydrogen gas and the storing of liquid hydrogen in super insulated cryogenic cylinders. While both of them have been demonstrated practically, the high stakes of their respective shortcomings is hindering the wide spread application of these methods. Thus different solid state storage materials are being looked upon as promising solutions. Metal hydrides are a class of solid state hydrogen storage materials which are formed by the reaction of metals or their alloys with hydrogen. These materials have very good gravimetric storage densities, but are very

stable thermodynamically to desorb hydrogen at room temperatures. Research is going on to improve the thermodynamics and the reaction kinetics of different metal hydrides.

This dissertation tries to address the problem of high thermodynamic stability of the existing metal hydrides in two ways. First, a novel carbon based lithium material is proposed as a viable storage option based on its promising thermodynamic heat of formation. Pure beryllium (Be) clusters and the carbon-beryllium (C-Be) clusters are studied in detail using the Density Functional Theory (DFT) computational methods. Their interactions with hydrogen molecule are further studied. The results of these calculations indicate that hydrogen is more strongly physisorbed to the beryllium atom in the C-Be cluster, rather than to a carbon atom. After these initial studies, we calculated the geometries and the energies of more than 100 different carbon based lithium materials with varying amounts of hydrogen. A detailed analysis of the heats of reactions of these materials using different reaction schemes is performed and based on the promising thermodynamic and gravimetric storage density,  $\text{LiC}_4\text{Be}_2\text{H}_5$  is divulged as a promising novel carbon based lithium material.

In the later part, this dissertation performs a detailed study on the effect of carbon when it is used as a dopant in four different well known complex hydrides, lithium beryllium hydride ( $\text{Li}_2\text{BeH}_4$ ), lithium borohydride ( $\text{LiBH}_4$ ), lithium aluminum hydride ( $\text{LiAlH}_4$ ) and sodium borohydride ( $\text{NaBH}_4$ ). Initially, the unit cells of the crystal structure are fully resolved using the plane-wave pseudopotential implementation of DFT. The supercells of each of these are then constructed and optimized. Varying amounts of carbon is introduced as impurity in these crystals in different sites such as the top, subsurface and the bulk of the crystal lattice. Using the electronic structure calculations, it is established that (i) C-Be-H, C-B-H or C-Al-H compounds are formed respectively in the cases of  $\text{Li}_2\text{BeH}_4$ ,  $\text{LiBH}_4$  and  $\text{LiAlH}_4$  when carbon is doped in them (ii) and carbon dopant causes a decrease in the bond strengths of Be-H, B-H and Al-H in respective cases. This reduction in the bond strengths combined with the fact that there is a decrease in the ionic interaction between the cation and the anionic hydride units of these complex hydrides causes a destabilization effect.

## APPROVAL FOR SCHOLARLY DISSEMINATION

The author grants to the Prescott Memorial Library of Louisiana Tech University the right to reproduce, by appropriate methods, upon request, any or all portions of this Dissertation. It is understood that "proper request" consists of the agreement, on the part of the requesting party, that said reproduction is for his personal use and that subsequent reproduction will not occur without written approval of the author of this Dissertation. Further, any portions of the Dissertation used in books, papers, and other works must be appropriately referenced to this Dissertation.

Finally, the author of this Dissertation reserves the right to publish freely, in the literature, at any time, any or all portions of this Dissertation.

Author Mohammed Yinkaj Ghawli

Date 02/20/2009



## **DEDICATION**

*In the name of God, the one who is endlessly merciful and boundlessly bountiful.*

I dedicate this dissertation  
to my beloved father Mohammed Yousuf Ghouri  
who could not be here this day to share this happiness  
and to my mother Asiya Yousuf.

## TABLE OF CONTENTS

ABSTRACT .....	iii
DEDICATION .....	vii
LIST OF TABLES .....	xiii
LIST OF FIGURES .....	xv
ACKNOWLEDGEMENTS .....	xix
CHAPTER 1 .....	1
INTRODUCTION .....	1
1.1 Hydrogen Economy .....	2
1.1.1 Hydrogen as a Fuel .....	4
1.1.2 Hydrogen Storage .....	5
1.1.2.1 High pressure gas tank .....	9
1.1.2.2 Liquid hydrogen .....	9
1.1.2.3 Solid state storage .....	10
1.1.2.3.1 Carbon nanostructures .....	11
1.1.2.3.2 Metal hydrides .....	13
1.1.2.3.3 Novel ideas .....	15
1.2 Importance of Atomistic Simulation and Study of Clusters to Propose New Materials .....	17
1.3 Organization of Remaining Chapters .....	20
CHAPTER 2 .....	22
METAL HYDRIDES .....	22

2.1	Formation and Thermodynamics of Metal Hydrides .....	23
2.2	Types of Metal Hydrides .....	25
2.2.1	Conventional Metal Hydrides .....	25
2.2.2	Complex Metal Hydrides .....	26
2.2.2.1	Alانات .....	27
2.2.2.2	Amides .....	30
2.3	Thermodynamic Destabilization of Complex Hydrides .....	32
2.4	Role of Carbon and its Related Materials in Hydrogen Storage by Metal Hydrides .....	36
CHAPTER 3 .....		39
METHODOLOGY .....		39
3.1	Quantum Chemical Methods .....	40
3.1.1	Schrödinger's Equation for a Many-Body Problem .....	40
3.1.2	Variational Principle and the Matrix Formulation .....	43
3.1.3	Hartree-Fock Model and the Self-Consistent Field (SCF) Theory .....	46
3.1.4	Density Functional Theory (DFT) Methods .....	52
3.1.4.1	Exchange and correlation functionals .....	59
3.1.5	Plane-Wave Pseudopotential Implementation of DFT. ....	61
3.2	Classical Molecular Dynamics .....	65
3.3	<i>Ab Initio</i> Molecular Dynamics .....	68
3.4	Monte Carlo Techniques .....	72
CHAPTER 4 .....		74
STRUCTURE AND ENERGETICS OF NEUTRAL BE <sub>N</sub> (N=1-17) CLUSTERS: A DENSITY FUNCTIONAL THEORY STUDY .....		74

4.1	Introduction .....	75
4.2	Methods .....	81
4.3	Results .....	84
4.3.1	Structure of $Be_n$ ( $n=2-17$ ) Clusters.....	88
4.3.1.1	$Be_n$ ( $n=2-4$ ) clusters.....	88
4.3.1.2	$Be_n$ ( $n=5-10$ ) clusters.....	89
4.3.1.3	$Be_n$ ( $n=10-17$ ) clusters.....	93
4.3.2	Stability of Ground State Beryllium Clusters ....	97
4.3.2.1	Binding energy and second difference in energy .....	98
4.3.2.2	HOMO-LUMO gaps, vertical IPs, EAs .....	101
4.4	Conclusions .....	104
CHAPTER 5	.....	106
GEOMETRY AND STABILITY OF $BE_N C_M$ ( $N=1-10$ ; $M=1, 2, \dots$ , TO 11- $N$ ) CLUSTERS .....		106
5.1	Introduction .....	106
5.2	Methodology .....	113
5.3	Results and Discussion .....	114
5.3.1	Ground State Conformations and Isomers .....	114
5.3.2	Stability of Ground State Clusters .....	115
5.3.2.1	Binding energy and second difference in energy .....	115
5.3.2.2	HOMO-LUMO gap, vertical IPs and EAs .....	123
5.3.2.3	Magic numbers .....	126
5.4	Conclusions .....	128

CHAPTER 6 .....	130
THE INTERACTIONS OF C-BE CLUSTERS WITH HYDROGEN AND NOVEL C-BE BASED LITHIUM METAL HYDRIDES .....	130
6.1 Introduction .....	131
6.2 Methodology .....	133
6.3 Results and Discussion .....	135
6.3.1 Interaction of Hydrogen Molecule with C-Be Clusters .....	135
6.3.2 Novel Li-C-Be Materials for Hydrogen Storage ...	136
6.4 Conclusions .....	140
CHAPTER 7 .....	142
DESTABILIZATION OF $\text{Li}_2\text{BeH}_4$ COMPLEX HYDRIDE BY CARBON DOPING .....	142
7.1 Introduction .....	142
7.2 Methodology .....	148
7.2.1 Theory Level .....	148
7.2.2 Calculation Parameters .....	148
7.2.3 <i>Ab Initio</i> MD parameters .....	149
7.2.4 Bond Nature .....	149
7.2.5 Bond Population Analysis .....	150
7.3 Results and Discussion .....	151
7.3.1 Crystal Structure of Pristine $\text{Li}_2\text{BeH}_4$ .....	151
7.3.2 Modified $\text{Li}_2\text{BeH}_4$ with a Single Carbon Dopant ....	154
7.3.3 $\text{Li}_2\text{BeH}_4$ with Two Carbon Dopant Atoms .....	162
7.3.4 <i>Ab Initio</i> Molecular Dynamics .....	163
7.4 Conclusions .....	164

CHAPTER 8 .....	166
DESTABILIZATION OF OTHER COMPLEX HYDRIDES BY CARBON DOPING AND THE THERMODYNAMICS OF DESTABILIZED REACTIONS.	166
8.1 Introduction .....	166
8.2 Methodology .....	172
8.3 Results and Discussion .....	173
8.3.1 Pristine Crystal Structures .....	173
8.3.1.1 LiBH <sub>4</sub> structure .....	173
8.3.1.2 NaBH <sub>4</sub> structure .....	176
8.3.1.3 LiAlH <sub>4</sub> structure .....	177
8.3.2 Modified Hydrides with a Single Carbon Dopant ..	178
8.3.3 Thermodynamics of Destabilized Reactions .....	182
8.4 Conclusions .....	185
CHAPTER 9 .....	187
CONCLUSIONS AND FUTURE WORK .....	187
9.1 Conclusions .....	187
9.2 Future Work .....	189
REFERENCES .....	191

## LIST OF TABLES

Table 1.1-A US DOE targets for hydrogen storage materials. ....	7
Table 4.3-A Total energies and their spin multiplicity states for $\text{Be}_n$ clusters ( $n=1$ to 17).....	85
Table 5.3-A Calculated $\Delta_2E(m)$ , homo-lumo gap (Gap), $\text{IP}_v$ , and $\text{AE}_v$ for $\text{Be}_n\text{C}_m$ ( $n=1-10$ ; $m=1, 2, \dots$ to $11-n$ ) clusters. Clusters are ordered according to $\Delta_2E(m)$ from the most (bold) to the least stable in terms of $E_b$ for decreased $N (=n+m)$ value. ....	118
Table 6.3-A Heats of formation of some of the reaction schemes examined. ....	138
Table 7.3-A Substitution energies in different layers of $\text{Li}_2\text{BeH}_4$ . ....	156
Table 7.3-B Different bond lengths when the carbon atom is in different layers in the $8*(\text{Li}_2\text{BeH}_4)$ supercell lattice. ....	158
Table 7.3-C Overlap bond populations and bond lengths of important bonds in the presence of a carbon dopant. ....	161
Table 8.3-A Substitution energy required in different layers of $\text{LiBH}_4$ . ....	180
Table 8.3-B Different bond lengths when the carbon atom is in different sites in the $(\text{LiBH}_4)*8$ lattice. ....	181

Table 8.3-C $\Delta H$ values and the desorption temperatures at equilibrium pressure of 1 bar for $\text{LiBH}_4$ , with and without carbon dopant. ....	184
Table 8.3-D $\Delta H$ values and the desorption temperatures at equilibrium pressure of 1 bar for $\text{NaBH}_4$ , with and without carbon dopant. ....	184



## LIST OF FIGURES

Figure 1.1-1	Classification of various hydrogen storage materials. ....	8
Figure 2.1-1	Pressure-Concentration-Isotherm/Temperature (PCT) and Van't Hoff plot for a hydrogen absorbent. Figure adapted from reference [46]. ....	24
Figure 2.3-1	Generalized enthalpy diagram illustrating destabilization through alloy formation upon dehydrogenation. ....	33
Figure 3.1-1	Schematic showing the self-consistent iterative procedure of a Kohn-Sham calculation. ....	58
Figure 4.3-1	Ground state structures of $Be_n$ ( $n=2-11$ ) clusters with important bond lengths in angstroms. ....	86
Figure 4.3-2	Ground state structures of $Be_n$ ( $n=12-17$ ) clusters with important bond lengths in angstroms. ....	87
Figure 4.3-3	Plot for binding energy per atom ( $E_b$ /atom) versus the cluster size $n$ for $Be_n$ clusters, $n=2-17$ . ....	99
Figure 4.3-4	Plot for second difference of energies versus the cluster size for $Be_n$ clusters, $n=2-17$ . ....	100
Figure 4.3-5	Plot of HOMO-LUMO gaps versus the cluster size for $Be_n$ clusters, $n=2-17$ . ....	102
Figure 4.3-6	Plot of vertical ionization potentials versus the cluster size for $Be_n$ clusters, $n=1-17$ . ....	104

- Figure 5.3-1 Binding energy per atom as a function of the cluster size  $N (=n+m)$  for  $\text{Be}_n\text{C}_m$  ( $n=1-10$ ;  $m=1, 2, \dots, \text{to } 11-n$ ) clusters. .... 117
- Figure 5.3-2  $n$  vs.  $N$  for the highest and lowest  $\Delta_2E(m)/n$  according to Table 5.3-A. .... 121
- Figure 5.3-3 Second difference in energy per beryllium atom,  $\Delta_2E(m)/n$ , vs. number of beryllium atoms,  $n$ , for odd total number of atoms in the cluster,  $N=n+m$ . .... 122
- Figure 5.3-4 Same as Figure 5.3-3 for even total number of atoms in the cluster. .... 123
- Figure 5.3-5 HOMO-LUMO gaps as a function of number of atoms in the cluster ( $N=n+m$ ) for  $\text{Be}_n\text{C}_m$  ( $n=1-10$ ;  $m=1, 2, \dots, \text{to } 11-n$ ) neutral clusters. .... 124
- Figure 5.3-6 Vertical ionization potential,  $\text{IP}_v$ , as functions of  $N (=n+m)$  for all the  $\text{Be}_n\text{C}_m$  ( $n=1-10$ ;  $m=1, 2, \dots, \text{to } 11-n$ ) neutral ground state clusters. .... 125
- Figure 5.3-7 Vertical electron affinity,  $\text{EA}_v$ , as functions of  $N (=n+m)$  for all the  $\text{Be}_n\text{C}_m$  ( $n=1-10$ ;  $m=1, 2, \dots, \text{to } 11-n$ ) neutral ground state clusters. .... 126
- Figure 6.3-1 The behavior of hydrogen when it is placed on top of C (above) vs when it is placed on top of Be (below). Bond lengths are in Angstroms. Mulliken charge and Isodensity surfaces of each are also depicted. .... 136
- Figure 6.3-2 Ground states of some of the lithium based materials studied. .... 137
- Figure 6.3-3 Crystal structure of  $\text{LiC}_4\text{Be}_2\text{H}_5$  structure. .... 140

- Figure 7.3-1 2x2x1 supercell of  $\text{Li}_2\text{BeH}_4$ , its calculated lattice parameters compared to the reported experimental parameters for  $\text{Li}_2\text{BeD}_4$  [278]. Purple atoms in the lattice structure are Li, solid green structures are  $\text{BeH}_4$  tetrahedra with H atoms in white at the ends. .... 152
- Figure 7.3-2 (a) Total and Partial DOS of  $\text{Li}_2\text{BeH}_4$  (b) Electron density maps of  $\text{Li}_2\text{BeH}_4$ . .... 154
- Figure 7.3-3  $\text{Li}_2\text{BeH}_4$  crystal structure when carbon atom is placed in the top surface of the crystal. Distorted tetrahedra near the bulky brown atom show the elongation in the Be-H bond. .... 157
- Figure 7.3-4 Region of interest in the crystal lattice of Figure 7.3-2 (a) before and (b) after the simulation. .... 159
- Figure 7.3-5 Total and partial DOS when carbon is doped in the top layer of  $\text{Li}_2\text{BeH}_4$  lattice... 160
- Figure 7.3-6 Carbon in the (a) surface/subsurface, (b) subsurface/bulk, and (c) surface/bulk in the  $\text{Li}_2\text{BeH}_4$  crystal Lattice. Distorted tetrahedra represent  $\text{BeH}_4$  units with elongated Be-H bonds. .... 163
- Figure 8.3-1 Unit cell of  $\text{LiBH}_4$ , its calculated lattice parameters compared to the experimental parameters. .... 174
- Figure 8.3-2 (a) Total/Partial DOS of  $\text{LiBH}_4$  (b) Electron density Maps for  $\text{LiBH}_4$ . .... 175
- Figure 8.3-3 Unit cell of  $\text{NaBH}_4$ , its calculated lattice parameters compared to the reported experimental parameters. .... 177
- Figure 8.3-4 Unit cell of  $\text{LiAlH}_4$ , its calculated lattice parameters compared to the reported experimental parameters. .... 178

- Figure 8.3-5  $\text{LiBH}_4$  crystal structure when carbon atom is placed in the top surface of the crystal. Purple atoms are Li, solid green structures are  $\text{BH}_4$  tetrahedra with H atoms in white at the ends, carbon atom is the bulky brown atom. Elongated B-H bonds are highlighted. .... 181
- Figure 8.3-6 Van't Hoff Plots for destabilized  $\text{LiBH}_4$  system. .... 183
- Figure 8.3-7 Van't Hoff Plots for destabilized  $\text{NaBH}_4$  system. .... 183

## **ACKNOWLEDGEMENTS**

*"The one who does not thank people has not (properly)  
thanked God."*

*-Prophet Muhammad*

I would like to express my most sincere gratitude to my advisor, Dr. Daniela Mainardi, for her tireless dedication to her students and for her excellent guidance and mentorship. My Ph.D work with her taught me among other things, the importance of values such as patience and having faith in others, for which I will be forever thankful to her.

I would also like to thank my advisory committee member, Dr. Bala Ramachandran, for his excellent support throughout my graduate student life. The quantum chemistry classes that I took with him gave me a stronger understanding of the research in this field. I would like to also thank my other committee members Dr. Tabbetha Dobbins, Dr. Henry Cardenas and Dr. Hisham Hegab for their time and their invaluable suggestions. I also had very fruitful discussions with Dr. Pedro Derosa. I thank him for the guidance and the books he provided me. I thank all the

faculty members at Louisiana Tech, with whom I may or may not have taken any course, for their service to the solemn profession of teaching. Education is a gift they have given me which, I hope will remain with me forever.

Financial support provided by different bodies such as Louisiana Tech College of Engineering and Science (COES), National Science Foundation (Grant No. DMR 0414903), Louisiana Board of Regents (Grant LEQSF(2007-08)-ENH-TR-46) and the computational facility support by Louisiana Optical Network Initiative (LONI) are gratefully acknowledged.

I thank my entire past and present research group members. It was very pleasant to work with all of them. At the same time, it helped me immensely by improving the scope of my learning. My friends at Islamic Center of North Louisiana where I resided for last five years became an extended family which made the stay in Ruston, away from my own family, less painful. I express my heartfelt gratitude and thanks to all of them.

I would like to thank my family for their unyielding support and patience in general and especially while I have been studying for my doctoral degree. I started my Ph.D with the permission and blessings of my father Mohammed Yousuf Ghouri and by the time I ended it, he has left us for an eternal life in a heavenly abode. I miss sharing

this moment of immense pleasure with him. The one thing that I cherish the most is the tireless efforts of my mother Asiya Yousuf in raising us brothers. I thank her very sincerely for that and for all her prayers for me. My brothers Mohammed Wahaj Ghouri, Mohammed Eraj Ghouri, Mohammed Meraj Ghouri and Mohammed Siraj Ghouri are all my pillars of support. I thank them wholeheartedly for being so understanding.

Above all, I thank God almighty copiously for giving me guidance throughout my life and for making me capable of obtaining this honor of a doctorate degree. Nothing was within my reach without His help, as He mentions in the Quran (10:49): "Say: I have no power over any harm or profit to myself except as God willeth."

## **CHAPTER 1**

### **INTRODUCTION**

Hydrogen is believed to be a fuel that could resolve all of the issues that we are struggling with due to the present layout of the energy demand and consumption associated with the fossil fuel based economy [1-3]. One of the reasons for this inclination towards Hydrogen, as senator Tom Harkin mentions in his foreword for Peter Hoffman's book on Hydrogen energy, is that "solar, wind and most other renewable energy sources are intermittent and regional." [4] The other reason for a prejudice towards hydrogen among the alternative sources of energy is that it is "arguably the most commercially viable option." [3] Thus the interest among the experts in an economy which is driven by hydrogen as a primary energy carrier, rather than oil has been on a constant rise in the last couple of decades. In this introductory chapter we talk about this alternative approach to the generation of energy. We present the definition and the details of hydrogen economy. We discuss the problems posed by the storage of hydrogen



onboard vehicles so that it can be used as a fuel for the transportation applications. The subsequent sections in this chapter are arranged as follows. Section 1.1 presents the definition of the hydrogen economy. Section 1.1.1 describes the merits of hydrogen as a fuel and presents the problems involved in its real world application. Section 1.1.2 and its subsections, in considerable detail broach upon one of the problems involved with the hydrogen economy, which is its storage on board vehicles for automotive applications. This is the main application targeted by this work. Sections 1.1.2.1 and 1.1.2.2 discuss briefly the gaseous and liquid storage of hydrogen. Section 1.1.2.3 and its subsections discuss the various solid state storage techniques being researched. Section 1.2 addresses the need for the use of atomistic calculations in the design of novel storage materials. Section 1.3 discusses the organization of remaining chapters in this dissertation.

## **1.1 Hydrogen Economy**

Hydrogen economy [1-25] is defined as "the industrial system in which one of the universal energy carriers is hydrogen." [5] It has to be clearly assimilated at this point, that hydrogen is merely an energy carrier [6] (and

not an energy source) just like electricity is a carrier of energy and not a source [3]. One obvious implication of hydrogen being an energy carrier (and not source) is the fact that it needs to be produced from other energy sources. Hydrogen can be produced from a range of different alternative sources like gasoline, natural gas, methane, solar, etc. Thus the usage of hydrogen as energy carrier is expected to be only as clean (environmentally) as the source used to produce it.

As with any other fuel, even hydrogen fuel has combustible properties and it has to be handled with due care. But in comparison with contemporary fuels like natural gas, gasoline and methane, in some respects hydrogen is safer [7]. Physicist Amory Lovins, cofounder and CEO of Rocky Mountain Institute, in his report on twenty hydrogen myths [8] says while talking about the myths about the hydrogen safety that "hydrogen is generally as safe as natural gas or LPG, and is arguably inherently safer than gasoline." [8] This is demonstrated by the fact that, due to its extremely buoyant properties (hydrogen is 14.4 times lighter than air and natural gas is only 1.7 times lighter than air), hydrogen diffuses quickly and it is rather difficult to build up sufficient concentration of hydrogen for it to be flammable. Hydrogen is quite

difficult to detonate in air and even when hydrogen gas is leaked, it is far more likely to burn than to explode [8]. It is worthy here to note the 1994 study conducted by the researchers at the Sandia National Laboratories on the hydrogen vehicle safety report that states "there is abundant evidence that hydrogen can be handled safely, if its unique properties - sometimes better, sometimes worse and sometimes just different from other fuels - are respected." [7]

#### **1.1.1 Hydrogen as a Fuel**

Hydrogen is the first and the lightest element of the periodic table. It is a colorless, odorless gas and in terms of the abundance of availability, it is the most abundantly available element in nature [3,9] and it accounts for around 75% of the universe mass [1,10]. Most of this hydrogen does not occur freely in the nature, but it is found in combination with other elements like carbon, oxygen and nitrogen. To be able to use hydrogen as a fuel, it needs to be split from these other elements. The calorific value of a fuel is the yardstick used to measure the efficiency of a fuel. This is defined as the amount of heat produced by the combustion of fuel at the standard condition of temperature and pressure (STP) which are in IUPAC's standards, a temperature of 0°C and an absolute

pressure of 100 kPa. Hydrogen gas has the highest calorific value of 150 kJ/g among all the fuels (compared to the values of 33 kJ/g for charcoal, 50 kJ/g for petrol, 55 kJ/g for methane) [11]. The way in which hydrogen is envisaged to be used as a fuel, particularly for transportation applications is, by employing an internal combustion engine which can burn hydrogen directly [12] or a hydrogen fuel cell [3,13]. Of these two alternatives, a clear bent of experts is towards the generation of electricity using a hydrogen fuel cell. Fuel cell is an electrochemical device that in principle operates like a battery. It combines hydrogen with oxygen to form water (as a byproduct) and in this process creates usable electricity power. Therefore, it would not be inappropriate to say that hydrogen when used as a fuel is perfectly clean on environment as it only produces completely unharmed water as the byproduct.

### **1.1.2 Hydrogen Storage**

Storage of hydrogen is the primary subject that is attempted to be addressed in this dissertation. This is a highly vibrant research field with innovative ideas and techniques being proposed by different researchers at regular intervals. The applications in which hydrogen can be used as a fuel and which might require the need for its storage can be very broadly classified into a stationary

application or a transportation/non-stationary application [14]. The instances for the stationary type of applications are the cooling and heating of our houses and the examples of non stationary applications are the driving of our cars, trucks and vehicles. These applications have completely different sets of requirements with a much more rigorous set of demands for the transportation applications. This can be expected because for transportation, the hydrogen storage must comply within particular size limits, operate near room temperature and pressure conditions, and supply hydrogen for a drive range of 300 miles [14]. The term 'hydrogen storage' in this project and whenever mentioned subsequently in this report is used to imply the meaning 'hydrogen storage for transportation applications'. The United States Department of Energy (DOE) [14] has set certain criterion, known as 'system targets' to be satisfied within different time frames for the successful storage material. These are summarized in the Table 1.1-A.

Table 1.1-A US DOE targets for hydrogen storage materials.

<b>Storage Parameters</b>	<b>2010</b>	<b>2015</b>
Gravimetric Capacity	0.060 kg H <sub>2</sub> /kg	0.090 kg H <sub>2</sub> /kg
Volumetric Capacity	0.045 kg H <sub>2</sub> /liter	0.081 kg H <sub>2</sub> /liter
Storage system cost	\$4 /kWh energy	\$2 /kWh energy
Refueling rate	1.5 kg H <sub>2</sub> /minute	2.0 kg H <sub>2</sub> /minute

The vividness of these storage requirements can be clearly delineated in one's perception only when one clearly comes to terms with the following facts about hydrogen gas at STP. At room temperature and pressure conditions, 1 gram of hydrogen occupies a volume of 11 liters. This fact in conjunction with the reality that 1 kg of hydrogen is required to provide the same chemical energy as 1 gallon of gas [12] illustrates the difficulty for the storage of pure hydrogen for vehicular applications. A tank to store enough hydrogen for a drive range of 300 miles [14] has to be of the size of many football fields. By the same token, a storage tank of comparative size of present cars with that amount of hydrogen is an enormous challenge in terms of the gravimetric and volumetric storage densities. Figure 1.1-1 shows the broad classification of

the various hydrogen storage methods and techniques available at present. None of these materials completely satisfy the requirements outlined above and dynamic research is going on to improve the performance characteristics of all these methods. The different techniques can be divided broadly into three types depending on whether the stored hydrogen is in the form of a gas, liquid and solid. The solid state storage materials can be further classified into different categories. Sections 1.1.2.3.1 through 1.1.2.3.3 briefly address each of these materials.

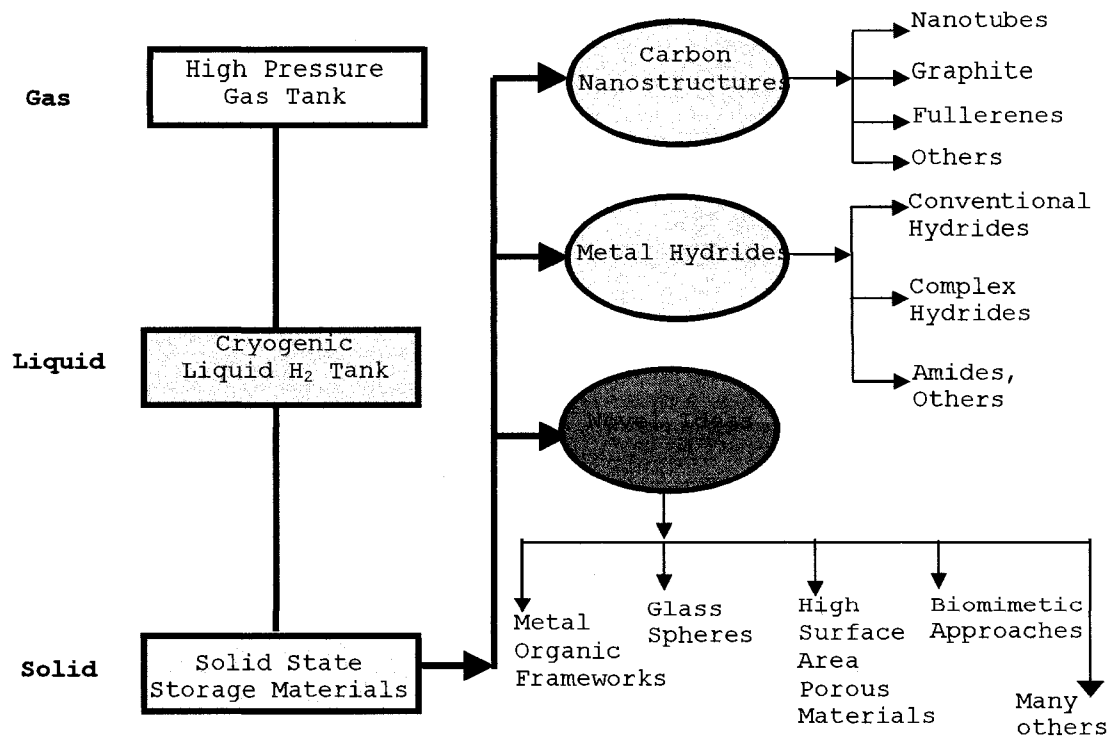


Figure 1.1-1 Classification of various hydrogen storage materials.

### **1.1.2.1 High pressure gas tank**

As mentioned earlier, at atmospheric pressure of 1 atm and ambient temperature of 298 K, it requires a volume of 60 m<sup>3</sup> to store 5 kg of H<sub>2</sub> [15]. Contrary to this, the same amount of gas at the same temperature occupies a volume of mere 0.2 m<sup>3</sup> when it is pressurized into a 35 MPa composite tank. Thus, due to its conceptual simplicity and technical viability high-pressure tank is the most commonly available storage method presently [12,16]. Very strong and Ultra-light composite materials are now being developed to store hydrogen up to pressures as high as 80 MPa [16]. Even when this technique has been practically demonstrated for transportation applications in projects such as Clean Urban Transport for Europe (CUTE) [17] and Daimler-Benz NECAR II [18], safety concerns are limiting the extensive usage of this technology. Also under such high pressures, the gravimetric density is very low. Another facet to consider in this method is the amount of work necessary for the compression of hydrogen gas which is of the order of 2.21 kWh per kg of gas when it is compressed from 0.1 MPa to 80 MPa [16].

### **1.1.2.2 Liquid hydrogen**

The boiling temperature of hydrogen is -253 °C. Hydrogen occurs as a liquid below this temperature. This



liquid hydrogen has higher energy density than its gaseous form. Super insulated cryogenic tanks, known as cryostats can be used to store liquid hydrogen. This technique has also been demonstrated practically both in the road transport (BMW limited series of cars) [14,17] and the space travel [18,19]. Even this method could have been accepted as the staple method for storage of hydrogen onboard vehicles lest it has some inherent drawbacks associated with it. Safety of this kind of tanks in practical usage is a concern that this technique shares in common with high pressure gas storage tanks. Two other issues characteristic of liquid storage are (i) tremendous amount of energy required in the liquefaction of hydrogen gas, which is listed as almost one-third of the energy value of stored hydrogen [14]. This drastically reduces the efficiency of this method and (ii) continuous evaporation of the liquid, despite being stored in exotic super insulated cryogenic tanks, which is referred to as boil-off. Liquid hydrogen storage cannot be expected to gain a status of most reliable storage method until these two disadvantages are effectively tackled.

#### **1.1.2.3 Solid state storage**

The above two methods (high pressure gas storage and liquid hydrogen storage) discussed in Sections 1.1.2.1 and

1.1.2.2 respectively have already been demonstrated prototypically in the industry. But the built-in hindrances of each of these techniques have motivated the study of different types of solid state storage techniques. There are different ways of storing hydrogen using a solid state storage material including metal and complex hydrides [20], carbon nanostructures like fullerenes and nanotubes [16], and many more novel ideas that have been recently proposed and investigated, like metal organic frameworks [21]. These solid state storage materials are anticipated to be easily implementable in the fuel cell vehicles and be safer than the two methods in the preceded discussion [22]. Each of this material and their storage properties as well as the latest state-of-the art in each of these highly vigorous research fields is discussed in Sections 1.1.2.3.1 through 1.1.2.3.3.

#### **1.1.2.3.1 Carbon nanostructures**

The discovery of unique carbon based materials like fullerenes in 1985 [23] and nanotubes in 1991 [24] has ignited interests in a diverse range of technological applications [25,26]. Among the major of these is the onboard hydrogen storage application. This is due to the high surface area and porosity of these materials [27]. The phenomenon called physisorption, the basis of which lies in

the Van der Waals interaction between gases and solids is the reason for the storage of hydrogen in carbon based materials. Dillon et al. [28] were the first group that initiated the study of hydrogen storage in these materials. The interest in these materials started with a highly optimistic tone with the initial reports like Rodriguez et al. [29] reporting even upto 67 wt% storage capacities in graphitic nanofibres. These results could never be reaffirmed by any other group, but they succeeded in sparking an active concern in the carbon materials for storage applications. Since then different carbon nanostructures like single wall carbon nanotubes SWNTs, multi wall nanotubes MWNTs, fullerenes, graphene, activated carbons, graphitic nanofibers, nanohorns, etc. have been proposed as prospective storage materials. Over the last five years, chemical activators in these materials known as heteroatoms are used, rather than pure carbon materials to enhance the adsorption capacity [30-32]. A 2006 review by Strobel et al. [22] presents a nice summary of the research done till date in this field. A brief reading of this review reveals a number of obvious conclusions, some of which are discussed below. First, a lot of efforts have already been committed into the investigation of various types of carbon nanomaterials. Second, the storage capacities reported for

a wide range of temperatures and pressures is devoid of consistency. Third, a set of results reported by a group could never be reproduced by any other group. Finally, a broad range of heteroatoms are also experimented with, without any promise of approaching the DOE targets. One of the reasons that have been cited for such diversity in the reported results for hydrogen storage is the differences in the purity of the samples used by the different groups. Also, from Strobel et al. [22] review, it is heartening to see that majority of the results paint a less hopeful picture with respect to carbon materials as an envisioned onboard hydrogen storage material.

#### 1.1.2.3.2 Metal hydrides

Hydrogen is a highly reactive element [33]. When it is passed over metals and alloys, a solid hydride solution is formed [33]. These are called the metal hydrides. During the process of formation of hydrides, molecular hydrogen breaks into its atomic form and these atoms get trapped in the host metal lattice. This hydrogen can be retrieved back under favorable conditions of temperature and pressure. Hence this is considered a reversible storage method. Metal Hydrides can be broadly divided into two categories. They are (i) the conventional metal hydrides [14] and (ii) the complex metal hydrides [16]. The conventional metal

hydrides are very well characterized and are in the form of  $MH_x$ , where M is a transition metal or an intermetallic alloy of the form of AB,  $AB_2$ ,  $AB_5$  or  $A_2B$  [14]. An example of the application of these types of hydrides is demonstrated by Daimler-Benz which, in early 1980s used a hydride tank of Fe-Ti alloy to fuel a car [34]. The problem in the wide spread practical usage of this technique is the low gravimetric storage capacity due to heavy weight of the tank of this hydride [35]. The other types of hydrides are the complex hydrides [16]. The difference between both these classes is that in complex hydrides, there "is the transition to an ionic or covalent compound of the metals upon hydrogen absorption." [16] The examples of these types of hydrides are the well known classes like alanates formed by the anionic group  $[AlH_4]^-$  and borates formed by other anionic group  $[BH_4]^-$ . In the last few years a new class of hydrides called amides/amines is proposed. These can be categorized into a separate class altogether because of the immense amount of interest in them in a relatively short time. A more thorough review of all these materials is attempted in Chapter 2 on related research in metal hydrides.

### 1.1.2.3.3 Novel ideas

Due to a host of reasons like (i) increase in the detrimental environmental effects and the immediate outcry to curb them and (ii) the growth of funding from governmental agencies in the recent past, a formidable growth in the proposal and research of different innovative materials for hydrogen storage is seen. A few important among these are discussed in this section.

Metal organic frameworks [21,36-39] or MOFs for short are quickly gaining ground as a reliable hydrogen storage material. MOFs, which are formed as a "result of the polymerization of metal ions with organic connectors" [38] are light weight, stable microporous solid materials which due to their high porosity and surface area, are expected to exhibit high H<sub>2</sub> sorption behavior. Many different sites like, organic linker site [38], open metal site [39] etc. are the adsorption sites for hydrogen in a MOF. There can also be ways to modify the adsorption sites so as to enhance the hydrogen uptake capacity of a MOF in general. According to the results published by Rowsell et al. [37] they use inelastic neutron scattering experiments to prove that there are specific sites in MOFs where hydrogen gets adsorbed. The two most common sites are the top site and the edge site of the organic linker molecule. The edge site

for the adsorption of hydrogen is considered to be particularly weak, and therefore if the physisorption of  $H_2$  near the edge site is improved by some means, the total uptake capacity of hydrogen can be improved so that it achieves the DOE requirements. Buda et al. [38] study the different models like 'one ring model' (benzene), 'two ring models' (naphthalene) and extended models ( $C_6H_4(COOH)_2$ ) for the adsorption of hydrogen at different sites like top site and the edge site. They found out that the hydrogen molecule gets adsorbed on the top site with its axis toward the center of the plane. This site was found relatively to be the stronger binding site by 2 kJ/mol. Sagara et al. [36] report the results of quantum chemistry calculations on  $H_2$  binding by the MOF-5. MOF-5 is the crystal MOF that consist of  $Zn_4O$  cluster connected by 1,4-benzenedicarboxylate (BDC) linker. Density Functional Theory is used to calculate the atomic positions, charges and lattice constant. This group also used the *ab initio* techniques to study the binding energy of  $H_2$  to benzene and  $H_2$ -BDC- $H_2$ . They have estimated the binding energies of 4.77 kJ/mol for benzene and 5.27 kJ/mol for BDC. They have also performed the Monte Carlo simulations at high temperatures and have observed many binding sites in MOF-5 at 300 K. Thus even though MOFs are quickly gaining prominence among

the researchers, a lot of ground needs to be covered before they can be implemented in the practical usage of the fuel cell vehicles.

Porous Walled - Hollow Glass Microspheres (PW-HGM) [40] are also contending materials for the storage of hydrogen on board vehicles. HGMs are porous microballoons with a diameter smaller than that of a human hair. The wall permeability of these glass spheres is increased by heating them. If a flow of hydrogen is introduced at this instance, the hydrogen molecules diffuse through the thin and porous walls of microspheres. After this, the spheres are cooled so that the gas gets trapped inside these balloons. The hydrogen is released whenever it is needed by reheating these spheres. However, this approach also has its share of limitations. One of these limitations is the poor thermal conductivity of a packed bed of glass spheres. This poor conduction of heat translates to unsuitably low release rates of hydrogen gas [41].

## 1.2 Importance of Atomistic Simulation and Study of Clusters to Propose New Materials

As has been discussed in Section 1.1 and its subsections, a successful hydrogen storage material needs to gratify a host of extremely challenging demands. It is



indeed an ambitious asking. The successful design of such a material calls for a symbiosis of both theory and experimentation. Theoretical computation in the present age is not just applied to understand experimental results, but also to guide them. The recent advances in theory and their implementation in the recent years have lent to the vistas in the approaches towards the design of new hydrogen storage materials.

One of the advantages of using the computational approaches to address a problem is that, unlike experiments, these help by shedding light on the physics and chemistry of the interactions at a broad range of different size scales from nano level to microscopic to bulk. Computational modeling provides a clearer perception into the interdependence of the size and the surface interactions of nanostructured materials such as clusters. This gives us more information into hydrogen bonding nature and the hydrogen binding energies thereby aiding us to tailor and test novel materials for hydrogen storage. By this we mean that theory provides us ways to delineate between ionic and covalent bonding between hydrogen and different types of materials such as carbon nanostructures or complex metal hydrides. Also this type of information

helps in the control of the thermodynamics and kinetics of the release of hydrogen from the storage material.

Design of novel storage materials is only possible by a detailed bottom-up analysis and this, in return, calls for a detailed study of the atomic clusters of the involved systems. In the recent past there has been a shift of the researchers towards meeting this requirement. Kiran et al. [42] have very recently studied aluminum-hydrogen clusters  $Al_nH_m$  using the electronic shell closure criteria and formulated a rule of selection, known as the 'magic rule' [43]. According to these authors, this rule provides criteria for the search of  $Al_nH_m$  clusters with magic properties that might have great potential in applications like hydrogen storage and high energy-density materials.

Due to the prominence of looking into clusters for better understanding the storage properties, Watari et al. [44] had earlier performed a detailed theoretical study on the storage of hydrogen in palladium clusters. They calculated the configurational entropy change for  $\alpha$  to  $\beta$  transition in bulk  $PdH_{0.6}$  by assuming the different hydrogen configurations of  $Pd_{13}H_8$ . Also there is a patent filed titled "Nanostructured materials for hydrogen storage," [45] where the inventors design clusters of the type  $XH$  and  $XH_2$  where  $X=C, Si, Ge$ . Thus looking at the chemistry and the

stability of the constituent clusters is among the primaries on the road to a better understanding and the development of hydrogen storage materials.

### **1.3 Organization of Remaining Chapters**

All efforts have been put in this dissertation so that its content is presented in a way that should be completely clear and self explanatory to the readers. Chapter 1 is an introduction to the work performed in this project. Given the immense gravity of the presently in-vogue fossil fuel economy, it discusses hydrogen economy that can be employed to defuse the looming ill consequences of their continual usage. It also discusses some challenges such as the storage of hydrogen that are impediments to the practical implementation of hydrogen economy. And also, chapter 1 discusses the validity of the usage of atomistic simulations to design novel storage materials. Chapter 2 presents a literature review on metal hydrides, which are the materials that are being researched in this work.

This dissertation is a modeling and simulation work and Chapter 3 discusses the computational tools and techniques that are used to perform them. Chapter 4 presents the results on pure beryllium atomic clusters we have studied. We first discuss the stability and the

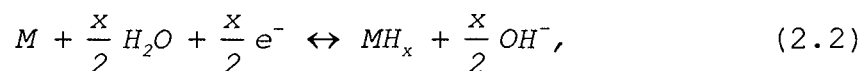
electronic properties of pure beryllium clusters  $\text{Be}_n$  from  $n = 1$  to 17. In Chapter 5, we then move on to discuss the clusters of the type  $\text{Be}_n\text{C}_m$  ( $n=1-10$ ;  $m=1, 2, \dots$ , to  $11-n$ ). We present the results on the stability of these clusters and also the electronic properties like HOMO-LUMO gap, vertical ionization potential. These are discussed in terms of the possible 'magic clusters'. These clusters are further studied in the presence of hydrogen molecule in Chapter 6. Then we study the different possible lithium-beryllium-carbon hydrogen storage materials depending upon their heats of formation. In Chapter 7, we present the detailed results of the *ab initio* calculations on introducing the carbon dopant in the known light metal hydride  $\text{Li}_2\text{BeH}_4$ . In Chapter 8, we extend the type of calculations we performed on  $\text{Li}_2\text{BeH}_4$  to three other complex hydrides lithium borohydride  $\text{LiBH}_4$ , sodium borohydride  $\text{NaBH}_4$ , lithium aluminum hydride  $\text{LiAlH}_4$  and also look into the thermodynamics of these metal hydrides.

Finally, in Chapter 9 we present the conclusions that come out of this work and also discuss the future work that can be performed in this direction.

## CHAPTER 2

### METAL HYDRIDES

Among the solid state hydrogen storage materials discussed in the previous chapter, metal hydrides are an integral part. In fact, one of the most intensively studied materials for this application are the metal hydrides [20]. Hydrogen is a highly reactive element and it generally reacts with metals, intermetallic compounds, alloys and forms solid solutions of metal hydrides. Hydrogen atoms in these (interstitial) metal hydrides [16] are trapped at the interstitial sites inside the metal host lattice, similar to lattice defects. Under favorable conditions of temperatures and pressures, these hydrogen atoms can be retrieved back and hence the metal hydrides are considered as good reversible storage options. There are two possible ways of hydriding a metal. These are direct dissociative chemisorption and electrochemical splitting of water with their respective reactions as shown in eqs. 2.1 and 2.2 [20,33].



where  $M$  represents the metal.

## 2.1 Formation and Thermodynamics of Metal Hydrides

There are generally two phases in the formation of metal hydrides.  $\alpha$ -phase is the phase when only some hydrogen is absorbed by the metal host and  $\beta$ -phase is the one at which hydride is fully formed. When starting from the metal, the external hydrogen pressure can be gradually increased to load the sample with hydrogen. In the diluted solution  $\alpha$ -phase, a large pressure increase is needed to induce higher hydrogen content. At certain equilibrium hydrogen pressures the two phases coexist and the  $\beta$ -phase will grow at the cost of  $\alpha$ -phase. Again after the complete formation of the hydride, a large increase in the pressure is needed to induce higher hydrogen content. The pressure at which this phase transition takes place at a given temperature is called as plateau pressure of equilibrium between two phases. Figure 2.1-1 shows a pressure-concentration-isotherm plot for hydrogen absorbent and also a Van't Hoff plot in the right. This equilibrium pressure  $P$

as a function of temperature is related to the changes in entropy  $\Delta S^\circ$  and enthalpy  $\Delta H^\circ$  by Van't Hoff equation given in eq. 2.3

$$\Delta G^\circ = -RT \ln K_{eq} = RT \ln \left[ \frac{P}{P_o} \right] = \Delta H^\circ - T\Delta S^\circ, \quad (2.3)$$

where  $P_o$  is the reference pressure which is typically taken as 1 bar or  $10^5$  Pa. The slope of Van't Hoff plot is a measure of the sorption enthalpy, which is directly related to the equilibrium sorption temperature at a given pressure. To achieve a hydrogen equilibrium desorption temperature in the range of 373-473 K at  $10^5$  Pa hydrogen pressure, the corresponding desorption enthalpy should be in the range of 48-61 kJ per mole of  $H_2$  [46].

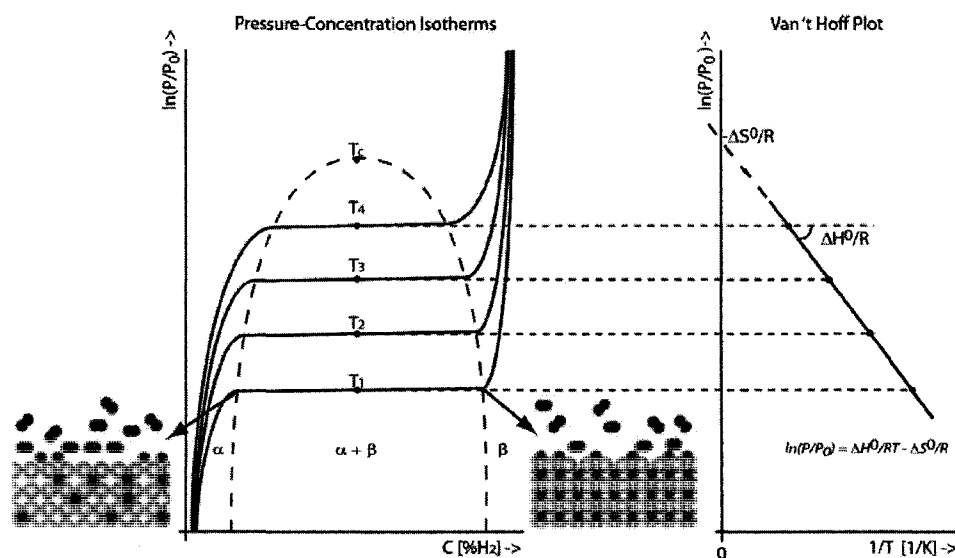


Figure 2.1-1 Pressure-Concentration-Isotherm/Temperature (PCT) and Van't Hoff plot for a hydrogen absorbent. Figure adapted from reference [46].

## 2.2 Types of Metal Hydrides

Metal hydrides can be broadly divided into two main classes. They are (i) conventional metal hydrides and (ii) complex metal hydrides.

### 2.2.1 Conventional Metal Hydrides

Conventional hydrides can be further divided into binary or ternary hydrides. The binary metal hydride compounds of the type  $MH_x$ , are generally formed by electropositive transition metals and their alloys [16]. The metallic hydrides of intermetallic compounds (the simplest of them being ternary hydrides of the type  $AB_nH_x$ ) are especially interesting because the variation of the elements allows tailoring of the properties of the hydrides. The element  $A$  is usually a rare earth or an alkaline earth metal and element  $B$  is often a transition metal. The examples of these type of hydrides are  $LaNiH_6$ ,  $ZrV_2H_{5.5}$ ,  $CeNi_3H_4$ ,  $Mg_2NiH_4$ , etc [16]. One of the features of these materials that are an important reason for such high amount of interest in them is their extremely high volumetric density.  $LaNi_5H_6$  [47-51], for example, reaches a volumetric density of  $115 \text{ kg m}^{-3}$ . Most of these conventional metallic hydrides absorb hydrogen up to a hydrogen to metal ratio of  $H/M=2$ . Greater  $H/M$  ratios of up to 4.5 (e.g.  $BaReH_9$  [52]) have been tried, however all hydrides with a  $H/M$



ratio of  $>2$  are ionic or covalent compounds and belong to the class of complex hydrides (see Section 2.2.2). Most of the transition metals and their intermetallic alloys provide a very efficient way for storing large amounts of hydrogen in a safe and compact way. However due to the heavy weight of these transition metals and their intermetallic compounds, they have a very limited gravimetric density of  $<3$  wt%  $H_2$ .

### **2.2.2 Complex Metal Hydrides**

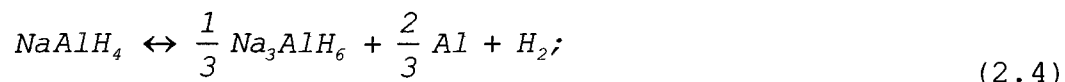
The other class of metal hydrides is the complex hydrides [16,53-55]. These are the metal-hydrogen complexes formed by the first, second and third group light elements such as lithium, sodium, beryllium, boron, etc. The main contrasting factor of complex hydrides from the above mentioned metallic hydrides is their transition to an ionic or covalent compound of the metals upon hydrogen absorption. Over the last decade or so, there has been an enormous growth in the research of these materials. The reason for this is that these represent a good compromise between gravimetric hydrogen content (due to the light weight of these metals), desorption temperature and reaction enthalpy [56]. Complex hydrides were previously studied only in the context of releasing the hydrogen via hydrolysis. Although hydrolysis reaction of a complex

hydride increases the amount of released, it essentially transforms the hydride into an unusable and irreversible byproduct. This is not an acceptable situation for a hydrogen storage material. One of the reasons for a recent surge in the study of these complex hydride systems is the proposal of a number of catalysts by different research groups that facilitate the reversible release of hydrogen from them.

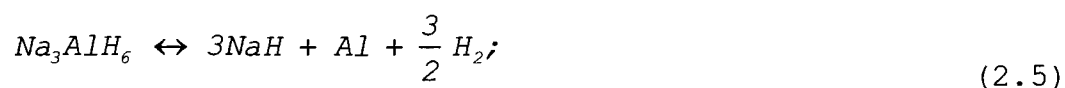
#### **2.2.2.1 Alanates**

The well known examples of complex hydride systems are the classes of alanates or the tetrahydroaluminates  $M(\text{AlH}_4)$ , boranes (also known as borohydrides or tetrahydroborates)  $M(\text{BH}_4)$ , amides  $M(\text{NH}_2)$ , where M is a group one, two or three light elements such as Li, Mg, Na, etc. In these hydrides the hydrogen content reaches a maximum of 18.5 wt% for  $\text{LiBH}_4$ , which is highly favorable for onboard hydrogen storage applications in terms of gravimetric requirements for such applications. However the practical usage of these systems is hampered because of both kinetic and thermodynamic limitations in these [20]. Different catalysts were then doped into these which proved to be two-fold facilitators for the complex hydride systems. First is that the use of catalysts made the use of these complex hydrides affordable as reversible materials as

opposed to their previous mode of application - hydrolysis which rendered them completely irreversible [57]. The other grounds on which catalysts proved beneficial were that they reduced the thermodynamic stability and also improved their kinetics in ways that the practical application of these systems seemed to be within reach. For instance, Bogdanović and Schwickardi [58,59] evidenced that upon doping sodium aluminum hydride  $\text{NaAlH}_4$  with  $\text{TiO}_2$ , its dehydriding kinetics enhanced and the stability reduced with the temperature for decomposition getting lowered. A more detailed study [60] on these catalyzed systems by the same group reported that the decomposition of  $\text{NaAlH}_4$  takes place in two reactions as shown in eqs. 2.4 and 2.5 at a hydrogen pressure of 2 bar and temperature of 60 °C (dissociation enthalpy and the amount of hydrogen released reversibly is shown for each reaction in the parentheses).



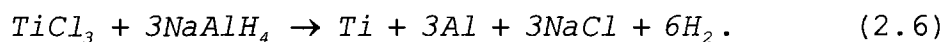
$$(\Delta H = 37 \text{kJ.mol}^{-1}, 3.7 \text{wt}\% \text{H})$$



$$(\Delta H = 47 \text{kJ.mol}^{-1}, 1.9 \text{wt}\% \text{H}).$$

These results led the way to a wave of further studies on transition metals as dopants [61-66]. Perhaps the greatest amount of efforts by different groups

internationally has been spent on transition metal doped alanates and both encouraging as well as otherwise results were reported. For instance, Sandrock et al. [61] investigated the dry-doping of  $TiCl_3$  as catalyst in sodium alanates and reported an increase in both the hydriding and rehydriding rates. Under similar conditions, they showed that the amount of hydrogen evolved from the Ti-doped  $NaAlH_4$  is about 50 times as much as that of the undoped  $NaAlH_4$ . As for the rationale that induces the improvement of thermodynamic stability and the enhancement of dehydriding kinetics in the complex hydrides, there are differing opinions. Sun et al. [62] attributed such improvements to dopant induced lattice distortions rather than the catalytic effect. Gross et al. [63] differed with them and proposed the catalytic effects of doping materials in the enhancements kinetics of  $NaAlH_4$ . Another view [64] on the exact nature of the titanium catalyst action is the reduction of the dopant to a zerovalent state as formulated in the reaction shown in eq. 2.6.



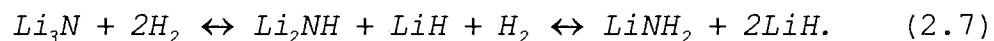
This view further obtains the support from detailed X-Ray Diffraction (XRD) and Extended X-Ray Absorption Fine Structure (EXAFS) studies on the mixtures of titanium halides and light metal hydrides [65-67]. However Al-Ti

alloy formation is yet another view.  $\text{Al}_3\text{Ti}$  or  $\text{AlTi}$  is reported to have been observed by doping  $\text{TiCl}_3$  in  $\text{LiAlH}_4$  [68],  $\text{TiCl}_4$  in  $\text{LiAlH}_4$  [69] or  $\text{TiCl}_3$  in  $\text{NaAlH}_4$  [70]. Gross et al. [71] have suggested the formation of Ti-Al phases as an important step in the dehydriding of these systems. Ti-Al-H compound formation has been also confirmed by the Density Functional Theory (DFT) calculations in our group by Dathara and Mainardi [72]. There have also been disputes in the scientific community over the more favorable dopant sites in the  $\text{NaAlH}_4$  lattice. Løvvik et al. [73] used DFT calculations and suggested native Al sites in the lattice to be favorable for Ti substitutions. Vegge's [74] DFT calculations also complement their results. Prior to this, Ñíguez et al. [75] performed combined neutron inelastic scattering studies with first principles calculations and suggested that the substitution of Ti at native Na sites is more energetically favorable. Dathara and Mainardi's [72] DFT studies suggest almost equal probability energetically for Ti substitutions both at lattice and interstitial sites.

#### **2.2.2.2 Amides**

Recently Li-N-H complex hydride systems such as lithium imide ( $\text{Li}_2\text{NH}$ ) and lithium amide ( $\text{LiNH}_2$ ) have attracted consistent attention as hydrogen storage

materials due to their enticing properties like high gravimetric densities of hydrogen [76-87]. The reversible hydriding and dehydriding reactions are shown in eq. 2.7.



The formation enthalpies for the two steps are reported to be -165 to -116 and -45 kJ/mol respectively for each step. The second step in the two-step reaction above is promising for H<sub>2</sub> storage due to its relatively small formation enthalpy and a large amount (6.5 wt%) of hydrogen [86]. However, this dehydriding reaction begins at approximately 423-473 K in vacuum and at approximately 550 K in argon [87]. One way proposed for lowering this temperature is by partial cation (Li<sup>+</sup>) substitution by different valence cations with larger electro-negativities (such as Mg<sup>+</sup>) [81,83-86]. The beginning and ending temperatures for the hydrogen desorption reaction from LiNH<sub>2</sub> are lowered by about 50 K by the partial substitution of Li by Mg [80,87,88]. Zhang et al. [86] in their electronic structure calculations have partially substituted Li by Mg, a more electronegative element and also K, a more electropositive element and report that Mg substitution is more effective in destabilization of NH<sub>2</sub> in LiNH<sub>2</sub>. TiCl<sub>3</sub> catalyst was also used by Ichikawa et al. [79] during ball-milling of the LiNH<sub>2</sub> and LiH mixture. They reported 5.5 wt%

storage and also a high reaction rate with positive effect on kinetics. They also report that addition of  $\text{TiCl}_3$  in these compounds can help to completely prevent the formation of ammonia which is one of the major concerns in the practical usage of N-based storage materials. Even a small amount of ammonia, if it is formed would poison the polyelectrolyte membrane of the conventional PEM fuel cells that are being used these days [55].

### **2.3 Thermodynamic Destabilization of Complex Hydrides**

As we have seen in the discussion on complex metal hydrides in Section 2.2 and its subsections, thermodynamic restrictions levied by the light weight complex hydrides is one of the main handicaps that prevent their implementation in the transportation applications. One of the approaches applied to address this issue is due to the work of Reilly and Wiswall [89,90] in late 1960's. They showed that it is possible to modify the thermodynamics of hydrogenation and dehydrogenation reactions by using additives to form new compounds or alloys during dehydrogenation that are energetically favorable respective to the products of the reaction without additives [91]. Researchers have named this technique as destabilization. The enthalpy diagram for this process is shown in Figure 2.3-1.

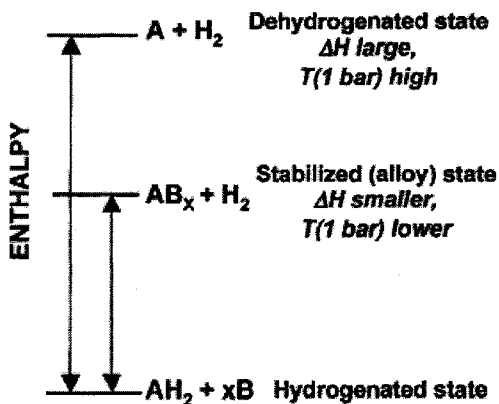


Figure 2.3-1 Generalized enthalpy diagram illustrating destabilization through alloy formation upon dehydrogenation.

Vajo and co-workers first applied this concept experimentally in their work on light metal hydrides like  $\text{MgH}_2$  and  $\text{LiH}$  [92]. They showed that these two hydrides can be destabilized by the reaction with Si and the dehydrogenation temperatures reduced.  $\text{Li}_{2.35}\text{Si}$  and  $\text{Mg}_2\text{Si}$  alloys were reported to be formed during this process respectively for  $\text{LiH/Si}$  and  $\text{MgH}_2/\text{Si}$  systems [92]. Another study came out later from the same group where they showed that upon using  $\text{MgH}_2$  as an additive, the hydrogenation and dehydrogenation enthalpy of  $\text{LiBH}_4$  reduced by 25 kJ/mol of  $\text{H}_2$  [93]. Pinkerton et al. [94], Aoki et al. [95] and Noritake et al. [96] then tried to destabilize  $\text{LiBH}_4$  with  $\text{LiNH}_2$ . Leng et al. [84] synthesized magnesium amide  $\text{Mg}(\text{NH}_2)_2$



and then studied its destabilization reaction with LiH. The same reaction was further studied by other groups [97-99]. Ichikawa et al. [97] report that the ball-milled mixture of  $\text{Mg}(\text{NH}_2)_2$  with LiH stores 7 mass% of hydrogen reversibly at the temperatures of 140 to 220 °C. There have been further experimental studies by different groups on various systems in very recent past which report considerable decrease in the thermodynamic stability of hydride system and therefore hydrogenation/dehydrogenation enthalpies [100].  $\text{LiBH}_4$  was destabilized by  $\text{MgH}_2$ ,  $\text{MgF}_2$ ,  $\text{MgS}$ ,  $\text{MgSe}$  by Vajo et al. [101] recently. They report that for the  $\text{LiBH}_4/\text{MgH}_2$  system, the reversible storage of around 10 wt% is attained with an equilibrium hydrogen pressure approximately 10 times greater than the pressure for pure  $\text{LiBH}_4$  [101]. A ternary mixture comprising of  $\text{LiNH}_2 + \text{LiBH}_4 + \text{MgH}_2$  is studied and a set of novel hydrogen storage reactions proposed by Yang et al. [102]. This group shows that by starting with this ternary mixture rather than other binary mixtures,  $\text{Mg}(\text{NH}_2)_2 + 2\text{LiH} \leftrightarrow \text{Li}_2\text{Mg}(\text{NH})_2 + 2\text{H}_2$ , a reaction previously known can proceed at lower temperatures and improved kinetics with improved reversibility. While there is a marked improvement in the thermodynamics of destabilized reactions, the problem of slow hydrogen sorption kinetics is addressed by Barison et al. [103] in their report on

$\text{LiNH}_2/\text{MgH}_2$  destabilized system by introducing catalysts such as  $\text{Nb}_2\text{O}_5$ ,  $\text{TiCl}_3$  and graphite. Vajo et al. in their work on destabilized  $\text{LiBH}_4/\text{MgH}_2$  system, used various catalytic additives such as  $\text{TiCl}_2$ ,  $\text{TiF}_3$ ,  $\text{CrCl}_3$ ,  $\text{NdCl}_5$ ,  $\text{VCl}_3$  [101]. They report that best results in terms of kinetics are observed by the use of 3%  $\text{TiCl}_3$ . Lim et al. [104] in their investigation on dehydrogenation behavior of  $\text{LiBH}_4/\text{CaH}_2$  system with small amount of  $\text{NbF}_5$  as catalyst report the equilibrium dehydrogenation temperature under a hydrogen pressure of 1 bar to be 309 °C with a reaction enthalpy change of 56.5 kJ/mol of  $\text{H}_2$ . Pinkerton and Meyer [105] report the same system  $\text{LiBH}_4/\text{CaH}_2$  with a small amount of  $\text{TiCl}_3$  to store 9.1 wt% hydrogen and an estimated reaction enthalpy of 59 kJ/mol of  $\text{H}_2$ .

There is also no dearth of theoretical works reported on the concept of destabilization. Alapati et al. [91] have used first principles Density Functional Theory (DFT) calculations to predict the reaction enthalpies for more than 100 different destabilization schemes and have identified a number of reactions that have very promising properties in terms of both their reaction enthalpies and their hydrogen storage capacity. In their preceding study [106], they have used the phonon frequency calculations with in DFT to calculate the vibrational entropy

contributions in the free energy change ( $\Delta G$ ) for the reactions which show promise in their earlier work [91]. In another study by the same group, they use DFT to report that mixtures of  $\text{ScH}_2 + \text{LiBH}_4$  releases 8.9 wt%  $\text{H}_2$  at an equilibrium hydrogen pressure of 1 bar at around 330 K. Velikokhatnyi et al. [107] have performed *ab initio* DFT study on the reaction  $\text{Mg}(\text{NH}_2)_2 + 2\text{LiH} \rightleftharpoons \text{Li}_2\text{Mg}(\text{NH})_2 + 2\text{H}_2$  and compared it to the experimental study. Cho et al. [108] have in their work used the CALPHAD approach to thermodynamically evaluate the possibility of destabilizing the high temperature binary ionic hydrides and ternary complex hydrides by reacting them with other light elements or other hydrides. They observe significant decrease in the decomposition temperatures for  $\text{MgH}_2 + \text{Si}$ ,  $\text{LiBH}_4 + \text{MgH}_2$ ,  $\text{LiBH}_4 + \text{Al}$  and  $\text{LiH} + \text{Si}$  systems with not so significant decrease in the decomposition temperatures for  $\text{MgH}_2 + \text{Al}$  and  $\text{NaBH}_4 + \text{Al}$  systems [108].

#### 2.4 Role of Carbon and Its Related Materials in Hydrogen Storage by Metal Hydrides

Carbon and its related compounds, as discussed in the previous chapter, are another class of materials that are very widely researched solid state hydrogen storage materials. The interest in these compounds initiated with a

report on hydrogen storage in single wall carbon nanotubes (SWNT) by Dillon et al. [28] who stated that the hydrogen molecules get physisorbed on the carbon related compounds due to the high surface area and the porosity of these materials [27]. Even before the research in the line of this field started, Imamura and group had proposed the application of nano-composites obtained by ball milling of graphitic form of carbon and magnesium with organic additives such as benzene, cyclohexane and tetrahydrofuran as hydrogen storage materials [109-115]. Based on this group's observation that co-milling graphite with magnesium improves its hydrogen absorption kinetics, Dal Toè et al. [116] for the first time employed carbon/graphite for the first time as a catalyst with  $MgH_2$  and analyzed the phase analysis by XRD and also measured its desorption behavior. They observed that the milling of  $MgH_2$  with graphite improved its desorption rate kinetics. Ritter's group then used graphite as a co-dopant in titanium doped  $NaAlH_4$  and measured the dehydrogenation and hydrogenation kinetics with temperature programmed desorption [117]. They found that co-doping of 2 mol% Ti-doped  $NaAlH_4$  with 10wt% graphite improved the kinetics of both the dehydriding reaction of  $NaAlH_4$  by lowering the dehydrogenation temperature over the range of 90 °C - 150 °C by as much as 15 °C [117]. Dehouche

et al. [118] studied the hydrogen charge and discharge characteristics and the stability of Ti/Zr-doped NaAlH<sub>4</sub> composites ball milled with carbon additives such as activated carbon, graphite and single wall carbon nanotubes SWNTs. They observed that carbon additives are good catalysts which can improve the hydrogen absorption and desorption properties. Their results show that, in comparison with Ti/Zr-doped NaAlH<sub>4</sub> without carbon additives, the hydriding and dehydriding kinetics of SWNT/catalyzed NaAlH<sub>4</sub> are enhanced by a factor of four [118]. Pukazhselvan et al. [119] have also investigated the hydrogen storage behavior of NaAlH<sub>4</sub> doped with different molar percentages of CNTs and have noted that NaAlH<sub>4</sub> with 8 mol% CNTs is the optimum material which has 3.3 wt% storage capacity and it exhibits desorption characteristics at 160 °C [119].

## **CHAPTER 3**

### **METHODOLOGY**

In Chapter 3, we discuss the various methods and techniques applied in the work related to this dissertation. This project being a computer simulation work, the computational physics and chemistry theories underlying the procedures employed to obtain these results are briefly addressed. Solid state systems like crystals are a major part of this work and thus an attempt is made here for an abbreviated address to the ways of dealing these kind of systems computationally. While trying to discuss these theories in considerable clarity, it is intended to keep the usage of mathematical equations to a minimum.

An overwhelmingly high percentage of this work is performed using a technique known as the Density Functional Theory (DFT). Before the details of DFT are presented, it is intended to begin with a brief discussion of quantum chemistry since DFT is strongly rooted in the theory of

quantum mechanical or chemical methods which describe the electronic structure in detail.

### 3.1 Quantum Chemical Methods

#### 3.1.1 Schrödinger's Equation for a Many-Body Problem

There is no alternative to quantum mechanics if it is intended to study the electronic structure and distribution in a system [120]. The aim of quantum mechanics, in contrast to classical mechanics [121] is to study very light particles like electrons. The basis of non-relativistic quantum mechanics revolves around solving what is known as Schrödinger's equation which, for molecules and solids with multiple nuclei and electrons is given in eq. 3.1

$$\hat{H} \Psi_i(\vec{r}_1, \dots, \vec{r}_n, \vec{R}_1, \dots, \vec{R}_N) = E_{tot} \Psi_i(\vec{r}_1, \dots, \vec{r}_n, \vec{R}_1, \dots, \vec{R}_N), \quad (3.1)$$

where  $\hat{H}$  is called the Hamiltonian operator for this system,  $\Psi_i(\vec{r}_1, \dots, \vec{r}_n, \vec{R}_1, \dots, \vec{R}_N)$  is the wave function of the  $i$ 'th state of the system (which depends on the  $3n$  spatial coordinates, the  $n$  spin coordinates of the electrons and the  $3N$  spatial coordinates of the nuclei) for which this equation is solved, and  $E_{tot}$  is the total energy of the system. The wave function  $\Psi_i$  contains all the information that can be known about the quantum system which is being

studied. It is worth mentioning here that the description of an electron, since it is a fermion, can be complete only with the specification of its spin coordinate which can only acquire the values of  $\pm \frac{1}{2}$ .

The Hamiltonian  $\hat{H}$  in the above equation is a differential operator representing the total energy of the system. This total energy is the sum of different kinetic and potential energy terms as shown in the eq. 3.2.

$$\hat{H} = -\frac{1}{2} \sum_{i=1}^n \nabla_i^2 - \frac{1}{2} \sum_{A=1}^N \frac{1}{N_A} \nabla_A^2 - \sum_{i=1}^n \sum_{A=1}^N \frac{Z_A}{r_{iA}} + \sum_{i=1}^n \sum_{j>i}^n \frac{1}{r_{ij}} + \sum_{A=1}^N \sum_{B>A}^N \frac{Z_A Z_B}{R_{AB}}. \quad (3.2)$$

In the sum above,  $A$  and  $B$  run over the  $N$  nuclei, while  $i$  and  $j$  denote the  $n$  electrons in the system. The first two terms are the kinetic energy terms of electrons and nuclei respectively, where  $\nabla_p^2$  is the Laplacian operator.

The remaining three terms in eq. 3.2 are the potential energy terms representing the electron-nuclei attractions, the electron-electron repulsions and the nucleus-nucleus interactions respectively. The energy of the electron whose wave function, is  $\Psi_i$ , is given by its expectation value of this Hamiltonian,  $\hat{H}$ . In the famous Dirac's bra-ket notation this is written as shown in eq. 3.3.



$$E_i = \left\langle \Psi_i \left| \hat{H} \right| \Psi_i \right\rangle. \quad (3.3)$$

For all practical purposes, it can be assumed to a very good approximation that the electrons move in the electrostatic field of fixed nuclei. The rationale for this approximation is the difference between the masses of nuclei and electrons. A typical carbon nucleus weighs more than 20,000 times its electron [122]. This famous approximation is known as the Born-Oppenheimer or adiabatic approximation. The complete Hamiltonian in eq. 3.2 is reduced to the so-called electronic Hamiltonian shown in eq. 3.4 after the invocation of the Born-Oppenheimer approximation.

$$\hat{H}_{elec} = -\frac{1}{2} \sum_{i=1}^n \nabla_i^2 - \sum_{i=1}^n \sum_{A=1}^N \frac{Z_A}{r_{iA}} + \sum_{i=1}^n \sum_{j>i}^n \frac{1}{r_{ij}}. \quad (3.4)$$

The solution of the Schrödinger's eq. 3.1 with the electronic Hamiltonian of eq. 3.4 above gives the electronic wave function  $\Psi_{elec}$  and the electronic energy  $E_{elec}$  for a particular relative orientation of the N nuclei. The total energy of the system is then given as the sum of this  $E_{elec}$  and the constant nuclear repulsion term that came out of the Hamiltonian as a part of the Born-Oppenheimer approximation. Therefore, the electronic Schrödinger's equation is reduced to as shown in eq. 3.5.

$$\hat{H}_{elec} \Psi_{elec} = E_{elec} \Psi_{elec}. \quad (3.5)$$

The total energy of the system is obtained using eq. 3.6. The  $E_{nuc}$  term in eq. 3.6 is defined below.

$$E_{tot} = E_{elec} + E_{nuc}, \quad (3.6)$$

where  $E_{nuc} = \sum_{A=1}^N \sum_{B>A}^N \frac{Z_A Z_B}{R_{AB}}$ .

### 3.1.2 Variational Principle and the Matrix Formulation

The Schrödinger's eq. 3.1 can be written in a shorthand operator form as shown in eq. 3.7

$$\hat{H} \Psi = E \Psi. \quad (3.7)$$

Or, in terms of Dirac notation this can be written as shown in eq. 3.8

$$\hat{H} |\Psi\rangle = E |\Psi\rangle. \quad (3.8)$$

From the definition of the Hamiltonian discussed in the Section 3.1.1, we know that the eq. 3.8 consists of analytic derivatives and integrals which are not the most convenient ways to express, so that they may be attempted to be solved by a computer. Thus the two fundamental concepts that facilitate all the electronic structure calculations are the matrix reformulation of this Schrödinger's equation and its transformation in the variational principle form, which makes it algorithmic or

computer friendly. These two concepts are discussed in this section briefly.

We consider the wave function as the amplitude field all over space which can be approximated as a linear combination of a finite number of well defined functions known as the basis functions. This is similar to the expansion of well behaved functions in Fourier analysis in terms of sines and cosines. Using the Dirac notation, this can be written as shown in eq 3.9

$$|\Psi\rangle = \sum_{n=1,k} C_n |\phi_n\rangle, \quad (3.9)$$

where  $C_n$  are the constant coefficients and the  $\{|\phi_n\rangle\}$  are the  $k$  orthogonal basis functions. With this approximation, our problem reduces to the finding of these finite numbers of the coefficients of basis functions. Both the sides of Schrödinger's eq. 3.8 are now multiplied with the complex conjugate of a basis function  $\phi_m^*$  and integrated all over the space. This now becomes eq. 3.10

$$\langle\phi_m|\hat{H}|\Psi\rangle = E\langle\phi_m|\Psi\rangle. \quad (3.10)$$

Substituting eq. 3.9 in eq. 3.10, we get eq. 3.11

$$\sum_{n=1,k} C_n \langle\phi_m|\hat{H}|\phi_n\rangle = EC_m. \quad (3.11)$$

The right hand side of eq. 3.11 is obtained by using the fact in our hypothesis that the basis functions are

ortho-normal. This implies that their product is zero for all the terms except when  $m=n$  and then it is one. Thus the right hand product just remains as  $EC_m$ . Equation 3.11 can now be written as eq. 3.12

$$\sum_{n=1,k} H_{mn} C_n = EC_m, \quad (3.12)$$

where,  $H_{mn}$  is a matrix,  $C_n$  is a coefficient matrix that needs to be found. Equation 3.12 written in its matrix form is shown in eq. 3.13

$$\begin{pmatrix} H_{11} & \dots & H_{1k} \\ \vdots & \ddots & \vdots \\ H_{k1} & \dots & H_{kk} \end{pmatrix} \cdot \begin{pmatrix} C_1 \\ \vdots \\ C_k \end{pmatrix} = E \begin{pmatrix} C_1 \\ \vdots \\ C_k \end{pmatrix}. \quad (3.13)$$

Equation 3.13 is derived as the matrix reformulation of the Schrödinger's eq. 3.7 or 3.1.  $H_{mn}$  are the Hamiltonian matrix elements over the two basis  $\phi_m$  and  $\phi_n$  which are just numbers. This matrix algebra problem is now very easily solvable by a computer algorithm. Thus the solutions of the Schrödinger's equation are reduced to the eigen vector  $C_n$ .

One other very powerful concept utilized in all the computational electronic structure calculations is the variational principle [122]. This is the recipe to systematically address the Schrödinger's equation so that we obtain the ground state wave function that delivers the lowest energy. We know that the expectation value of the

Hamiltonian operator  $\hat{H}$  using the wave function gives the energy of the system. The variational principle states that there is a functional  $E$  of any arbitrary function which is defined as shown in eq. 3.14 and is always greater than or equal to the ground state energy  $E_0$ .

$$E[\Phi] = \frac{\langle \Phi | \hat{H} | \Phi \rangle}{\langle \Phi | \Phi \rangle} \geq E_0 \quad (3.14)$$

The numerator in the eq. 3.14 is the expectation value of the Hamiltonian operator and the denominator is the normalization factor. If  $E[\Phi] = E_0$  then  $\Phi$  is the ground state wave function. Thus, for complex potential systems, the ground state wave function is obtained by trying a family of different wave functions, and the one which gives the lowest expectation value is divulged as the ground state with the lowest energy  $E_0$ .

### 3.1.3 Hartree-Fock Model and the Self-Consistent Field (SCF) Theory

The exact solution of the Schrödinger's equation is not mathematically possible except for few trivial molecular systems like the Hydrogen atom or a  $\text{He}^+$  ion which consist of only one electron [123]. As Dirac put it "The underlying physical laws necessary for the mathematical theory of a large part of physics and the whole of

chemistry are thus completely known, and the difficulty is only that the exact application of these laws leads to equations much too complicated to be soluble.”[123] The most difficult part in exactly solving this many-body problem is the two-body term of the Hamiltonian, which is

$\sum_{i=1}^n \sum_{j>i}^n \frac{1}{r_{ij}}$ . This is the electron-electron interaction term and

it depends on the simultaneous position of two bodies. Thus systematic approximations are introduced at this point to obtain the solutions. A significant simplification is obtained by introducing *independent-particle* models, according to which the interactions between the particles is approximated, either by neglecting all the interactions except the most important one, or by taking all interactions in an average fashion. In the *Hartree* model, each electron moves in an effective potential representing the attraction of the nuclei and the average effect of the repulsive interactions of the other electrons. This average repulsion is the electrostatic repulsion of the average charge density of all other electrons.

In this model, each electron is described by an orbital, and the total wave function is given as a product of orbitals as shown in eq. 3.15

$$\Psi(\vec{r}_1, \dots, \vec{r}_n) = \phi_1(\vec{r}_1)\phi_2(\vec{r}_2) \dots \phi_n(\vec{r}_n). \quad (3.15)$$

Thus we have  $n$  number of integro-differential equations representing each of the orbital wave functions in the eq. 3.15 and can be expressed as shown in eq. 3.16

$$\left[ -\frac{1}{2} \nabla_i^2 + \sum_{A=1}^N \frac{Z_A}{\vec{r}_{iA}} + \sum_{j \neq i} \frac{\int |\varphi_j(\vec{r}_j)|^2 d\vec{r}_j}{\vec{r}_{ij}} \right] \varphi_i(\vec{r}_i) = \epsilon \varphi_i(\vec{r}_i). \quad (3.16)$$

The third term in the Hamiltonian of eq. 3.16 represents the electrostatic potential felt by the electron in the average field of all other electrons. This each one electron wave function (the Hamiltonian of which involves the average electron charge density of all the other electrons) is solved individually. Thus this leads to the concept of self consistency. That is, to be able to solve the Schrödinger's equation for an electron, we should have the information about all the other electrons, and to be able to solve each of these, in turn requires us to have the solution of the former electron. The solution to this is achieved iteratively. An initial guess at all the orbitals is made which allows the construction of all the operators in equation 3.16 above. Thus the solution of the single-particle pseudo-Schrödinger equations is obtained. With this new set of orbitals, the new Hartree operators are formed and this iterative procedure is continued until

the results are converged. This procedure is known as 'Self-Consistent Field (SCF)' theory.

The result obtained by the Hartree model of eq. 3.15 has two inherent shortcomings in it. The first one is that it does not take into consideration electron correlation. This corresponds to the fact that, since electrons are moving at a high speed, they repel each other and this repulsion is only included as an average effect. Due to this the energy obtained by this model is always higher than the ground state energy. The second deficiency of this model is that it neglects one of the most fundamental requirements of the electronic wave functions, which is its antisymmetric nature. According to this requirement, electrons, being fermions (have half-integer spin), the wave function of a set of identical electrons should be antisymmetric by the interchange of their spatial coordinates.

$$\psi(\vec{r}_1, \vec{r}_2, \dots, \vec{r}_j, \dots, \vec{r}_k, \dots, \vec{r}_n) = -\psi(\vec{r}_1, \vec{r}_2, \dots, \vec{r}_k, \dots, \vec{r}_j, \dots, \vec{r}_n).$$

This basic requirement of antisymmetry is over come by taking what is known as the Slater's determinant, shown in eq. 3.17, of the individual orbitals rather than just a product (eq. 3.15) in Hartree's product. Therefore,



$$\psi(\vec{r}_1, \dots, \vec{r}_n) = \begin{vmatrix} \phi_\alpha(\vec{r}_1) & \phi_\beta(\vec{r}_1) & \dots & \phi_\gamma(\vec{r}_1) \\ \phi_\alpha(\vec{r}_2) & \phi_\beta(\vec{r}_2) & \dots & \phi_\gamma(\vec{r}_2) \\ \vdots & \vdots & \ddots & \vdots \\ \phi_\alpha(\vec{r}_n) & \phi_\beta(\vec{r}_n) & \dots & \phi_\gamma(\vec{r}_n) \end{vmatrix}. \quad (3.17)$$

The columns in the determinant of eq. 3.17 are single-electron wave functions, orbitals, and the electron coordinates are along the rows. Thus interchange of the coordinates is synonymous to the interchange of two rows, which leads to the same determinant, but with opposite signs. Also this determinant establishes the basic principle which is due to *Pauli*. Pauli's exclusion principle states that two electrons cannot have all quantum numbers equal. We know that the determinant vanishes when either two rows or columns are identical. Each element in this determinant is given by the Hartree-Fock eqs. 3.18

$$\begin{aligned} \psi(\vec{r}_1, \dots, \vec{r}_n) &= |\text{Slater}|, \\ \left[ -\frac{1}{2} \nabla_i^2 + \sum_{A=1}^N \frac{Z_A}{\vec{r}_{iA}} \right] \phi_\lambda(\vec{r}_i) + \\ &\left[ \sum_{\mu} \int \phi_{\mu}^*(\vec{r}_j) \frac{1}{\vec{r}_{ij}} \phi_{\mu}(\vec{r}_j) d\vec{r}_j \right] \phi_\lambda(\vec{r}_i) - \\ &\sum_{\mu} \left[ \int \phi_{\mu}^*(\vec{r}_j) \frac{1}{\vec{r}_{ij}} \phi_{\lambda}(\vec{r}_j) d\vec{r}_j \right] \phi_{\mu}(\vec{r}_i) = \epsilon \phi_\lambda(\vec{r}_i). \end{aligned} \quad (3.18)$$

The wave function generated by the Hartree-Fock (HF) model discussed above is now antisymmetric, but it still does not include all of the electron correlation effects.

That is, on an average, electrons are further apart due to their repulsions than described by the HF wave function. As mentioned above this leads to an energy which is higher than the ground state energy. This difference of energy between the HF energy and the lowest possible ground state energy is called the 'electron correlation' energy.

Hartree-Fock model forms the fundamental basis of the modern computational electronic structure calculation methods, based on which a lot of post HF methods are formulated. The examples of such methods are Møller-Plesset Perturbation theories, Configuration interaction (CI) methods and others. These methods also include a systematic way of including the electron correlation energies. There is also a separate class of methods called the *Semi-empirical* methods (such as NDDO, INDO, MINDO, etc) which start from the HF method, but as the name suggests, replace certain multi-center integrals with experimental data to simplify the computation.

There is a completely different class of electronic structure methods which are very similar to the Hartree-Fock model in their architecture, but they start from a completely different premise than these *ab initio* methods. These are called the Density Functional Theory (DFT) methods. These are based on the assumption that the energy

and consequently all other properties of a molecular system is a function of their electron charge density, rather than their wave functions. These methods are discussed in the Section 3.1.4.

#### **3.1.4 Density Functional Theory (DFT) Methods**

Density Functional Theory (DFT) methods root from the two theorems that were proved by Hohenberg and Kohn [124] in 1964. According to these theorems "there exist a universal functional of the electron charge density, such that the correct ground-state energy can be associated with it." [124] The difference between this approach and the wave function based methods discussed in the Section 3.1.3 is emphasized by the fact that a wave function for an  $N$  electron system has  $4N$  variable coordinates (three spatial and one spin for each electron), where as electron density is the square of the wave function integrated over  $N-1$  electron coordinates. This translates into a significant reduction of the computational burden in applying these methods.

Prior to the 1964 theorems, the idea of finding energy as a function of electron density dates back to the Thomas-Fermi approach of the late 1920s and the early 1930s. In this approach of formulating the energy in terms of the

density, the most difficult part of the energy expression, which is the kinetic energy density is taken to be corresponding to the kinetic energy density of the homogeneous electron gas (HEG). This is known as the Local Density Approximation (LDA). Thus the expression for energy in terms of Thomas-Fermi approach is given by eq. 3.19

$$E_{Th-Fe}[\rho] = A \int \rho^{\frac{5}{3}}(\vec{r}) d\vec{r} + \int \rho(\vec{r}) v_{\text{ext}}(\vec{r}) d\vec{r} + \frac{1}{2} \iint_{\vec{r}_{12}} \frac{\rho(\vec{r}_1)\rho(\vec{r}_2)}{\vec{r}_{12}} d\vec{r}_1 d\vec{r}_2. \quad (3.19)$$

The first term in the summation of eq. 3.19 corresponds to the kinetic energy. But this rather unrefined functional for energy is not theoretically justified. It is just a heuristic derivation. Anyhow, this idea of focusing on the charge density rather than the complex electronic wave function for detailed electronic structural analysis led to the basis of Hohenberg-Kohn theorems of 1960s.

DFT, based on Hohenberg-Kohn theorems, in contrast to Thomas-Fermi approach is an exact theory, at least in principle, that starts with proved theorems and then lists the conditions that the charge density needs to satisfy in order to completely solve the problem. The complete quantum problem is defined, as we have seen in the Section 3.1.3, by the external potential  $v_{\text{ext}}$  and the number of electrons  $N$ . All system properties, including its energy and the charge

density are derived from the wave functions obtained by the Schrödinger's equation formed by the external potential and the electron coordinates. Hohenberg-Kohn in their two theorems in 1964 proved that even the opposite is true.

In exact terms, the first of the two Hohenberg-Kohn theorems states that "The external potential  $v_{\text{ext}}$ , and hence the total energy, is a unique functional of the electron density  $\rho(r)$ ." [124] The energy functional referred to in this first theorem is given by eq. 3.20

$$E[\rho(\vec{r})] = \int \rho(\vec{r})v_{\text{ext}}(\vec{r})d\vec{r} + F[\rho(\vec{r})], \quad (3.20)$$

where  $F[\rho(\vec{r})]$  is an unknown functional (called 'universal functional') which depends only on the charge density,  $\rho(\vec{r})$ . The second theorem states that "the ground state energy can be obtained variationally: the density that minimizes the total energy is the exact ground state density." [124] This second theorem is writing out the conceptual equivalent of the Schrödinger equation for the charge density. The universal functional  $F[\rho]$  is defined as shown in eq. 3.21

$$F[\rho] = \langle \Psi | \hat{T} + \hat{V}_{e-e} | \Psi \rangle, \quad (3.21)$$

where  $\Psi$  is the ground state wave function of the external potential  $v_{\text{ext}}$  corresponding to the charge density  $\rho(\vec{r})$ . The concept of  $\Psi$  discussed here with respect to  $\rho(\vec{r})$  is still in

principle and not yet determined. Therefore, according to the second Hohenberg-Kohn theorem we obtain eq. 3.22

$$E_v[\rho'(\vec{r})] = F[\rho'(\vec{r})] + \int \rho'(\vec{r})v_{\text{ext}}(\vec{r})d\vec{r} \geq E_0. \quad (3.22)$$

Till here, this is still a conceptual approach, although a powerful one, which is not yet practically implementable due to the unknown universal functional  $F[\rho(\vec{r})]$ . After an year of the Hohenberg Kohn theorems, Kohn and Sham [125] devised a way similar to Hartree-Fock methods in structure, to implement this methodology. In this formulation, linear combination of basis functions is used to express electron density, very similar in form to HF orbitals [126]. A determinant is then formed from these functions known as Kohn-Sham orbitals.

Kohn and Sham introduced a reference system consisting of pseudo-electrons known as the Kohn-Sham electrons. These electrons do not interact with each other and live in an external potential, known as the Kohn-Sham potential  $v_{KS}[\rho(\vec{r})]$ , such that their ground-state charge density  $\rho(\vec{r})$  is identical to the charge density of the interacting system [127]. The Kohn-Sham (Schrödinger-like) equations are then written as eq. 3.23.

$$\left[ -\frac{1}{2}\nabla^2 + v_{KS}[\rho(\vec{r})] \right] \phi_i(\vec{r}) = \epsilon_i \phi_i(\vec{r}) \quad (3.23)$$

Here  $\phi_i(\vec{r})$  are the wave functions of Kohn-Sham electrons. The electron density in terms of these wave functions is defined by eq. 3.24

$$\rho(\vec{r}) = \sum_i^{\text{occ}} |\phi_i(\vec{r})|^2. \quad (3.24)$$

The Kohn-Sham potential  $v_{KS}[\rho(\vec{r})]$  is further defined as the sum of the external potential which is generated by the nuclei, the Hartree term and an unknown functional called the exchange-correlation potential. This sum is shown in eq. 3.25

$$v_{KS}[\rho(\vec{r})] = v_{\text{ext}}(\vec{r}) + v_{\text{Hartree}}[\rho(\vec{r})] + v_{\text{XC}}[\rho(\vec{r})]. \quad (3.25)$$

Each of the components of  $v_{KS}$  is evaluated separately. The external potential  $v_{\text{ext}}$  is typically a sum of nuclear potentials. The next term in the sum of eq. 3.25 is the Hartree potential, which is defined as

$$v_{\text{Hartree}}[\rho] = \int d^3\vec{r}_1 \frac{\rho(\vec{r}_1)}{|\vec{r} - \vec{r}_1|}.$$

Finally the unknown exchange-correlation functional has been defined in perhaps, more than a hundred ways over the past 30 years. A note with considerable detail about these is made in Section 3.1.4.1 on exchange and correlation functionals. The first and the simplest definition was called the Local Density Approximation (LDA), similar to the one put forth in the section on

Thomas-Fermi approach of 1920s. It can be written as shown in eq. 3.26

$$E_{xc}^{LDA} = \int d^3\vec{r} \epsilon^{HEG}(\rho)|_{\rho=\rho(r)}; v_{xc}^{LDA}(r) = \frac{d}{dn} \epsilon^{HEG}(\rho)|_{\rho=\rho(r)}, \quad (3.26)$$

where  $\epsilon^{HEG}(\rho)$  stands for the xc energy per unit volume of the homogeneous electron gas (HEG) of constant density  $\rho$ . In 1980, Ceperley and Alder [128] used Monte Carlo methods and tabulated the energies of the HEG at several densities.

Now that all the terms to define the Kohn-Sham potential are available, the Kohn-Sham equations in eq. 3.23 can be solved. Due to the functional dependence on the density, these equations form a set of nonlinear coupled equations. These are solved using the iterative procedure until self-consistency is achieved. The schematic in Figure 3.1-1, inspired by the chapter by Nogueira et al. [129] in the book on DFT [130], shows this iterative procedure.

This self-consistency cycle is continued until some convergence criterion is reached. The most common convergence criterions are based on the difference of total energies or densities from the iteration step  $i$  and  $i-1$ . Energy is calculated using the formula in eq. 3.27

$$E = \sum_i^{occ} \epsilon_i - \int d^3r \left[ \frac{1}{2} v_{Hartree}(\vec{r}) + v_{xc}(\vec{r}) \right] \rho(\vec{r}) + E_{xc}. \quad (3.27)$$



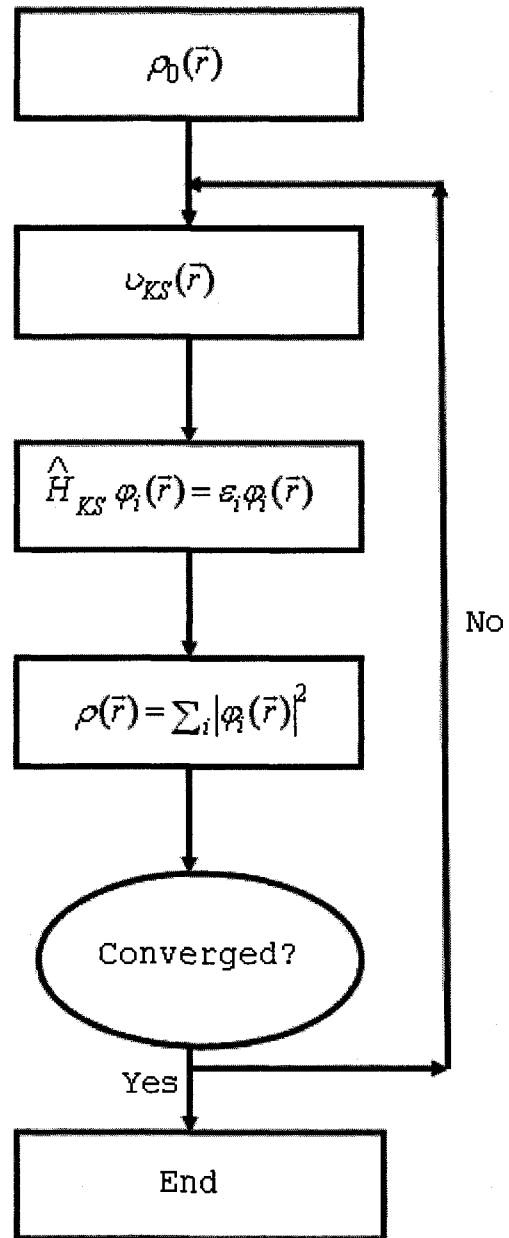


Figure 3.1-1 Schematic showing the self-consistent iterative procedure of a Kohn-Sham calculation.

### 3.1.4.1 Exchange and correlation functionals

The Kohn-Sham potential  $v_{KS}$  discussed in Section 3.1.4 has in it a term called the exchange-correlation potential  $v_{xc}$ . The formal definition of this is that it is the functional derivative of the exchange-correlation (XC) energy,  $E_{xc}$ . A lot of research has been focused over the last few decades to form different parameterizations for this function. The LDA functional defined in the Section 3.1.4 is the most simple of all of them. The XC energy  $E_{xc}$  can be separated into two parts, a pure exchange  $E_x$ , and a correlation part  $E_c$  as shown in eq. 3.28

$$E_{xc}[\rho] = E_x[\rho] + E_c[\rho]. \quad (3.28)$$

Early works in formulating a functional for  $E_{xc}$  focused only on one of these components at a time and then subsequently combined them, while the current trend is to construct both the parts in a combined fashion. In 1980, Vosko, Wilk and Nusair [131] used the Monte-Carlo results to form their correlation functional  $E_c^{VWN}$ . In 1981, Perdew and Zunger proposed their functional PZ81 [132]. After the concept of LDA, Generalized Gradient Approximation (GGA) functionals were introduced, where the functional has a very similar form, but now the energy  $\epsilon$  does not depend solely on the density  $\rho$ , but also on its gradient  $\nabla\rho$ . The

density gradient was introduced so as to preserve the analytic, symmetry and scaling features of the unknown XC functional. The most successful attempt to formulating the gradient corrected exchange functional is due to Becke who proposed his functional B88 in 1988 [133]. The development of correlation functionals proceeded much more slowly than that of the exchange functionals. In the same year, Lee, Yang, and Parr proposed their very famous LYP correlation functional [134]. Although B88 and LYP perform very well, they fail to show some scaling and limiting features that the unknown exact exchange-correlation functional should possess [135]. Keeping these in mind, Perdew et al. [136] proposed their PW91 correlation functional, with some correction in the theoretical weaknesses of B88. PBE (Perdew-Burke-Ernzerhof) [137] is yet another form of gradient corrected functionals proposed later.

A new generation of density functionals known as the 'hybrid' or 'adiabatic connection' methods is introduced and used lately. The idea behind this class of functionals is to weigh in a certain amount of non-local Hartree-Fock exchange. Becke's three parameter functional (B3) [138] is an example of such hybrid models. This in combination with PW91 and LYP correlation functionals form the popular

B3PW91 and B3LYP [139] methods respectively. These are defined as shown in eq. 3.29

$$E_{XC}^{B3-PW91/LYP} = (1 - a)E_X^{LSDA} + aE_X^{exact} + b\Delta E_X^{B88} + (1 - c)E_C^{LSDA} + cE_C^{PW91/LYP}, \quad (3.29)$$

where,  $a$ ,  $b$  and  $c$  are the three parameters that depend on the chosen forms for  $E_X^{GGA}$  and  $E_C^{GGA}$ . B3PW91 functional is extensively used in this dissertation work related to clusters' work.

### 3.1.5 Plane-Wave Pseudopotential Implementation of DFT

This section describes the plane wave implementation of the Kohn-Sham DFT used in this work to perform calculations on the solid state systems and crystal lattices. This '*Total-Energy Pseudopotential Approach*' has been developed to study solid systems consisting of extended matter, rather than atoms and molecules. In infinite periodic systems, such as crystals, there are an infinite number of interacting electrons, each of whose wave functions needs to be determined, and also the basis sets required to expand these wave functions need to be infinite. These two difficulties are overcome by (i) by using Bloch's Theorem [140] and (ii) by expanding the wave functions in plane wave basis sets. According to Bloch's Theorem, the one-particle effective Hamiltonian  $\hat{H}$  within a

periodic lattice commutes with the lattice-translation operator  $\hat{T}_R$ . Thus the Hamiltonian  $\hat{H}$  of a solid is periodically invariant. This leads to the expression of the wave function as a product of two functions, a periodic part and other a plane wave type function. This is expressed mathematically in eq. 3.30

$$\left[ \hat{H}, \hat{T}_R \right] = 0 \Rightarrow \Psi_{nk} = u_{nk}(\vec{r}) e^{ik \cdot \vec{r}}, \quad (3.30)$$

where the subscripts  $n$  and  $k$  are the quantum numbers used to denote the band index and the crystal momentum (a continuous wave vector that is confined to the first Brillouin zone of the reciprocal lattice [140]), respectively. In eq. 3.30 for  $\Psi$  above, the function  $u_{nk}(\vec{r})$  is periodic and it has the same periodicity as the direct lattice. It is expanded in terms of discrete plane-wave basis set with wavevectors  $\vec{G}$  that are reciprocal lattice vectors. Mathematically, eq. 3.31 represents the definition of this function.

$$u_{n\vec{k}}(\vec{r}) = \sum_{\vec{G}} C_{n\vec{k}}^{\vec{G}} \exp(i\vec{G} \cdot \vec{r}), \quad (3.31)$$

where  $C_{n\vec{k}}^{\vec{G}}$  are the plane wave coefficients and  $\vec{G}_i \cdot \vec{a}_j = 2\pi\delta_{ij}$ , where  $\vec{a}_j$  are the crystal lattice vectors. Thus, substituting eq. 3.31 in eq. 3.30, we get the equations for the wave

functions as the linear combinations of the plane waves as shown in eq. 3.32

$$\Psi_{n\vec{k}} = \sum_{\vec{G}} C_{n\vec{k}}^{\vec{G}} \exp(i(\vec{G} + \vec{k}) \cdot \vec{r}). \quad (3.32)$$

Another approximation used in the solid state DFT calculations is the use of pseudopotentials [141-143]. The electrons in the solid are divided into two groups: valence and core electrons. The electrons in the inner shells of an atom are very strongly bound to the nucleus and do not play any substantial role in their chemical bonding. Thus they form an almost inert core. A plane wave basis set is not suited to describe all the electrons because an all-electron plane wave calculation would require an impossibly large number (proportionally increasing the computational burden) of them to describe accurately the oscillations in the core regions which maintain orthogonality between valence and core electrons. This difficulty is overcome by introducing the concept of pseudopotentials [141-143].

The strong ionic potential in the core region is replaced by the weaker pseudopotential by this approximation. The wave functions corresponding to this pseudopotential are identical to the all-electron wave functions outside a chosen cutoff radius and therefore exhibit the same scattering properties.

The main requirement of a pseudo potential approach is that it reproduces the valence charge density associated with the chemical bonds. For pseudo and all-electron wave functions to be identical beyond the core radius, it is necessary for the integrals of the square amplitudes of the two functions to be the same [144]. This is tantamount to requiring 'norm-conservation' from pseudo wave functions. That is each of them should carry exactly one electron. This condition ensures that the scattering properties of the pseudopotential are reproduced correctly. These types of pseudopotentials are known as 'norm-conserving pseudopotentials'. An important factor in the pseudopotential applications is the degree of the 'hardness' of the pseudopotential. This depends on the number of Fourier components that pseudopotentials require for its accurate representation. Pseudopotential is considered 'soft' when it requires lesser number of Fourier components and is considered 'hard' if it requires more of them. Norm-conserving pseudopotentials for first row elements and transition metals turn out to be extremely hard [145,146]. More recently Vanderbilt [147] suggested a radical approach to improve the norm-conserving pseudopotentials where the pseudo wave functions in the core region are allowed to be as soft as possible. These

new class of pseudopotentials are known as 'ultra-soft pseudopotentials'. These tend to be much less expensive because the ultra-soft pseudo wave functions are smoother and so they can be described by smaller basis set. A major portion of calculations on the extended systems in this dissertation are performed using the ultra-soft pseudopotentials.

### **3.2 Classical Molecular Dynamics**

Unlike the techniques that have been discussed so far, Molecular Dynamics (MD) follow the principles of classical mechanics [121] rather than quantum mechanics. The technique of MD simulations forms a major part of the total suite of computational chemistry tools. Statistical mechanics [148] provides a means for determining physical properties of macroscopic sample of bulk liquid and solid, rather than just a single molecule at a single geometry. These results are obtained as the net result of the properties of many molecules in many conformations and many energy states. Practically, this difficult task of obtaining information of possible energy states and structural conformations is obtained using Molecular Dynamics [126]. Alder and Wainwright carried out the first Molecular Dynamics simulation in 1957 on a hard-sphere



fluid [149]. The first fluid with soft interactions was simulated by Rahman in 1964 [150] and the first complex fluid (water) was simulated by Rahman and Stillinger in 1971 [151]. Anees Rahman is famously known as the 'father' of MD [152].

Either Newtonian deterministic dynamics or a Langevin-type stochastic dynamics is used as a foundation to emulate the motion of the individual atoms within an assembly of  $N$  atoms. In a MD simulation, these  $N$  atoms are confined in a simulation cell of volume  $V$ . This cell is replicated in all spatial dimensions generating its own periodic images as those of the original  $N$  atoms. These periodic boundary conditions (PBC) are necessary in order to recompense the unwanted effects of the artificial surfaces associated with the finite size of the simulated system. The energetics and dynamics of the atoms in a MD simulation are obtained from a two-body or a *many-body inter-atomic potential*,  $H_I(r_{ij})$ , and the simulation involves the computation of forces experienced by each atom at each simulation time step from these according to eq. 3.33

$$F_i = -\sum_{j>i} \nabla_{r_i} H_I(r_{ij}), \quad (3.33)$$

where  $r_{ij}$  is the separation distance between two atoms  $i$  and  $j$ . During a MD simulation, initial positions of the atoms

are chosen with a set of initial velocities. These velocities are usually chosen to obey Maxwell-Boltzmann or Gaussian distribution at a given temperature, which gives the probability that an atom  $i$  has a velocity  $v_x$  in the  $x$ -direction at a temperature  $T$  [153] This is expressed in eq. 3.34

$$p(v_{ix}) = \left( \frac{m_i}{2\pi k_B T} \right)^{\frac{1}{2}} \exp \left[ - \frac{m_i v_{ix}^2}{2k_B T} \right]. \quad (3.34)$$

These velocities are then normalized such that the net momentum for the entire system is zero (that is, the system is not flowing). The forces on each atom are then computed using the energy/force expression (eq. 3.33) which depends on the *many-body inter-atomic potential*,  $H_I(r_{ij})$ . The atomic positions after a short time step  $dt$  are calculated using a scheme for the numerical integration of the Newton's equations of motions. One very famous integration scheme is the velocity verlet algorithm [153]. According to this, the positions,  $r_i$ , and velocities,  $v_i$ , of the atoms of mass  $m_i$  are updated at each simulation time step,  $dt$ , according to the rules set in eq. 3.35.

$$\begin{aligned}
 r_i(t + dt) &= r_i(t) + v_i(t)dt + \frac{1}{2} dt^2 \frac{F_i(t)}{m_i}, \\
 v_i\left(t + \frac{1}{2} dt\right) &= v_i(t)dt + \frac{1}{2} dt \frac{F_i(t)}{m_i}, \\
 v_i(t + dt) &= v_i\left(t + \frac{1}{2} dt\right) + \frac{1}{2} dt \frac{F_i(t + dt)}{m_i}.
 \end{aligned}
 \tag{3.35}$$

This iteration of obtaining the new velocities and accelerations of the atoms is repeated until the equilibrium is obtained. In this case of a MD simulation, equilibrium is not the lowest energy conformation, but it is a configuration that is reasonable for the system with the given amount of energy [126]. Once the system equilibrium is reached, the atomic coordinates at an interval of every few iterations are saved and this list of coordinates over time is known as the trajectory. The trajectory of the system is then analyzed to obtain information about the system. This is determined by computing the radial distribution functions, diffusion coefficients, vibrational motions or any other property computable by this information.

### 3.3 Ab Initio Molecular Dynamics

The main premise for the classical MD simulation to result in reliable answers, as has been discussed in the Section 3.2, is the ability of the many-body inter-atomic potential or the 'force-field' that is used to describe the

interactions of the involved atoms. Although the field of classical MD simulations has had an overwhelming success in the fields of condensed matter physics and materials modeling, this methodology has got some inherent limitations in it. They are (i) systems that consist of several different types of atoms in it require a large set of inter-atomic potential energy parameters to be parameterized, (ii) systems involving chemical events like the bond breaking and bond forming cannot be fully described by this 'force-field' technology, (iii) most force-fields do not include electronic polarization effects.

The technique known as *Ab Initio* Molecular Dynamics (AIMD) [154] overcomes these limitations [155,156]. AIMD is a rapidly growing technique, in which finite-temperature dynamical trajectories are generated by using forces obtained directly from electronic structure calculations performed 'on the fly'. A very common electronic structure method most commonly in the modern AIMD calculation is the Kohn-Sham formulation of density functional theory.

As discussed in Section 3.1.4, in the Kohn-Sham DFT the energy functional is expressed in terms of a set of  $n$  occupied single-particle orbitals  $\psi_1(r), \psi_2(r), \dots, \psi_n(r)$  and

the  $N$  nuclear positions  $R_1, \dots, R_N$ . It takes the form of eq. 3.36

$$\begin{aligned}
 E[\{\psi\}, \{R\}] = & -\frac{1}{2} \sum_{i=1}^n \int dr \psi_i^*(r) \nabla^2 \psi_i(r) + \\
 & \frac{1}{2} \int dr dr' \frac{\rho(r)\rho(r')}{|r-r'|} + E_{xc}(\rho) \\
 & + \int dr \rho(r) V_{\text{ext}}(r, R),
 \end{aligned} \tag{3.36}$$

where  $V_{\text{ext}}(r, R)$  is the total external coulombic attraction between one electron and the nuclei and the density  $\rho(r)$  related to the orbitals by  $\rho(r) = \sum_{i=1}^n |\psi_i(r)|^2$ .

A possible strategy of accommodating the electronic structure calculations in the MD scheme of things is: (i) to minimize the energy functional in the eq. 3.36 for a given set of initial nuclear positions  $R_1, \dots, R_N$  to obtain the ground state density  $\rho_0(r)$  and the corresponding orbitals  $\psi_1^0(r), \psi_2^0(r), \dots, \psi_n^0(r)$ . (ii) Once these quantities are obtained, the forces between the nuclei are obtained by the Hellman-Feynman theorem defined in eq. 3.37

$$F_I = -\frac{\partial}{\partial R_I} E[\{\psi^0\}, \{R\}]. \tag{3.37}$$

These forces are then fed into a numerical integration scheme together with a set of initial velocities for the nuclei, and a step of molecular dynamics is carried out which results in a new set of velocities and nuclear

positions. For these new positions and the velocities, the ground state density and therefore the orbitals are obtained minimizing the energy functional given by eq. 3.36, the forces are obtained using eq. 3.37 and are again given to a integration scheme like velocity verlet algorithm. This process is continued until a total trajectory is obtained. This scheme of implementation is known as Born-Oppenhiemer Molecular Dynamics (BOMD). As can be seen, this is a rather computationally intensive technique since it involves the solving of Kohn-Sham orbitals at each and every step of MD.

An alternative approach to this is suggested by Car-Parrinello [157], where rather than minimizing the energy functional in eq. 3.36 at each and every step of MD and obtaining the corresponding orbitals, a fictitious time dependence is introduced into the Kohn-Sham orbitals, i.e.,  $\psi_i(r) \rightarrow \psi_i(r, t)$ , and a dynamics is introduced that propagates an initially fully minimized set of orbitals to subsequent minima corresponding to each new nuclear configuration [155]. The complete motion of the system including both the fictitious orbital dynamics and real nuclear dynamics is given by the Car-Parrinello (CP) Lagrangian and this Lagrangian yields the CP equations of motion which are shown in eq. 3.38.

$$\begin{aligned}
 M_I \ddot{R}_I(t) &= - \frac{\partial}{\partial R_I(t)} E[\{\psi(t)\}, \{R(t)\}] \\
 \mu \ddot{\psi}_i(r, t) &= - \frac{\delta}{\delta \psi_i^*(r, t)} E[\{\psi(t)\}, \{R(t)\}] + \sum_j \Lambda_{ij} \psi_d(r, t),
 \end{aligned}
 \tag{3.38}$$

where  $\Lambda_{ij}$  are a set of Lagrange multipliers  $\mu$  is a fictitious kinetic energy parameter.

Calculations reported in the Section 7.3.4 of Chapter 7 and Section 8.3.2 of Chapter 8 are performed using the *Ab Initio* Molecular Dynamics method.

### 3.4 Monte Carlo Techniques

Monte Carlo (MC) techniques, introduced by Metropolis et al. in 1953 [158], are based on the use of probabilistic concepts. These methods have applications in diverse fields of computational sciences such as catalysis, polymer science, nuclear physics etc. The name "Monte Carlo" was coined by Metropolis, because of the similarity of statistical simulation to games of chance, and because the capital of Monaco was a center for gambling [159,160].

In this method, a system composed of  $N$  interacting atoms is given a set of initial coordinates. The emergence of this initial configuration is then generated by successive random displacements of the atoms. However, not all configurations generated by these displacements are accepted, and there is certain criterion for the acceptance

of the move. In a typical Metropolis algorithm [158], the following steps are followed.

- A unique random value is generated for each of  $3N$  coordinates ( $r_N$ ).
- The energy of the new configuration is calculated and compared to the value of the old one.
  - If the energy is lower, the new configuration is accepted.
  - If the energy is larger, Boltzmann factor of the new configuration  $\exp(-V(r_N)/k_B T)$  is compared to the random number between 0 and 1
    - If the random number is lower than the Boltzmann factor, the new configuration is accepted
    - In other case, configuration is rejected.

The result reported in the Section 6.3.2 of Chapter 6 on novel Li-C-Be materials for hydrogen storage is obtained using the Monte Carlo techniques.



## CHAPTER 4

### STRUCTURE AND ENERGETICS OF NEUTRAL $BE_N$ (N=1-17) CLUSTERS: A DENSITY FUNCTIONAL THEORY STUDY

One of the roles that is expected of theory and computation to play in the development of hydrogen storage materials is to help clearly understand the physics and chemistry of the fundamental interactions of hydrogen with them at various size scales [14]. Atomic clusters fall under an interesting class of size because they form the intermediate phase of matter between a single atom and the bulk material. The properties of such clusters are of great importance because they are size and composition specific and here every atom and electron counts [42]. The emergence of new research areas like nanoscience and nanotechnology and their promise of different possible technological applications have further fueled the interest in cluster systems. The so-called 'magic clusters' are of considerable importance.

#### 4.1 Introduction

The interest in the physics and chemistry of atomic clusters is ever growing among the scientific community [161,162]. Since an atomic cluster represents an intermediate phase of matter between a single atom and the bulk material, the convergence of the clusters properties towards the corresponding macroscopic characteristics of the material has been a matter of great interest. Divalent-metal clusters (e.g.,  $\text{Be}_n$ ,  $\text{Mg}_n$ ,  $\text{Hg}_n$ ) are particularly interesting in this respect, due to their  $s^2$  closed shell atomic configuration and considerably large  $sp$  excitation energy [163]. Due to weak Van der Waals forces in small divalent metal clusters, such clusters are expected to behave like insulators. As the divalent cluster size increases towards the bulk, the  $s$  and  $p$  bands overlap giving the material strongly metallic characteristics [164]. This implies that there is a transition affecting the nature of the chemical bond from weak Van der Waals to strong metallic bonds somewhere as a function of increased cluster size.

Of all the divalent metals, beryllium has attracted a lot of attention lately due to its relevance in astrophysics [165,166] and importance as a component in hydrogen storage materials such as  $\text{Li}_2\text{BeH}_4$  [167]. Moreover,

the value of studying beryllium clusters theoretically increases due to the scarcity of experimental studies [168,169] on these clusters due to their toxic nature [170]. Beryllium does not form a diatomic molecule because such a molecule would have two electrons in the  $\sigma_s$  bonding orbital and two electrons in the  $\sigma^*$  antibonding orbital, and therefore the total number of bonding electrons would then be zero. The  $\text{Be}_2$  dimer is therefore considered to be one of the most demanding computational chemistry problems which require careful selection of electronic structure methods [171-174]. A brief review of the current state of knowledge on  $\text{Be}_2$  is presented here.

$\text{Be}_2$  was experimentally generated by Bondybey [168,169] in supercooled vapor produced by laser vaporization of the metal. The experimental Be-Be bond length reported by these authors is  $4.72a_0$  or  $2.497 \text{ \AA}$  ( $a_0=0.529 \text{ \AA}$ ) with a corresponding binding energy of  $(790\pm 30) \text{ cm}^{-1}$  or  $(0.098\pm 0.004) \text{ eV}$  [168]. There has been considerable theoretical work [164,170,171,173,175-185] on  $\text{Be}_2$  previously which spans across a wide range of different methods including both *ab initio* and DFT methods. Harrison et al. [173] performed CI calculations and reported the binding energies of a Be dimer as  $1.86 \text{ kcal/mol}$  ( $0.0806 \text{ eV}$ ). MP4(SDTQ) study of  $\text{Be}_2$  by Kaplan et al. [181] resulted in a

Be-Be bond length of 2.56 Å and a binding energy of 1.83 kcal/mol (0.08 eV). A complete active space/configuration interaction (CASSCF/CI) study by Morrison and Handy [175] predicted a bond length of 2.50 Å and a binding energy of 1.86 Kcal/mol (0.08 eV). Klopper et al. [180] employ a MP2-R12 method to study the one-particle basis set limit of second-order correlation energies on small Be<sub>n</sub> clusters and report a bond length of 2.65 Å and a binding energy of 0.06 eV. Basis sets of different complexities in conjunction with different density functionals are used to address this interesting problem of Be<sub>2</sub> dimer. Sudha et al. [177] employed BPW91, BP86 with 63111/3111(3df) basis set and reported the values of 2.44 Å and 0.36 eV each for bond length and binding energies respectively. The same authors also used the basis set 631/31 with BPW91, BP86, B3LYP methods and reported the values set of (2.47 Å, 0.36 eV), (2.48 Å, 0.36 eV) and (2.54 Å, 0.18 eV) respectively for the (bond length, binding energy) pair. Beyer et al. [177] use 63111/3111(3df) basis set with B3LYP functional and find that Be-Be equilibrium bond length is 2.48 Å and the binding energy is 0.20 eV. Murray et al. [182] used *8s5p2d1f* basis set with the functionals BLYP, BP86, SVWN and report the values of (2.43 Å, 0.26 eV), (2.45 Å, 0.35

eV), (2.40 Å, 0.56 eV) respectively for (bond length, binding energy) pair.

Early work conducted on other Be clusters focused on the calculation of equilibrium geometries and binding energies, using *ab initio* techniques such as the wavefunction based methods like Configuration Interaction (CI) [186] and QCISD; which account for the single and double excited states in the QuadraticCI [187]. MultiReferenced Configuration Interactions (MRCI) in conjunction with extended basis sets was employed by Lee et al. [171] to study Be<sub>3-5</sub> cluster binding energies and reported 24 (Be<sub>3</sub>), 83 (Be<sub>4</sub>) and 110 (Be<sub>5</sub>) Kcal/mol respectively. The second, third and fourth orders of the Moller Plesset Perturbation Theory [188] were also used by several authors to study Be clusters [180,181,189]. Pamidighantam et al. [189] studied the bonding properties of Be<sub>3-7</sub> clusters using the more *ab initio* methods like the coupled cluster [190] and perturbation theories [188] at different orders until MP4 and reported the binding energy per atom for Be<sub>3</sub>, Be<sub>4</sub>, Be<sub>5</sub>, Be<sub>6</sub> and Be<sub>7</sub> clusters to be 7.2, 20.9, 24.4, 22.8 and 26.3 Kcal/mol respectively. Klopper et al. [180] combined CCSD(T) and MRCI calculations on Be<sub>3</sub> and Be<sub>4</sub> and reported their binding energies as 27 and 88 kcal/mol respectively.

Most of the early DFT work [170,185] on Be clusters were performed on the platform of the local spin density approximation (LSDA) [124,125]. Estela et al. [185] developed a many body potential for beryllium by performing LSDA calculations on the  $Be_n$  clusters from  $n=3-5$  and they exercised these parameters for the bulk structure properties of beryllium. A comparative study was performed by Oritz et al. [191] using various density functional approximations and they concluded that the gradient corrections were noteworthy in ascertaining the ground state properties of such divalent metal dimers [164], There were also gradient corrected calculations reported on the  $Be_n$  clusters [164,176-178,191], but there were more variations rather than the similarities in the results. Cerowski et al. [178] more recently used this many body potential and symbiotic Genetic Algorithm (SGA) methods of Molecular Dynamics to find the local minima of the  $Be_n$  clusters until  $n=41$ . They then used these initial geometries and calculated the energies of these structures at an *ab initio* method, self-consistent-field (SCF) Linear Combination of Atomic Orbital (LCAO) - Molecular-Orbital (MO) method.

Many *ab initio* and DFT (both LDA and GGA) results were published [170,171,176,179-181,183-185,189,192]; however

(i) the geometry was calculated at a level of theory lower than the energy calculations resulting in errors (ii) the higher level calculations were performed only for smaller beryllium clusters. The aim of this work is to carry out the higher level DFT calculations on a more extended set of  $\text{Be}_n$  clusters until  $n=17$ , obtain their equilibrium geometries, bond lengths, energies. The stability of these clusters is discussed in terms of the Binding energies per atom and the second difference of energies [43,193,194]. Electronic structure properties like the energy gap between the highest occupied molecular orbital (HOMO) and the lowest unoccupied molecular orbital (LUMO), the ionization potentials and the electron affinities have been used to obtain further insights into the stability of these clusters. The variation of these electronic properties as a function of the number of atoms in these clusters is discussed.

Remaining of the chapter is arranged in the following hierarchy. Section 4.2 discusses the computational methods we have used in this work. Section 4.3 presents the results and the discussion. In results, Section 4.3.1 is dedicated to the structure of the different clusters. Section 4.3.2 discusses the stability of these clusters in the perspective of different electronic structure properties

like Binding energies, Second difference of energies  $\Delta_2E$ , HOMO-LUMO Gaps (HLG), and vertical Ionization Potentials. Section 4.4 addresses the conclusions based on the results in this work.

## 4.2 Methods

Density Functional Theory (DFT) calculations of  $Be_n$ ,  $n=1-17$ , neutral (zero total charge) clusters are performed using the Gaussian 03 program, Revision C.02 [195]. A large variety of possible geometrical arrangements of these clusters are investigated, including three-dimensional (3-D), cyclic, and linear configurations. The density functional employed in these calculations is the B3PW91, one of the most successful hybrid functionals [196], that includes an exchange description constituted by contributions of local, nonlocal (Becke 3-parameter) and Hartree-Fock exchange terms, and correlation given by the 1991 Perdew and Wang (PW91) nonlocal GGA functional [120]. This DFT method is used in combination with the 6-31+G\* basis set, which is a split-valence double-zeta that considers *d*-like polarization functions on heavy atoms and a set of diffuse *s*- and *p*-like functions on heavy atoms [120].



The B3PW91 method is known to perform very well on the structure and stability of pure Be [197,198] clusters. For instance, Zhao et al. [198] studied the structure and stability of  $\text{Be}_6$ ,  $\text{Be}_6^+$ , and  $\text{Be}_6^-$  clusters using B3PW91, B3LYP, MP2 levels in combination with the 6-311G\* and 6-311+G\* basis sets. They have also used CCSD(T)/6-311+G\* to check the reliability of the results when the calculations at the aforementioned levels contradicted each other. In particular, these authors correctly predicted using the B3PW91, MP2, and CCSD(T) methods that the ground state configuration of  $\text{Be}_6$  is a  $D_{2h}$  structure, also well predicted by Pacchioni and Koutecky' [199] using pseudopotential configuration interaction (CI). At the B3LYP level of theory, however, Zhao et al. found that the  $D_{2h}$  structure is a transitional state instead of a local minimum, and that the most stable configuration of  $\text{Be}_6$  is wrongly predicted to be a  $D_{3d}$  structure, which was also reported by Beyer et al.[176] at the B3LYP/6-311++G (3df) level as the most stable one for  $\text{Be}_6$ . Similar conclusions are drawn by the same authors for  $\text{Be}_5$  in terms of the comparable performance of the B3PW91, MP2, and CCSD (T) methods. Hence, B3PW91/6-31+G\* theory level is further used in this work for the prediction of accurate geometric and reliable energetics of  $\text{Be}_n$  clusters for which electron correlation effects are very

important. When this theory level is used, errors in calculated bond lengths (Å) and absolute energies (Ha) are expected to be in the third and fifth decimal respectively [122].

Geometry optimizations and harmonic vibrational frequency calculations for all the 17  $\text{Be}_n$ ,  $n=1-17$ , ground state clusters, different spin multiplicity ( $2S+1$ ) state clusters, and isomers are performed to ensure that stationary points on the Potential Energy Surface of the clusters are in fact local minima. These calculations were run for different spin multiplicity states of each cluster and the structure with a particular spin multiplicity state and the least energy is divulged as the most stable configuration and the other higher energy structures are considered as their higher-energy isomers. All the clusters reported here are neutral structures i.e., the total charge of the initial structures was taken as zero. Zero-point corrected absolute energies are used for further calculation of binding energies and second differences in energy. A particular structure with a particular spin multiplicity is reported as a ground state only after running several single point calculations of that geometric structure with different multiplicities.

### 4.3 Results

At the B3PW91/6-31+G\* DFT level, the calculated absolute electronic energy corresponding to the  $2S^2 \ ^1S$  (singlet) ground state and the lowest triplet state  $2P \ ^3P^0$  state of atomic beryllium are -14.65607 and -14.57203 Hartrees respectively. From this energetic information the calculated excitation energy of the triplet state of the beryllium atom is  $18445.5 \text{ cm}^{-1}$  (2.29 eV); which underestimates the experimental value of 2.73 eV [200] by 0.44 eV. Tozer et al. [201] used the time-dependant form of DFT, TDDFT which is better at calculating the excitation energies and predict a difference of 0.23 eV between their excitation energy value of 2.50 eV and the experimental value. They also observe that this difference of 0.23 eV is acceptable [201]. Table 4.3-A lists the energies (in Hartrees) and the spin multiplicity states of the observed ground states in our calculations. Ground state structures of  $\text{Be}_n$  neutral clusters are shown in Figures 4.3-1 ( $n=2-11$ ) and 2 ( $n=12-17$ ) along with selective bond lengths.

Table 4.3-A Total energies and their spin multiplicity states for  $\text{Be}_n$  clusters ( $n=1$  to 17).

Cluster, $\text{Be}_n$	Spin multiplicity $m$	Symmetry	GroundState Energy (Ha)
$n = 1$	1		-14.65607
2	1	$D_{\infty h}$	-29.32076
3	1	$C_s$	-44.02257
4	1	$C_1$	-58.78485
5	1	$C_1$	-73.49911
6	3	$C_1$	-88.20949
7	1	$C_1$	-102.94852
8	3	$C_1$	-117.70672
9	3	$C_1$	-132.47926
10	1	$C_1$	-147.24799
11	1	$C_1$	-161.99484
12	1	$C_1$	-176.72874
13	1	$C_1$	-191.48123
14	1	$C_1$	-206.23032
15	1	$C_1$	-220.97780
16	3	$C_1$	-235.73453
17	1	$C_1$	-250.52936

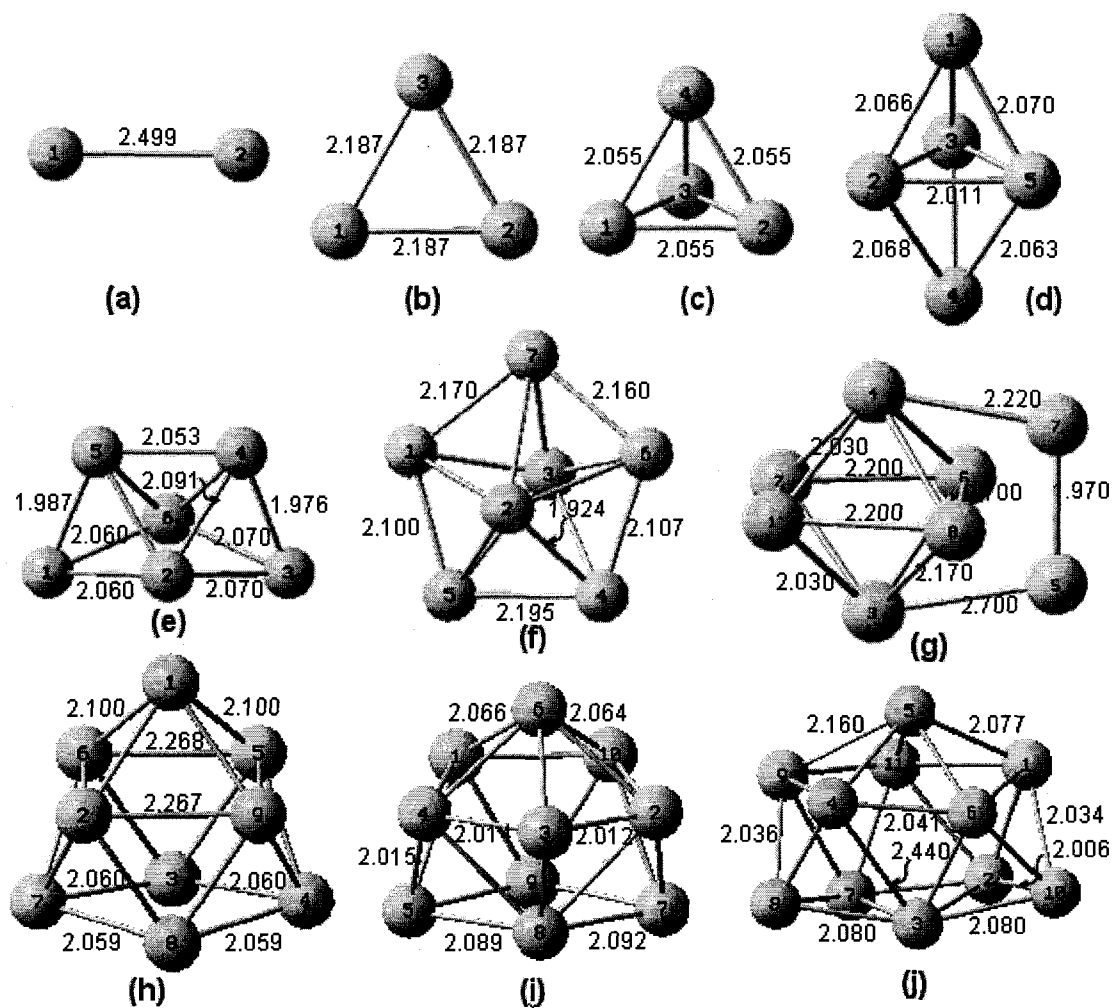


Figure 4.3-1 Ground state structures of  $\text{Be}_n$  ( $n=2-11$ ) clusters with important bond lengths in angstroms.

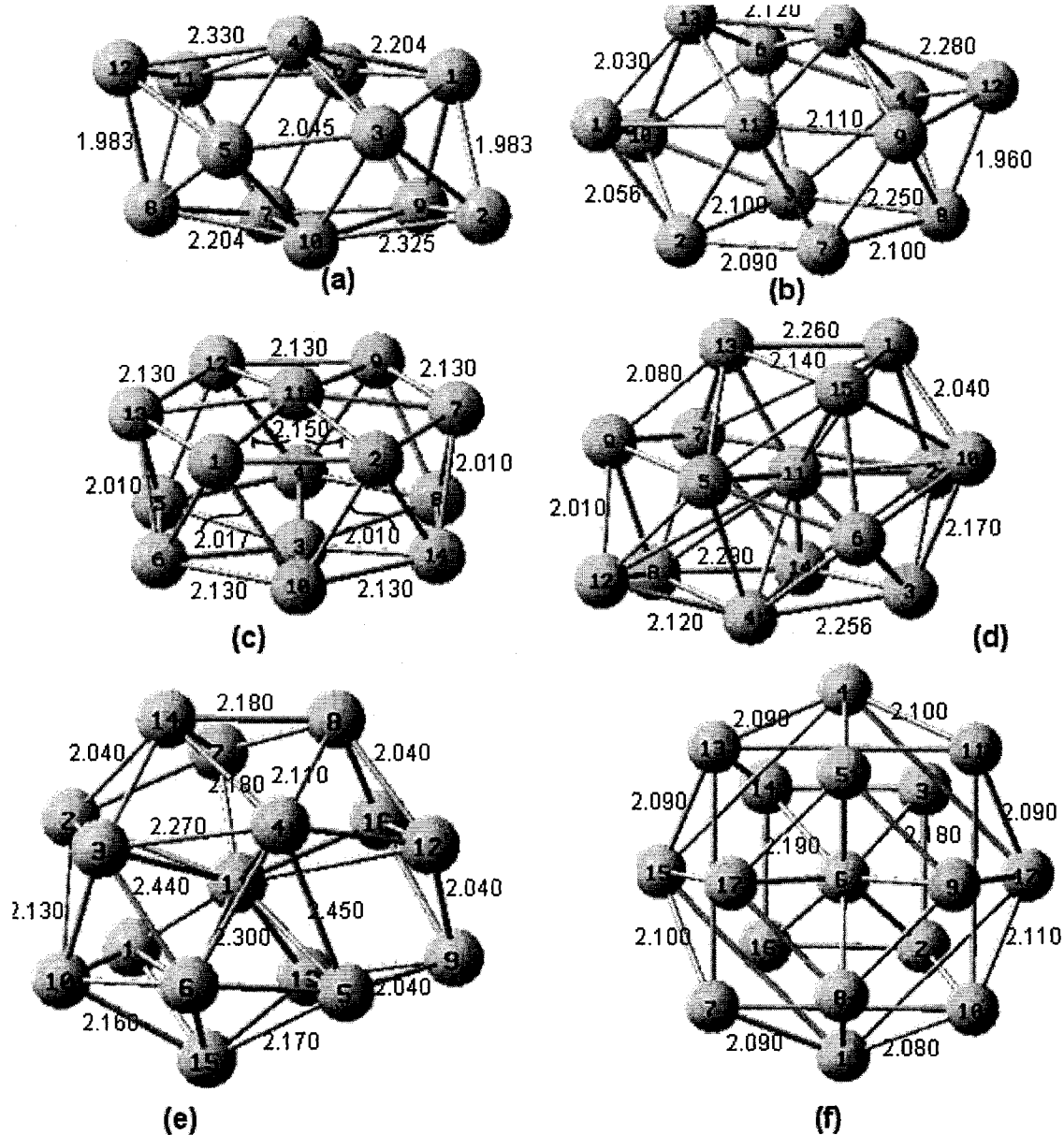


Figure 4.3-2 Ground state structures of Be<sub>n</sub> (n=12-17) clusters with important bond lengths in angstroms.

Section 4.3.1 and its subsections describe the geometries of the ground states of  $\text{Be}_n$  ( $n=1-17$ ) clusters.

#### 4.3.1 Structure of $\text{Be}_n$ ( $n=2-17$ ) Clusters

##### 4.3.1.1 $\text{Be}_n$ ( $n=2-4$ ) clusters

At the B3PW91/6-31+G\* theory level used in this work,  $\text{Be}_2$  (Figure 4.3-1a) is a spin singlet with a Be-Be bond length of 2.499 Å (only overestimated by 0.002 Å). The triplet multiplicity state of a Be dimer has a bond length of 2.02 Å. This structure is 0.58 eV higher in energy than the ground state.

The structure of  $\text{Be}_3$  ground state in our calculations is an equilateral triangle with bonds of 2.187 Å (Figure 4.3-2b). Comparisons with the previous published results [164,176,177,189] on  $\text{Be}_3$  show that DFT is predicting a smaller bond length for these systems when compared with other *ab initio* methods. The  $\text{Be}_3$  system has an isomer 0.34 eV higher than the ground state, which is a spin triplet isosceles triangle of bond lengths 2x2.13 Å and 1.94 Å. We also studied the singlet and the triplet states of  $\text{Be}_3$  linear system, which have not been examined in previous studies. These linear chains of beryllium atoms are considerably higher in energy (1.36 eV, triplet and 1.64 eV, singlet) than the equilateral triangle ground state.

The ground state structure of  $\text{Be}_4$  (Figure 4.3-1c) observed in the B3PW91 results of our calculation is of the shape of a regular tetrahedron with all the sides having a length of 2.055 Å. This system, like the previous ground states, also has a spin singlet multiplicity. Among the many other  $\text{Be}_4$  structures studied in this work, a stable isomer for  $\text{Be}_4$ , which has a spin multiplicity 3 is 0.99 eV higher in energy than the ground state. It has a distorted tetrahedral shape with bond lengths  $\text{Be}_2\text{-Be}_3 = 2.189$  Å and  $\text{Be}_2\text{-Be}_4 = 2.192$  Å while all the other bond lengths are equal to 2.012 Å. One other isomer of  $\text{Be}_4$  is observed in our study. We observe that this Y-shaped isomer is a singlet state and is 2.41 eV higher in energy than  $\text{Be}_4$  singlet ground state. The bond lengths of the two top branches of this Y structure are each 2.17 Å and the bottom branch is 2.21 Å. We observe that quintet state of this structure is not a stable one with two imaginary frequencies. The four Be atoms linear chain (both singlet and triplets) are considerably higher in energy than the ground state. One other isomer is a square of side 2.037 Å with a Be atom at its each vertex. This is a triplet in its multiplicity.

#### **4.3.1.2 $\text{Be}_n$ (n=5-10) clusters**

$\text{Be}_5$  ground state according to our calculations is a spin singlet tilted trigonal bipyramid (Figure 4.3-1d) with



the length of the equilateral triangular base (Be2-Be3-Be5) as 2.011 Å. Two other beryllium atoms (Be1 and Be4), one above this triangular plane and one below this triangular plane form two tilted tetrahedrons with the triangular base. The upper tetrahedron has the bond lengths of Be1-Be5 = 2.070 Å, Be1-Be2 = 2.066 Å and Be1-Be3 as 2.064 Å. The lower tetrahedron has the bond lengths of Be4-Be5 = Be4-Be3 = 2.063 Å and Be4-Be2 = 2.068 Å.

The ground state of the Be<sub>6</sub> cluster obtained in our calculations, with the corresponding bond lengths is shown in Figure 4.3-1e. The shape of this structure can be seen as a bicapped tetrahedron. This ground state has a spin multiplicity of m=3. The bond lengths of the base of this tetrahedron are Be1-Be2 = Be1-Be6 = 2.06 Å and Be2-Be3 = Be3-Be6 = 2.07 Å. Two sides of this bicapped tetrahedron in Figure 4.3-1e have the bond lengths of Be1-Be5 = 1.987 Å and Be3-Be4 = 1.976 Å. The bond lengths of the four diagonals of this system are Be2-Be5 = 2.075 Å, Be2-Be4 = 2.091 Å, Be6-Be5 = 2.082 Å and Be6-Be4 = 2.098 Å. This Be<sub>6</sub> cluster has five stable isomers. Another octahedron shaped structure with multiplicity 3 is observed to be 0.18 eV higher in energy than the ground state. The other stable isomers for Be<sub>6</sub> observed in our calculation are with quintet spin multiplicity and 0.16 eV less stable than the ground

state, other with  $m=1$  and 0.63eV less stable, one with  $m=5$  and 1.20 eV less stable, one with  $m=3$  and 1.84 eV less stable, and one of  $m=1$  and 1.91 eV less stable than the ground state.

The ground state  $\text{Be}_7$  is observed as a tilted pentagonal bipyramid with spin multiplicity of 1. This is shown in Figure 4.3-1f. Four stable isomers are found. Another structure with a similar structural confirmation is observed 0.0002 eV higher in energy than the ground state ground state. The other isomers observed for  $\text{Be}_7$  are the regular hexagon shaped systems with six beryllium atoms at the six corners of a hexagon and a seventh atom at the center of the hexagon. The system with this shape and a multiplicity of  $m=3$  is 0.84 eV higher in energy than the ground state. Two similar structures with the multiplicities of 1 and 5 are 0.86 eV and 1.29 eV higher in energy than the ground state. Another structure of a shape of a planar heptagon is also observed in our calculations which is 2.65 eV higher in energy than the ground state.

The  $\text{Be}_8$  ground state observed in our calculations is a spin quintet (Figure 4.3-1g). The shape of this ground state can be seen as a distorted crown shape with a triangular base (formed by  $\text{Be}_1$ ,  $\text{Be}_2$ ,  $\text{Be}_7$ ) and a tetrahedron (formed by  $\text{Be}_8$ ,  $\text{Be}_3$ ,  $\text{Be}_5$ ,  $\text{Be}_6$  and  $\text{Be}_4$ ,  $\text{Be}_4$  being the apex

of the tetrahedron) on top of that. Our calculations also reveal 5 higher energy isomers for  $\text{Be}_8$ . One isomer is a spin triplet with 0.14 eV higher in energy than the ground state. The shape of this isomer is more like a distorted pentagonal bipyramid. Another isomer with a spin singlet is seen which is 0.75 eV less stable than the ground state. The shape of this isomer is a 3-dimensional structure with a base of pentagon and three other beryllium atoms in a plane above that plane of the base. Another structure with a confirmation very similar to this isomer but with a multiplicity of a quintet is also seen which is 0.86 eV less stable. A structure very similar in the shape to the ground state but having a septet spin multiplicity is observed as 0.99 eV less stable than the ground state.

The ground state of  $\text{Be}_9$  ground state has triplet multiplicity state. This structure is shown in the Figure 4.3-1h. The shape of this system has a four sided square base (formed by the atoms  $\text{Be}_3$ ,  $\text{Be}_4$ ,  $\text{Be}_8$  and  $\text{Be}_7$ ) with the bond length of 2.06 Å and a square pyramid on top of that (formed by the atoms,  $\text{Be}_1$ ,  $\text{Be}_2$ ,  $\text{Be}_5$ ,  $\text{Be}_6$ ,  $\text{Be}_9$ , the apex of this square pyramid being the atom  $\text{Be}_1$ ). Two higher energy isomers for this  $\text{Be}_9$  cluster are observed with shapes very similar to that of the ground state confirmation. One of them is a spin singlet which is higher in energy than the

ground state by an amount of 0.19 eV. The other one is a spin quintet and this is 1.33 eV less stable than the ground state.

#### 4.3.1.3 Be<sub>n</sub> (n=10-17) clusters

The ground state of Be<sub>10</sub> is shown in Figure 4.3-1i with the important bond lengths highlighted. It is a spin singlet. The icosahedral shape of the pure Be clusters observed previously continues even in this cluster. The rectangular base of this cluster (formed by the atoms, Be5, Be7, Be8 and Be9 as shown in Figure 4.3-1i) has the bond length of 2.09 Å approximately. At the height of approximately 2.01 Å above this rectangular base is a pentagonal prism formed by the atoms Be1, Be2, Be3, Be4, Be10 and Be5 (ref Figure 4.3-1i). The first four atoms in this list form the irregular pentagon with the bond lengths of approximately 2.01 Å. The Be6 atom (Figure 4.3-1i) is the apex of this prism which is at the height around 2.065 Å from the pentagonal prism base. We have searched for the higher energy isomers for this cluster by making the spin multiplicity of the structure as a variable. We observe that it has a spin triplet isomer which is 0.45 eV less stable than its singlet ground state. This isomer is the same as its ground state but has higher average bond length. For instance, the bond lengths of the rectangular

base of this isomer are 2.15 Å and 2.09 Å. The pentagonal base of the prism which also has a bond length of 2.04 Å in this structure is at the height of 2.04 Å above the rectangular base. The apex of this structure is at approximately 2.14 Å above the pentagonal base.

Figure 4.3-1j shows the ground state of  $\text{Be}_{11}$  which is also a spin singlet. Icosahedral shape is again obvious in this ground state also. The structure of this cluster is also very similar to the one observed for the  $\text{Be}_{10}$  cluster, but the extra atom goes to the base forming a pentagonal base rather than a rectangular one. Therefore this structure can be viewed as two layers of pentagonal bases one above another with an apex for the top pentagon forming a pentagonal prism at the top. The bond lengths of the bottom pentagon are nearer to the value of 2.08 Å. The top pentagonal layer is at a height of 2.035 Å above the bottom layer. The apex of this top prism is at a diagonal length of around 2.16 Å from its bottom. As with the other Be clusters, we have searched for the higher energy isomers of this cluster as well and we see that the spin triplet multiplicity of this structure is 0.7 eV higher in energy than the ground state. The base pentagonal average bond lengths of this isomer are 0.1 Å larger than the ground state. The height of the top irregular pentagon is 1.95 Å

above the bottom base in the higher energy triplet, which is around 0.8 Å shorter than the singlet ground state. The diagonal height of the apex of this cluster is 2.22 Å which is 0.06 Å higher than its corresponding bond length in the ground state.

The ground state of Be<sub>12</sub> cluster is shown Figure 4.3-2a. The multiplicity of this ground state is also 1. The average nearest neighbor bond length in this icosahedral structure is slightly larger than that in the Be<sub>11</sub> cluster. This shape can be viewed more as a hexagonal prism above a pentagonal base. The bond lengths of the base vary from 2.04 Å to 2.33 Å. The hexagonal base of the irregular hexagonal prism in this structure is 1.98 Å above the pentagonal base of the structure. The diagonal heights of the apex of this hexagonal prism (Figure 4.3-2a) are 2.33 Å (Be<sub>12</sub>-Be<sub>4</sub>) and 2.20 Å (Be<sub>1</sub>-Be<sub>4</sub>). The higher spin state (triplet) of this structure is 0.20 eV less stable than the ground state. The average nearest neighbor bond length of this isomer is also higher than its ground state.

The ground state structure of a Be<sub>13</sub> cluster is that of a tri-capped hexagonal prism over a rectangular base. It is a spin singlet in its multiplicity and is shown in Figure 4.3-2b. The figure also shows some of the bond lengths of this ground state. The nearest neighbor bond lengths of the

rectangular base (Figure 4.3-2b) formed by atoms Be2-Be3-Be8-Be7 are  $\text{Be2-Be3} = \text{Be7-Be8} = 2.1 \text{ \AA}$  and  $\text{Be3-Be8} = 2.25 \text{ \AA}$ ,  $\text{Be2-Be7} = 2.09 \text{ \AA}$ . The diagonal heights of the hexagonal prism above this plane are  $\text{Be8-Be12} = 1.96 \text{ \AA}$  and  $\text{Be2-Be1} = 2.06 \text{ \AA}$ . The three apexes in the tri-capped hexagonal prism are the atoms Be5, Be6 and Be13. The distance of these apexes above the hexagonal base (middle layer of the whole structure) are  $\text{Be1-Be13} = 2.03 \text{ \AA}$  and  $\text{Be12-Be5} = 2.28 \text{ \AA}$ . The distance between the top apex are of the order of  $\text{Be5-Be13} = 2.12 \text{ \AA}$ . The triplet state isomer of this structure is 0.30 eV less stable than the ground state. The trend of higher energy isomers having a larger average nearest distance neighbor is seen in this higher energy state also.

The ground state of  $\text{Be}_{14}$  is a spin singlet and is shown in Figure 4.3-2c. This ground state is a closed structure formed by the two hexagons with an atom each in the middle of those hexagons very slightly above or below their planes. The bond length of each side of this hexagon is  $2.13 \text{ \AA}$  and the diagonal distance between the two hexagonal planes are of the order of  $\text{Be6-Be13} = \text{Be2-Be10} = \text{Be7-Be14} = 2.01 \text{ \AA}$ . The distance between the atoms on the vertices of the hexagon (for both the hexagons) and the one in the center is in the range of  $2.14\text{-}2.15 \text{ \AA}$ . This ground state also has an isomer of multiplicity 3, which is 0.18 eV less

stable. The isomer has average bond length higher than the ground state.

The structure of the spin singlet  $\text{Be}_{15}$  ground state is shown in Figure 4.3-2d. It is a more closely packed icosahedral structure. Despite several attempts to study the triplet state of this system we observe that the higher state of this ground state is unstable.

The ground state of  $\text{Be}_{16}$  and  $\text{Be}_{17}$  clusters is shown in Figures 4.3-2e and 4.3-2f. The icosahedral growth of beryllium clusters is continued in these clusters as well. In our calculations we see that the ground state of  $\text{Be}_{16}$  is a spin triplet unlike the previous singlets. The singlet state and the quintet states of this structure are 0.11eV and 0.02 eV higher in energy than the ground state. Our calculations did not yield any higher energy isomers for  $\text{Be}_{17}$  cluster.

#### **4.3.2 Stability of Ground State Beryllium Clusters**

In this section, binding energies per atom,  $E_b$ , second difference of energies,  $\Delta_2 E$ , vibrational frequencies, HOMO-LUMO gaps (HLGs), and vertical ionization potentials ( $\text{IP}_v$ 's) for ground state pure beryllium clusters are presented and discussed.



#### 4.3.2.1 Binding energy and second difference in energy

The binding energy per atom for the neutral beryllium clusters is calculated according to the eq. 4.1.

$$E_b = \frac{nE(Be) - E(Be_n)}{n}. \quad (4.1)$$

The calculated binding energy per atom  $E_b$  is plotted as a function of the cluster size  $n$ , in Figure 4.3-3. It is interesting to note from this plot that the binding energies per atom of pure beryllium  $Be_n$  clusters, increase rapidly up to  $n=4$  atoms and then there is a gradual increase for  $n=4-6$  atoms. One other part of this plot which shows rapid increase in  $E_b$  is from  $n=6-10$ . For clusters greater than the size of 10 atoms, the increase in  $E_b$  is more regular. This trend in the binding energies of Be clusters is in complete agreement with the previous published theoretical results by Wang et al. [164] and Kawai et al. [183]. Wang et al. [164] contributed the first sharp increase of the binding energies due to the significant decrease in the average bond length and the second rapid increase to the appearance of more highly coordinated structures. The binding energy per atom of the largest cluster studied here ( $n=17$ ) is still lower than the bulk beryllium cohesive energy of 3.32 eV [163] or 3.36 eV [183] per atom.

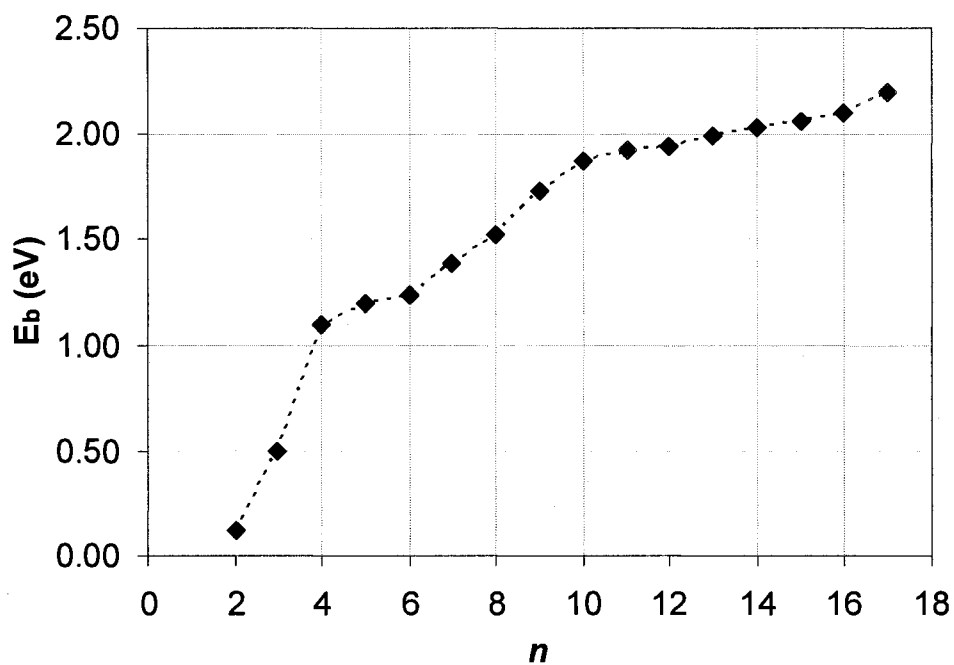


Figure 4.3-3 Plot for binding energy per atom ( $E_b/\text{atom}$ ) versus the cluster size  $n$  for  $\text{Be}_n$  clusters,  $n=2-17$ .

The relative stabilities of the clusters are examined using the second difference of energy  $\Delta_2 E$  which is calculated using the eq. 4.2.

$$\Delta_2 E = E(\text{Be}_{n-1}) + E(\text{Be}_{n+1}) - 2E(\text{Be}_n) \quad (4.2)$$

Figure 4.3-4 shows the plot of the second order finite difference of the calculated total energies plotted against the number of atoms in the cluster.

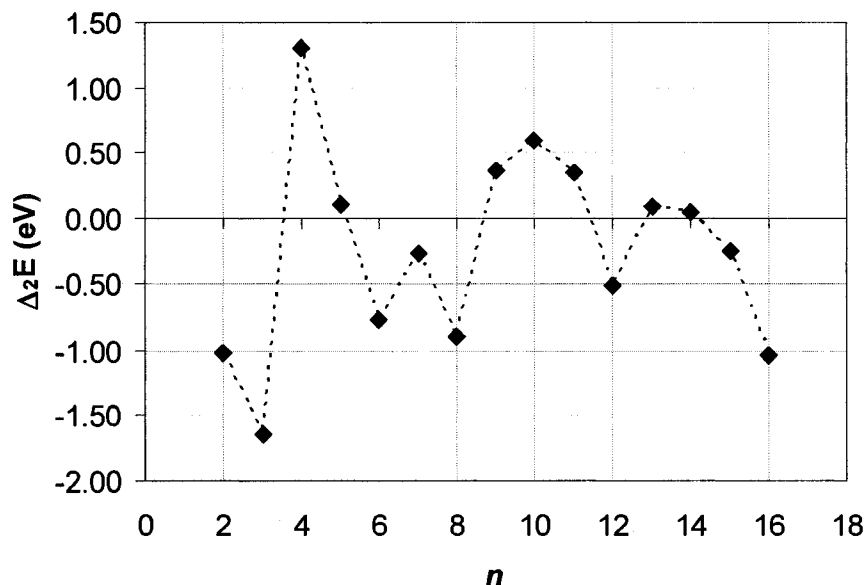


Figure 4.3-4 Plot for second difference of energies versus the cluster size for  $\text{Be}_n$  clusters,  $n=2-17$ .

The quantity  $\Delta_2 E$  can be related to the abundance of clusters measured in the experiments [202]. Within the jellium model, the maxima in these kinds of plots are associated with closure of electronic shells. These maxima are often used as indicators of enhanced local stability. From the figure 4.3-4 we can see that these maxima are observed at  $n=4$ ,  $10$  suggesting their enhanced stability. The 4-atom and 10-atom cluster correspond having eight-electron closed shell which is exactly predicted by the electronic shell model. This result of the enhanced stability of  $\text{Be}_4$  and  $\text{Be}_{10}$  clusters is in perfect agreement with the results of the previous authors.

#### 4.3.2.2 HOMO-LUMO gaps, vertical IPs, EAs

The HLG/band gap is the energy difference between the highest occupied (HOMO) and the lowest unoccupied (LUMO) molecular orbitals. A large HLG for a particular system is symbolic of a closed shell electronic structure with its low reactivity and a higher stability of the system. Few of the reports in the past (by Wang et al.[164] and Cerowski et al.[178]) have discussed the variation of the HLG for pure Beryllium clusters. Ge et al. [203] theoretically studied the structure and electronic properties of the Magnesium doped Be clusters  $MgBe_n$  ( $n=2-12$ ) in which they reported the HOMO-LUMO gaps of the  $Be_{n+1}$  clusters. An interesting point they note is that the magnesium impurity, which is itself a divalent metal atom reduces the HOMO-LUMO gap of pure Be clusters, thereby decreasing the chemical activation of Be cluster. Figure 4.3-5 shows the variation of HLG as a function of the cluster size,  $n$  for pure Beryllium clusters as obtained in our calculations. The values that our calculations predict for the band gaps are larger than the values reported by Wang et al. [164] but the general trend we have observed is in complete agreement with what has been reported. The peaks in the HLG plot of

Figure 4.3-5 can be seen for the  $n$  values of 2, 4, 10 and 17 as reported by Wang et al. [164].

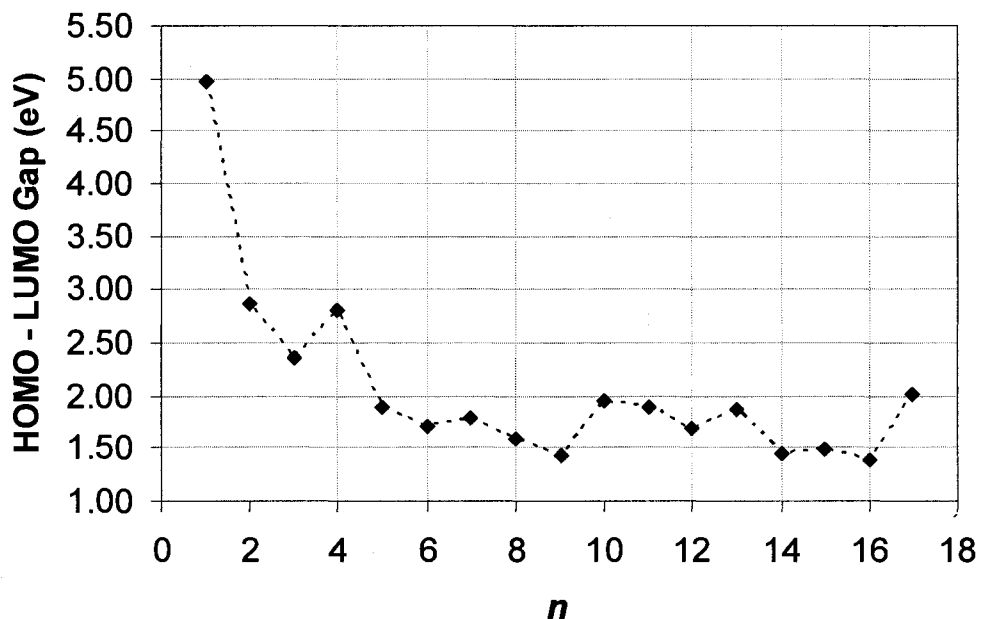


Figure 4.3-5 Plot of HOMO-LUMO gaps versus the cluster size for  $\text{Be}_n$  clusters,  $n=2-17$ .

These large values of HLG are indicative of the enhanced stability of these clusters. The particular stability of these clusters can be associated with the electronic shell model and the magic numbers of total valence electrons of 8, 20 and 34 for  $\text{Be}_2$ ,  $\text{Be}_4$ , and  $\text{Be}_{17}$  clusters respectively. The appearance of the electron shell model in the  $\text{Be}_n$  clusters with only a few atoms already demonstrates some metallic-like features in the pure Be clusters.

The ionization potential is defined as the energy needed for the removal of an electron from the cluster, yielding valuable information on the electronic structure of the cluster [43]. The vertical ionization potential is the 'first order' ionization potential and is calculated using the eq. 4.3

$$IP_v = E(Be_n)^+ - E(Be_n), \quad (4.3)$$

where  $E(Be_n)^+$  is the energy corresponding to the singly positively charged ionic clusters at the neutral  $Be_n$  cluster's geometry.

Figure 4.3-6 shows the vertical Ionization potential of the pure Be clusters as functions of the cluster size, respectively. The ionization potentials IPs, decrease with the increase in size of the clusters. In general a higher value for IP is indicative of the stability of the cluster. The  $IP_v$  values for the pure beryllium clusters are consistent with the electronic shell model with significant peaks at  $n=1, 2, 4, 7$  and  $17$ .

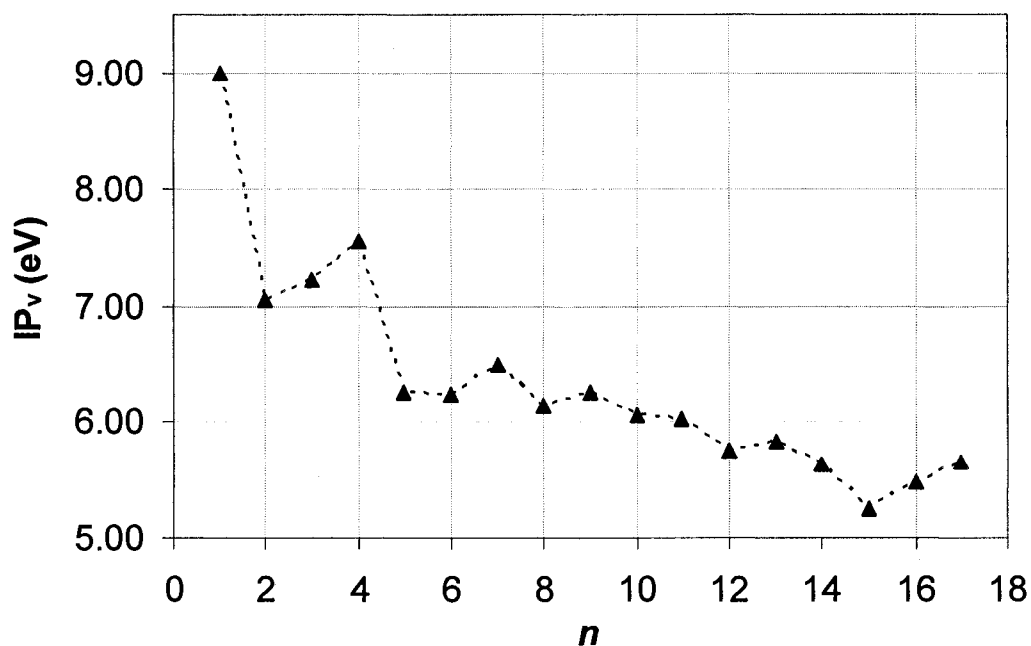


Figure 4.3-6 Plot of vertical ionization potentials versus the cluster size for  $Be_n$  clusters,  $n=1-17$ .

#### 4.4 Conclusions

In conclusion, the geometrical and electronic properties of pure beryllium clusters have been studied by using a B3PW91 density functional. Singlet multiplicity states are favored for  $Be_n$  with  $n= 1-5, 7$  and  $10-17$ , and  $Be_n$  with  $n= 6, 9$  have multiplicity 3 whereas  $Be_8$  has quintet multiplicity. We observe that, while the beryllium dimer is a weakly bound structure with a low binding energy value of 0.11 eV per atom, the binding energies rapidly increase with the cluster size. The binding energy per atom of the largest cluster we have studied, that is  $Be_{17}$  is still

considerably smaller than the cohesive energy of bulk beryllium. The second-order difference in the energies, the HOMO-LUMO gaps and also the vertical ionization potentials are also calculated in our study. We see that  $\text{Be}_n$  with  $n=4$  and 10 have a maxima in the  $\Delta_2E$  plot which is very consistent with the electronic shell model. This, as well as the trends in  $\text{IP}_v$  and the HLG plots, show enhanced stabilities for  $\text{Be}_n$  ( $n=4, 10, 17$ ) clusters.



## CHAPTER 5

### GEOMETRY AND STABILITY OF $\text{Be}_N\text{C}_M$ ( $N=1-10$ ; $M=1, 2, \dots, \text{TO } 11-N$ ) CLUSTERS

Most of the content of this chapter has been published as a full paper. For a complete report on these results, the reader is pointed towards the reference: Mohammed M. Ghouri, Lakshmi Yareeda, and Daniela S. Mainardi, Geometry and Stability of  $\text{Be}_n\text{C}_m$  ( $n=1-10$ ;  $m=1, 2, \dots, \text{to } 11-n$ ) Clusters, *J. Phys. Chem. A*, **2007**, *111* (50), pp 13133-13147.

#### 5.1 Introduction

Over the last decade, a lot of emphasis has been paid to the study of the physical and the chemical properties of atomic clusters [162,204,205], which are aggregates of atoms containing from few to a few thousand atoms [206]. These clusters are known to exhibit strong size-dependent effects and display properties which are significantly different from those of their bulk structures due to a quite large surface-to-volume ratio [206]. The emergence of new research areas like nanoscience and nanotechnology and their promise of different possible technological

applications have further fueled the interest in cluster systems. Main issues in cluster science focus on determining their size-evolutionary patterns based on the clusters unique conformations and stabilities in terms of their energy-related properties. For instance, shell models relate to the formation of 'magic clusters' corresponding to closure of electronic or nuclear shells in clusters, which correlates with enhanced energetic stability [43,194,206,207]. The discovery of clusters with special geometry and stability formed by 'magic' number of atoms is one of the goals of cluster science, since those interesting units can be used to further assemble more complex materials. Extensive theoretical calculations have been conducted to examine structure, energetics and stability of small clusters [208-213] and to explore the potential to assemble crystals from them [214-222].

Experimental determinations of the ground state and isomeric conformations of clusters are currently subtle issues mainly due to practical difficulties in applying structure determination techniques such as Photoelectron Spectroscopy (PES) to such systems. PES provides information about the electronic structure and excitation energies of atomic clusters; however, a difficulty in applying PES to cluster systems is the need for size-

selectivity due to size resolution issues [223]. Hence, many studies on the electronic structure of clusters have been focused on size-selected neutral clusters [224], such as  $\text{As}_2$ ,  $\text{As}_4$  and  $\text{P}_4$  [225], and the photo-detachment of negatively-charged clusters [226,227]. Theoretical studies, on the other hand, allow detailed investigation of ground states and their higher energy isomers that may appear to be the preferred stable structures at particular operating conditions. A comparison of experimental PES data with theoretical calculations has become a valuable means to determine the structures and low-lying isomers for a variety of clusters. Thus, theoretical and experimental studies of clusters are very useful for the understanding of electronic, chemical, and physical properties and prediction of the cluster local chemistry [228]. In particular, theoretical methods [120] based on solutions to the Schrödinger equation provide accurate characterization of cluster structures [229,230].

Many studies have been performed on small pure carbon clusters [231-238] and carbon-containing clusters [208,239-242]. Moreover, since they form the basic structural units of new materials with potential applications, for instance in astrochemistry/physics [243], heteroatom-doped carbon clusters have been a topic of many theoretical

investigations [243,244]. Recently, much attention has been paid to the study of beryllium-doped carbon clusters since the addition of beryllium provides a means to stabilize the highly reactive linear carbon chains for applications in astrophysics [165,166,245,246]. This particular interest yielded to the extensive theoretical investigations of heteroatom-doped carbon clusters of the form  $C_nBe^{2-}$  ( $n=4-14$ ) [165],  $BeC_{2n}^{2-}$  ( $n=2-6$ ) [245], and  $BeC_n^-$  ( $n=1-8$ ) [166], since these species were particularly observed experimentally [246]. Chen et al. [165] performed DFT calculations on  $C_nBe^{2-}$  ( $n=4-14$ ) using the B3LYP Density Functional theory (DFT) method in combination with the 6-31G\* basis set, and found that the ground state structures of the clusters are linear chains with the beryllium atom located inside the  $C_n$  chain. Zhang [245] studied  $BeC_{2n}^{2-}$  ( $n=2-6$ ) at the hybrid B3LYP functional and 6-311+G(2df) theory level and reported that linear chains correspond to the ground states of metastable  $C_2BeC_2^{2-}$ , and highly stable  $C_2BeC_4^{2-}$ ,  $C_4BeC_4^{2-}$ ,  $C_4BeC_6^{2-}$ ,  $C_6BeC_6^{2-}$  clusters. In a more recent study, Chen et al. [166] investigated  $BeC_n^-$  ( $n=1-8$ ) clusters using B3LYP/6-311+G\*//B3LYP/6-31G\* theory levels and found that these clusters with even  $n$  are more stable than the ones with odd  $n$ . They attribute such an even/odd alternation in the stabilities of these systems to trends observed in the

local positive charge of the Be atom, electron affinity, variations in bond lengths, incremental binding energy and dissociation channels [166].

Not only ionic carbon-heteroatom cluster systems were worth of extensive research. With the discovery of the Metallo-carbohedrenes (Metcars) of the form  $M_mC_n$  where M is any metal (mostly a transition metal) by Castleman et al. [247-249], carbon-metal and also carbon- non-metal neutral systems have been investigated comprehensively. In particular, studies with different carbon- 'non-metals' clusters such as carbon-nitrogen [240] and carbon-silicon [208,250] have been the focus of attention for applications in astrophysics [242,251] and electronics [208] respectively. Belbruno et al. [240] studied the structural stability and the energetics of up to 12-atom clusters of C-N using the density functional B3LYP in combination with the cc-PVTZ basis set. These authors confirmed at that theory level that linear carbon chains with the nitrogen atoms at the terminal positions are the global minima (ground states) of C-N structures with one or two nitrogen atoms. They predicted that this is the case for up to a total number of 13 carbon atoms and contrasted this with the pure carbon clusters, where the cyclic rings are energetically favorable when the cluster size is 9 or

greater [234]. Pradhan et al. [208] studied the electronic properties and the geometrical structures of small carbon-silicon clusters of the form  $\text{Si}_m\text{C}_n$  ( $1 \leq m, n \leq 4; n \leq m$ ). Using DFT Local Density Approximation (LDA) in conjunction with the 6-311++G\*\* basis set, these authors reported that the  $\text{Si}_3\text{C}_3$  cluster is candidate for a 'magic cluster' with a very high stability based on their reported electronic properties such as, the HOMO-LUMO Gaps, vertical Ionization Potentials ( $\text{IP}_v$ ) and the vertical Electron Affinities ( $\text{EA}_v$ ). They also reported that the clusters with equal number of silicon and carbon atoms tend to be particularly stable [208].

The discovery of carbon nanotubes [24] and other carbon-related nanostructures such as fullerenes [252] has taken the interest in carbon and its related clusters even further. Of particular importance is the potential hydrogen storage capacity of carbon-based nanostructures [253]. For instance, fullerenes have a limited capacity to hold certain number of endohedral substituents depending on their sizes. However, in some cases, the insertion of dopants such as lithium [254] or beryllium [255] have shown promise of enhanced hydrogen storage capacity of carbon-doped nanostructures. Hence, alkali metal-doped [256,257] and alkaline earth metal-doped [258], especially beryllium-

doped carbon nanostructures [255,259] are considered to be likely candidates for hydrogen storage materials. Metal hydrides are also being considered for hydrogen storage applications [16]. In particular, lithium beryllium hydrides are the lightest reversible complex metal hydrides with promising gravimetric hydrogen storage capacities (more than 8 wt.%) [260]; however, the high temperature needed for hydrogen desorption ( $\sim 150^\circ\text{C}$ ) is a major drawback [260]. The possibility of using carbon as dopant in such hydrides might reduce the temperature for hydrogen desorption, as it clearly happens in the case of magnesium hydrides [115,116], making the Li-Be-C hydrides attractive complex metal hydrides for hydrogen storage applications. The interest of this study is therefore, to advance the knowledge of structure and energetics of Be-C neutral clusters for the prediction of highly stable 'magic clusters' with potential use in diverse technological applications such as hydrogen storage. Therefore, it is of fundamental importance to study the size dependence of electronic and geometric structures of Be-C clusters as functions of both particle size and composition. In this paper, a systematic study on the neutral beryllium-carbon clusters of the form  $\text{Be}_n\text{C}_m$  ( $n=1-10$ ;  $m=1, 2, \dots$ , to  $11-n$ ) is performed. According to this notation, for each  $n$  value, 1

$\leq n \leq 10$ ,  $m$  can take the values 1, 2, ..., up to  $11-n$ . The fundamental work presented in this chapter has served us with a better understanding of the carbon doped beryllium-based light metal hydrides such as  $\text{Li}_2\text{BeH}_4$ , and therefore aid in tailoring novel materials for such aforementioned applications.

## 5.2 Methodology

Density Functional Theory (DFT) calculations of  $\text{Be}_n\text{C}_m$   $n=1-10$ ,  $m=1, 2, \dots$ , to  $11-n$  neutral (zero total charge) clusters are performed using the Gaussian 03 program, Revision C.02 [228]. A large variety of possible geometrical arrangements of these clusters are investigated, including three-dimensional (3-D), cyclic, and linear configurations where  $n$  beryllium and  $m$  carbon atoms are placed in different ways they can group. The density functional employed in these calculations is the B3PW91, one of the most successful hybrid functionals [196], that includes an exchange description constituted by contributions of local, nonlocal (Becke 3-parameter) and Hartree-Fock exchange terms, and correlation given by the 1991 Perdew and Wang (PW91) nonlocal GGA functional [120], This DFT method is used in combination with the 6-31+G\* basis set, which is a split-valence double-zeta that



considers *d*-like polarization functions on heavy atoms and a set of diffuse *s*- and *p*-like functions on heavy atoms [120].

Geometry optimizations and harmonic vibrational frequency calculations for all the 55  $\text{Be}_n\text{C}_m$   $n=1-10$ ,  $m=1, 2, \dots$ , to  $11-n$  neutral ground state clusters, 38 different spin multiplicity  $(2S+1)$  state clusters, and 113 isomers are performed to ensure that stationary points on the potential energy surface of the clusters are in fact local minima. Spin multiplicity states are checked in all calculations and ground state geometries as well as stable higher-energy isomers are presented. Zero-point corrected absolute energies are used for further calculation of binding energies and second differences in energy.

### **5.3 Results and Discussion**

#### **5.3.1 Ground State Conformations and Isomers**

To preserve the clarity of this dissertation, the extraneous details of the geometric structures and the bond lengths of all the 55  $\text{Be}_n\text{C}_m$   $n=1-10$ ,  $m=1, 2, \dots$ , to  $11-n$  neutral ground state clusters, 38 different spin multiplicity  $(2S+1)$  state clusters, and 113 isomers are avoided here. However, these can be found in considerable detail in our published report [261].

### 5.3.2 Stability of Ground State Clusters

In this section, binding energies per atom,  $E_b$ , second differences in energies,  $\Delta_2E(m)$ , HOMO-LUMO gaps, HLG, and vertical ionization potentials ( $IP_v$ ) and electron affinities ( $EA_v$ ) for ground state  $Be_nC_m$  cluster ( $n=1-10$ ,  $m=1, 2, \dots$ , to  $11-n$ ) clusters are presented and discussed. Table 5.3-A summarizes the calculated values of  $E_b$ , HLG,  $IP_v$ ,  $AE_v$ , and  $\Delta_2E(m)/n$  for this clusters, which are ordered according to  $E_b$  from the most to the least stable for decreasing  $N (=n+m)$  value. All these energy-related properties are then used for the identification of magic  $Be_nC_m$  clusters.

#### 5.3.2.1 Binding energy and second difference in energy

The binding energy per atom for the neutral clusters is calculated according to eq. 5.1

$$E_b = \frac{mE(C) + nE(Be) - E(Be_nC_m)}{N}, \quad (5.1)$$

where  $E(C)$  is the energy of a single carbon atom,  $E(Be)$  is the energy of a single Be atom,  $E(Be_nC_m)$  is the energy of the  $Be_nC_m$  cluster ( $n=1-10$ ,  $m=1, 2, \dots$ , to  $11-n$ ), and  $N$  is the total number of atoms in the cluster ( $N=n+m$ ).

The calculated binding energy per atom  $E_b$  is plotted as a function of the cluster size,  $N$ , in Figure 5.3-1. It is interesting to notice that  $BeC_m$  ( $m=1-9$ ) show the highest

binding energy per atom for  $2 \leq N \leq 9$  and  $N=11$ , while  $\text{Be}_2\text{C}_8$  shows a slightly higher binding energy per atom (5.34 eV) than  $\text{BeC}_9$  (5.30 eV) for  $N=10$  (Table 5.3-A). Hence, it is reasonable to conclude that  $\text{Be}_n\text{C}_m$  clusters containing 1 Be atom seem to be the most stable ones. On the other hand, the lowest  $E_b$  value is always reached by the highest possible value of  $n$  in each  $\text{Be}_n\text{C}_m$  cluster (Figure 5.3-1, Table 5.3-A). It is also observed that the clusters with odd number of beryllium atoms,  $n$ , (Figure 5.3-1, filled symbols) show comparatively higher binding energies than the clusters containing even number of beryllium atoms (Figure 5.3-1, empty symbols), which makes them relatively more stable.

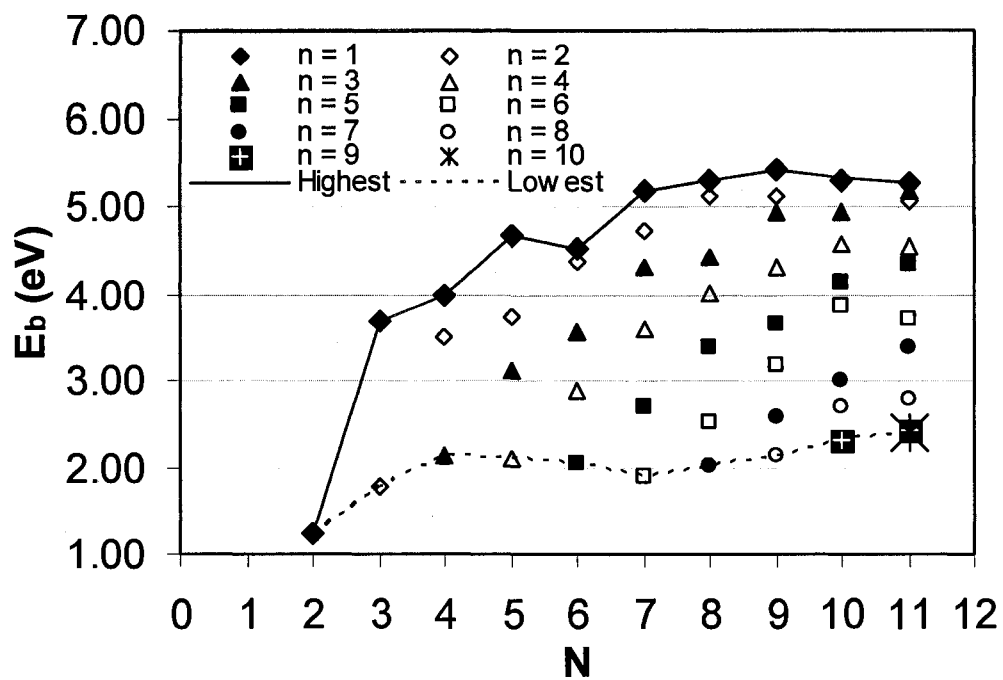


Figure 5.3-1 Binding energy per atom as a function of the cluster size  $N (=n+m)$  for  $\text{Be}_n\text{C}_m$  ( $n=1-10$ ;  $m=1, 2, \dots, \text{to } 11-n$ ) clusters.

Table 5.3-A Calculated  $\Delta_2E(m)$ , homo-lumo gap (Gap),  $IP_v$ , and  $AE_v$  for  $Be_nC_m$  ( $n=1-10$ ;  $m=1, 2, \dots$  to  $11-n$ ) clusters. Clusters are ordered according to  $\Delta_2E(m)$  from the most (bold) to the least stable in terms of  $E_b$  for decreased  $N$  ( $=n+m$ ) value.

N	n	m	$E_b$ (eV)	HLG (eV)	$IP_v$ (eV)	$EA_v$ (eV)	$\Delta_2E(m)/n$ (eV)	N	n	m	$E_b$ (eV)	HLG (eV)	$IP_v$ (eV)	$EA_v$ (eV)	$\Delta_2E(m)/n$ (eV)
11	1	10	<b>5.26</b>	3.04	6.84	3.47	-	8	1	7	<b>5.30</b>	2.49	8.22	3.66	-0.11
11	3	8	5.18	<b>4.72</b>	<b>8.01</b>	2.14	-	8	2	6	5.11	<b>5.14</b>	<b>9.46</b>	<b>2.04</b>	1.17
11	2	9	5.05	2.71	6.22	3.64	-	8	3	5	4.44	4.41	8.67	2.87	-1.21
11	4	7	4.54	2.58	5.98	2.63	-	8	4	4	4.02	3.49	8.10	2.51	0.10
11	5	6	4.33	3.48	6.94	<b>1.86</b>	-	8	5	3	3.39	1.92	6.05	2.48	0.47
11	6	5	3.73	1.19	5.34	3.40	-	8	6	2	2.54	1.15	5.82	3.41	-0.22
11	7	4	3.37	2.35	5.25	3.90	-	8	7	1	2.01	2.92	6.20	2.15	0.03
11	8	3	2.80	1.61	5.65	2.71	-	7	1	6	<b>5.17</b>	3.81	<b>8.95</b>	2.57	<b>2.80</b>
11	9	2	2.43	1.43	5.38	3.01	-	7	2	5	4.74	<b>4.50</b>	8.44	2.68	-0.36
11	10	1	2.40	2.03	5.76	2.65	-	7	3	4	4.32	3.98	8.47	<b>1.94</b>	<b>1.18</b>
10	2	8	<b>5.34</b>	4.17	<b>8.28</b>	2.72	<b>2.50</b>	7	4	3	3.60	2.88	6.91	1.96	0.24
10	1	9	5.30	2.93	7.15	3.74	-0.55	7	5	2	2.70	1.75	5.96	2.13	-0.33
10	3	7	4.94	<b>4.44</b>	7.55	2.80	-0.85	7	6	1	1.89	2.59	6.03	2.58	-0.19
10	4	6	4.58	2.81	6.80	2.78	0.75	6	1	5	<b>4.54</b>	3.04	8.38	2.68	-5.06
10	5	5	4.13	3.01	6.47	2.07	0.39	6	2	4	4.38	<b>3.63</b>	<b>8.46</b>	<b>1.81</b>	<b>0.31</b>
10	6	4	3.87	3.74	6.32	<b>1.31</b>	1.27	6	3	3	3.57	1.64	7.10	2.88	-0.97
10	7	3	3.01	2.14	5.81	3.22	-0.01	6	4	2	2.88	2.15	6.63	1.90	-0.29
10	8	2	2.71	1.52	5.77	2.91	0.52	6	5	1	2.05	1.76	6.48	2.29	-0.05
10	9	1	2.32	2.43	5.41	2.62	0.44	5	1	4	<b>4.66</b>	3.91	<b>9.73</b>	2.38	<b>3.38</b>
9	1	8	<b>5.41</b>	3.58	7.98	2.68	<b>2.02</b>	5	2	3	3.75	<b>5.54</b>	7.33	2.13	-1.40
9	2	7	5.13	3.91	7.54	3.37	-0.93	5	3	2	3.12	2.71	7.07	1.55	0.40
9	3	6	4.93	<b>5.13</b>	<b>8.95</b>	<b>2.03</b>	<b>1.30</b>	5	4	1	2.11	4.22	6.61	<b>1.04</b>	-0.20
9	4	5	4.30	2.73	7.90	3.48	-0.14	4	1	3	<b>4.00</b>	1.96	<b>8.09</b>	2.58	-2.36
9	5	4	3.67	2.47	6.09	2.64	-0.48	4	2	2	3.50	<b>6.26</b>	7.49	<b>1.13</b>	<b>1.97</b>
9	6	3	3.19	2.42	5.97	2.44	-0.26	4	3	1	2.13	2.99	6.89	2.33	-0.01
9	7	2	2.57	1.73	5.66	2.69	0.01	3	1	2	<b>3.68</b>	<b>3.39</b>	<b>9.35</b>	2.13	<b>3.59</b>
9	8	1	2.13	2.88	5.85	2.58	-0.12	3	2	1	1.77	3.04	7.43	<b>2.03</b>	-1.81
								2	1	1	1.24	2.86	9.60	0.44	-6.06

In Figure 5.3-1 the minimum (dotted line) binding energy trend curve shows a clear change of behavior at  $N=7$ , value after which this curve increases almost linearly with  $N$ , possibly indicating an intrinsic change in the behavior of small BeC clusters. In order to elucidate this point, the relative stabilities of the clusters upon the addition or elimination of a carbon atom are calculated using the second difference of energy  $\Delta_2 E(m)$ , which is calculated as shown in eq. 5.2

$$\Delta_2 E(m) = E(\text{Be}_n \text{C}_{m-1}) + E(\text{Be}_n \text{C}_{m+1}) - 2E(\text{Be}_n \text{C}_m), \quad (5.2)$$

where  $E(\text{Be}_n \text{C}_{m-1})$ ,  $E(\text{Be}_n \text{C}_{m+1})$ , and  $E(\text{Be}_n \text{C}_m)$ , are the energies of the  $n$ -beryllium  $\text{Be}_n \text{C}_{m-1}$ ,  $\text{Be}_n \text{C}_{m+1}$ , and  $\text{Be}_n \text{C}_m$  clusters ( $n=1-10$ ,  $m=1, 2, \dots$ , to  $11-n$ ) respectively. As mentioned in the Chapter 4 on pure beryllium clusters, in cluster physics [194,262], the second difference in energy can be used to search for 'magic clusters'. This quantity represents the relative stability of a pure cluster with respect to its two immediate neighbors and can be compared directly to the experimental abundance [194]. Since this study does not consider pure clusters, i.e. formed by only one type of element, two equations for the second difference in energy can be written, one at constant  $n$ ,  $\Delta_2 E(m)$ , and the other at constant  $m$ ,  $\Delta_2 E(n)$ . Both possibilities were explored, but

$\Delta_2 E(m)$  is presented here due to its clearer trends and ease to follow the organization of this chapter.

Equation 5.2 for  $\Delta_2 E(m)$  can be rewritten as the sum of two differences as shown in eq. 5.3

$$[E(\text{Be}_n\text{C}_{m-1}) - E(\text{Be}_n\text{C}_m)] + [E(\text{Be}_n\text{C}_{m+1}) - E(\text{Be}_n\text{C}_m)]. \quad (5.3)$$

The first difference in the above equations is the relative stability of  $\text{Be}_n\text{C}_m$  with respect to the addition of a carbon atom to the  $\text{Be}_n\text{C}_{m-1}$  cluster, and the second difference is the relative stability of  $\text{Be}_n\text{C}_m$  with respect to the elimination of a carbon atom from the  $\text{Be}_n\text{C}_{m+1}$  cluster. Hence, if  $\text{Be}_n\text{C}_m$  is indeed more stable than its neighbors, then both differences and therefore  $\Delta_2 E(m)$  are positive. In order to "normalize"  $\Delta_2 E(m)$  and get rid of relative comparisons between all ground state clusters, the quantity  $\Delta_2 E(m)/n$ , where  $n$  is the number of Be atoms in the cluster, is considered instead. Hence,  $\Delta_2 E(m)/n$  provides a qualitative measure of absolute  $\text{Be}_n\text{C}_m$  cluster stability upon the addition and removal of one carbon atom to the clusters.

In Figure 5.3-2 the  $n$  value that gives the highest and the lowest  $\Delta_2 E(m)/n$  per each  $N$  is plotted as a function of  $N$ . According to this Figure, it is evident that the highest  $\Delta_2 E(m)/n$  is always achieved by  $n=1$  for odd  $m$  and  $n=2$  for even  $m$ , and that the lowest  $\Delta_2 E(m)/n$  is achieved by  $n=2$

for odd  $m$  in  $\text{Be}_n\text{C}_m$  respectively and irrespective of the cluster size  $N$ . However, when  $N$  is even and  $N > 6$ , a different behavior is observed since the lowest  $\Delta_2E(m)/n$  values are obtained by  $n=3$ . Therefore, it is concluded that the highest  $\text{Be}_n\text{C}_m$  cluster stability with respect to the addition or removal of a carbon atom is achieved by  $\text{BeC}_m$  (odd  $m$ ) and  $\text{Be}_2\text{C}_m$  (even  $m$ ) irrespective of the total number of atoms in the cluster. Moreover,  $\text{Be}_2\text{C}_m$  (odd  $m$ ),  $\text{BeC}_m$  ( $m=4$  and  $6$ ) and  $\text{Be}_3\text{C}_m$  (odd  $m=8$  and  $10$ ) clusters are the least stable with respect to the addition or removal of a carbon atom (Figure 5.3-2).

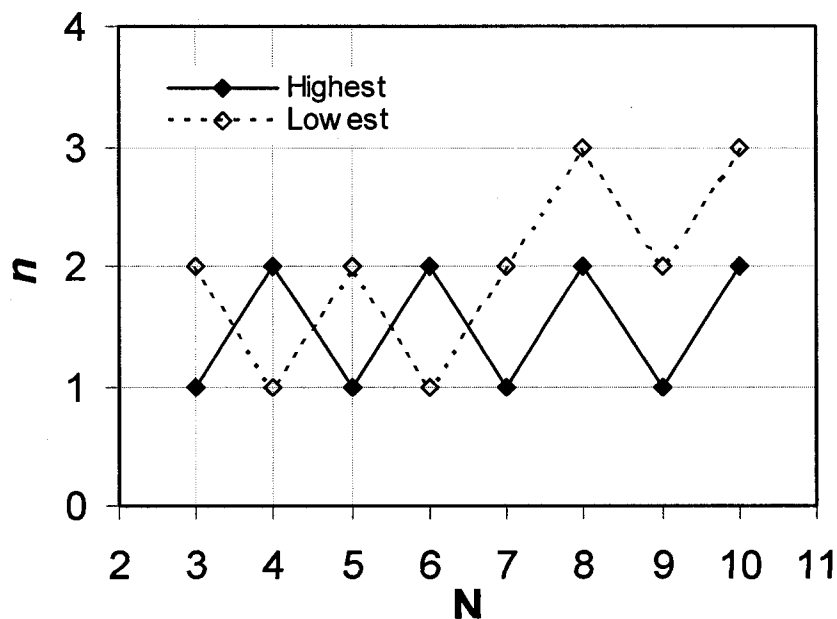


Figure 5.3-2  $n$  vs.  $N$  for the highest and lowest  $\Delta_2E(m)/n$  according to Table 5.3-A.



Thus, two different trends are observed from Figure 5.3-2 for  $N < 7$  and  $N > 7$  with respect to the number of beryllium atoms that minimize  $\Delta_2 E(m)/n$  per each  $N$ , explaining the intrinsic change in the behavior of small BeC clusters at  $N=7$  in the minimum binding energy trend curve of Figure 5.3-1.

Figures 5.3-3 and 5.3-4 show the behavior of  $\Delta_2 E(m)/n$  as a function of  $n$  for odd and even total number of atoms,  $N=n+m$ , in the  $\text{Be}_n\text{C}_m$  clusters, respectively. It can be noted that there is an even-odd alternation in these  $\Delta_2 E(m)/n$  values with  $n$ . This figure clearly shows that clusters with odd  $n$  and  $N$  (Figure 5.3-3), and clusters with even  $n$  and  $N$  (Figure 5.3-4) are particularly stable.

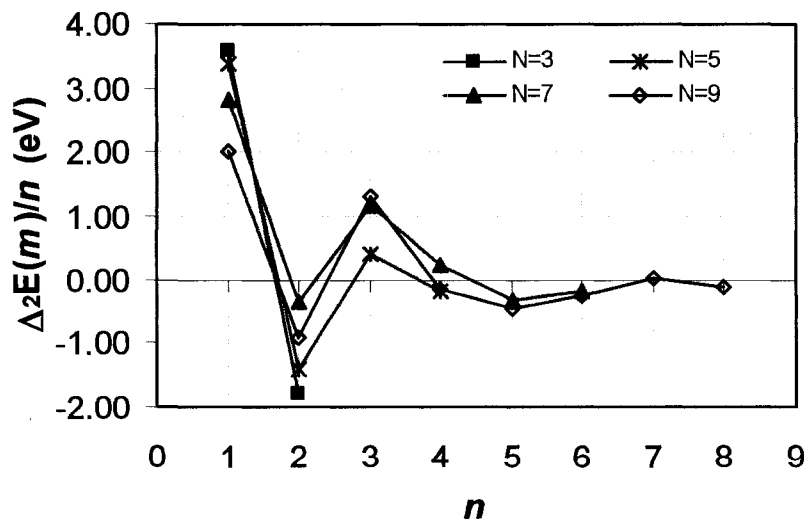


Figure 5.3-3 Second difference in energy per beryllium atom,  $\Delta_2 E(m)/n$ , vs. number of beryllium atoms,  $n$ , for odd total number of atoms in the cluster,  $N=n+m$ .

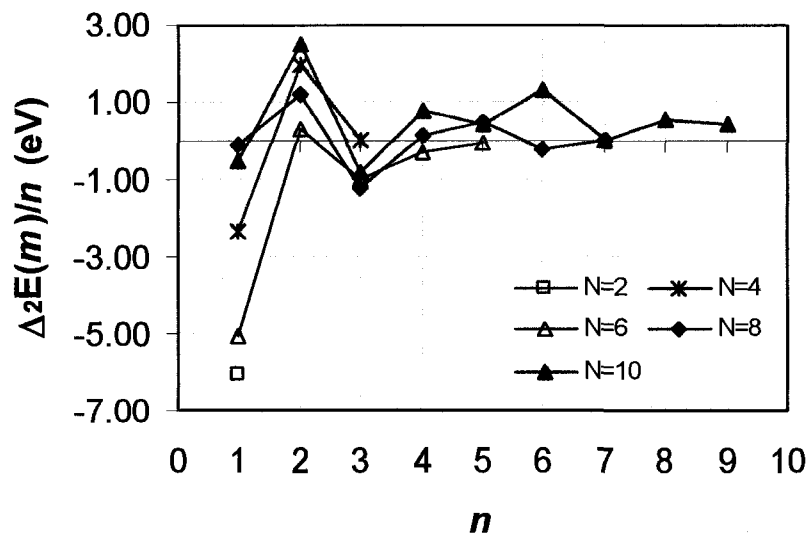


Figure 5.3-4 Same as Figure 5.3-3 for even total number of atoms in the cluster.

#### 5.3.2.2 HOMO-LUMO gap, vertical IPs and EAs

The HOMO-LUMO gap (HLG)/ band gap is the energy difference between the highest occupied (HOMO) and the lowest unoccupied (LUMO) molecular orbitals. Figure 5.3-5 shows the variation of HLG as a function of the cluster size  $N$ . It is interesting to notice that the highest HLG is observed when  $n=1$ ,  $n=2$ , and  $n=3$  for  $N=3$ , 4-8, and 9-11 respectively. Similarly, the lowest HLG is observed when  $n=2$ , 1, 3, 3, 5, 6, 7, 8, and 6 for  $N=3-11$  respectively. Overall, the highest and lowest HLG is reached by  $\text{Be}_2\text{C}_2$  and  $\text{Be}_6\text{C}_2$  respectively (Figure 5.3-5).

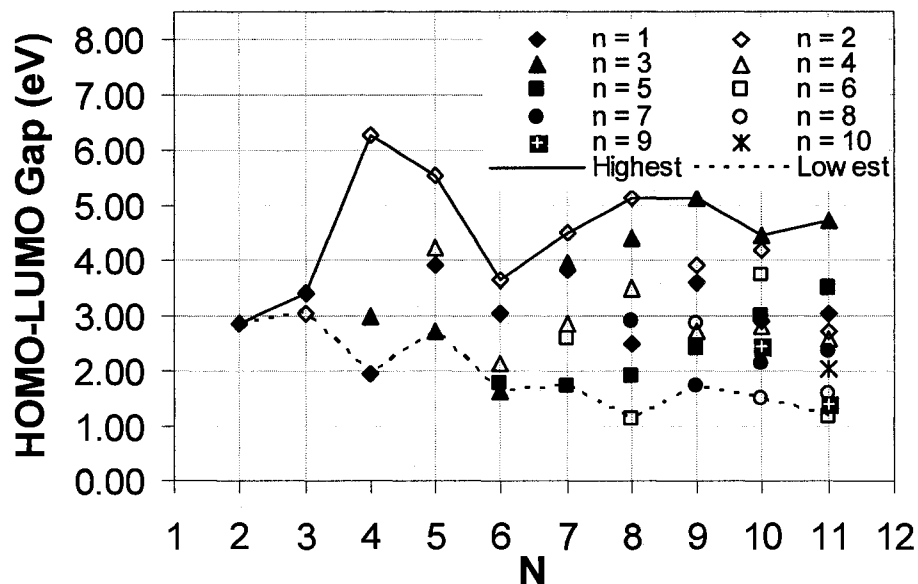


Figure 5.3-5 HOMO-LUMO gaps as a function of number of atoms in the cluster ( $N=n+m$ ) for  $Be_nC_m$  ( $n=1-10$ ;  $m=1, 2, \dots$ , to  $11-n$ ) neutral clusters.

The ionization potential and the electron affinity are defined as the energy needed for the removal of an electron from the cluster, and the energy released when an extra electron is added to the neutral atom respectively, yielding valuable information on the electronic structure of the cluster [43]. The vertical ionization potential,  $IP_v$ , and vertical electron affinity,  $EA_v$ , are 'first order' ionization potentials and electron affinities respectively, and are calculated using the eqs. 5.4 and 5.5

$$IP_v = E [Be_nC_m]^+ - E [Be_nC_m], \quad (5.4)$$

$$EA_v = E [Be_nC_m] - E [Be_nC_m]^{-}, \quad (5.5)$$

where  $E[\text{Be}_n\text{C}_m]^+$  and  $E[\text{Be}_n\text{C}_m]^-$  are the energies corresponding to singly positively and negatively charged cluster at the neutral cluster's geometry, respectively.

Figures 5.3-6 and 5.3-7 show the  $\text{IP}_v$  and  $\text{EA}_v$  as functions of the cluster size respectively. The solid and dotted lines in Figures 5.3-6 and 5.3-7 join the highest and the lowest calculated  $\text{IP}_v$  and  $\text{EA}_v$  values for each  $N$ .

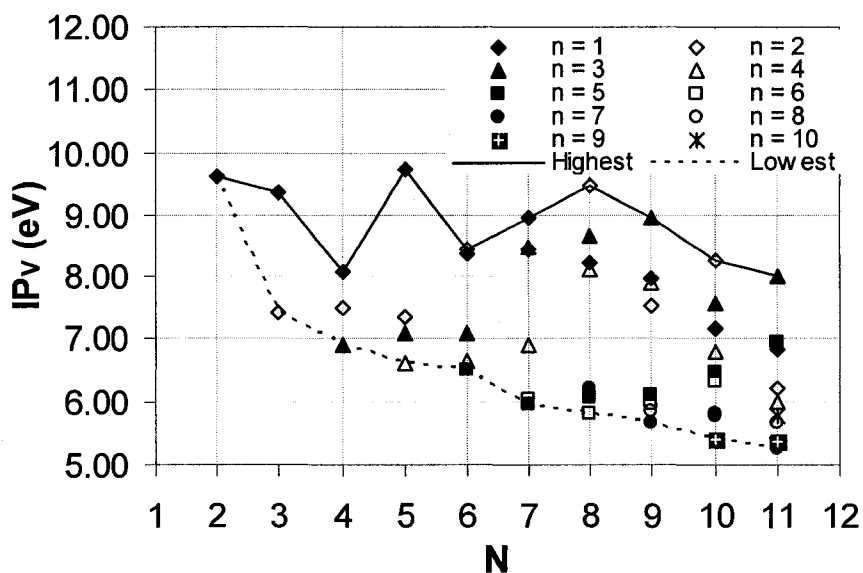


Figure 5.3-6 Vertical ionization potential,  $\text{IP}_v$ , as functions of  $N$  ( $=n+m$ ) for all the  $\text{Be}_n\text{C}_m$  ( $n=1-10$ ;  $m=1, 2, \dots$ , to  $11-n$ ) neutral ground state clusters.

It is interesting to notice that  $\text{IP}_v$  is maximum at  $n=1$ ,  $n=2$ , and  $n=3$  for  $N=3-5$ , and 7,  $N=6$ , 8 and 10, and  $N=9$  and 11 respectively. The  $\text{IP}_v$  minimum is found when  $n=2, 3, 4, 5, 5, 6, 7, 9$ , and 7 for  $N=3-11$  respectively (Figure 5.3-6). On the other hand,  $\text{EA}_v$  is maximum at  $n=1, 1, 1, 3, 2$ ,

1, 4, 1, and 7 for  $N=3-11$ , and it is minimum when  $n=2, 2, 4, 2, 3, 2, 3, 6,$  and  $5$  for  $N=3-11$  respectively.

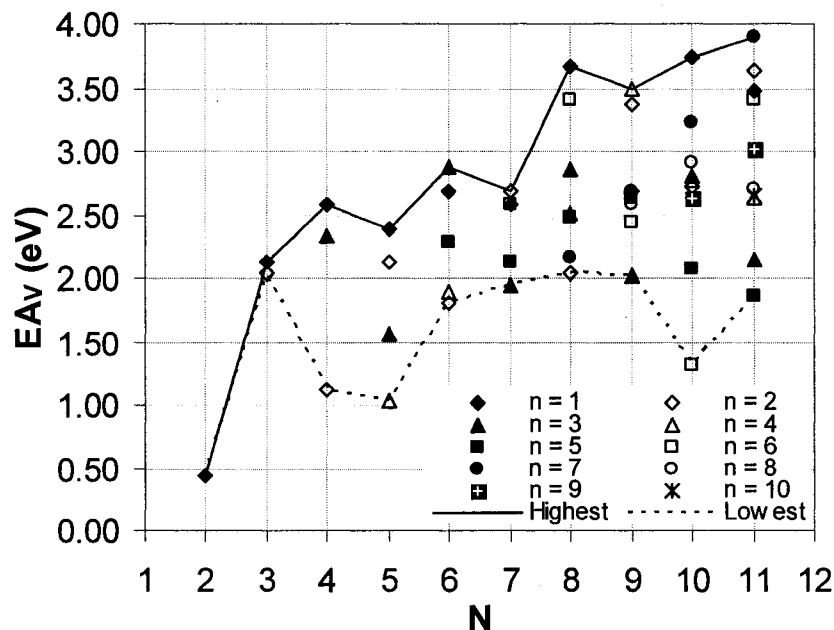


Figure 5.3-7 Vertical electron affinity,  $EA_v$ , as functions of  $N$  ( $=n+m$ ) for all the  $Be_nC_m$  ( $n=1-10$ ;  $m=1, 2, \dots$ , to  $11-n$ ) neutral ground state clusters.

### 5.3.2.3 Magic numbers

The stability of  $Be_nC_m$  ( $n=1-10$ ;  $m=1, 2, \dots$ , to  $11-n$ ) clusters can be discussed on the basis of the binding energy per atom,  $E_b$ , the HOMO-LUMO gap, HLG, the vertical ionization potential,  $IP_v$ , the vertical electron affinity,  $EA_v$ , and the second difference in energy per beryllium atom,  $\Delta_2E(m)/n$ . In Table 5.3-A  $E_b$ , HLG,  $IP_v$ ,  $EA_v$ , and  $\Delta_2E(m)/n$  of the  $Be_nC_m$  ground state structures are reported, where clusters are ordered per each  $N$  from the most to the least

stable (in terms of  $E_b$ ) for decreased  $N$ . Hence, the most and least stable clusters correspond to the cases for which  $E_b$  are the highest and lowest respectively per  $N$ . In Table 5.3-A the highest  $E_b$ , HLG,  $IP_v$  and lowest  $EA_v$  are in bold for clear visualization of clusters with particular stability. In addition, when a cluster has any of those quantities highlighted,  $\Delta_2E(m)/n$  is also highlighted when positive. Note that for clusters containing a total of 11 atoms, no value for  $\Delta_2E(m)/n$  is reported since their calculations required information about clusters containing 12 atoms, which were not studied in this work.

Table 5.3-A clearly shows that  $BeC_m$  ( $m=1-9$ ) clusters have the highest binding energy per atom for  $2 \leq N \leq 9$  and  $N=11$ , while  $Be_2C_8$  shows a slightly higher binding energy per atom (5.34 eV) than  $BeC_9$  (5.30 eV) for  $N=10$  as discussed previously. The most stable 5-, 7- and 10-atom clusters are the ones that exhibit the highest  $E_b$ ,  $IP_v$  and  $\Delta_2E(m)/n$ . The most stable 4-atom cluster is the one that exhibit the highest  $E_b$  and  $IP_v$ . The most stable 6-, 8- and 11-atom clusters are the ones that exhibit the highest  $E_b$ . The most stable 9-atom cluster is the one that exhibits the highest  $E_b$  and  $\Delta_2E(m)/n$ . Finally, the most stable 3-atom cluster is the one that exhibits the highest  $E_b$ , HLG,  $IP_v$ , and

$\Delta_2E(m)/n$ . No correlation has been found between  $EA_v$  and cluster stability.

According to Table 5.3-A, at particular values of  $n$  and  $m$  certain  $Be_nC_m$  clusters show particular stability and are expected to have higher abundance than their neighboring clusters. Clusters having two or more properties highlighted and a positive  $\Delta_2E(m)/n$  in Table 5.3-A are considered particularly stable. These clusters ( $Be_2C_8$ ,  $Be_3C_6$ ,  $Be_2C_6$ ,  $BeC_6$ ,  $Be_2C_4$ ,  $BeC_4$ ,  $Be_2C_2$ , and  $BeC_2$ ) are then referred to as clusters of 'magic numbers', indicating that the clusters with these values of  $n$  are more stable than their neighboring clusters. The particularly high stability of  $BeC_2$ ,  $BeC_4$ ,  $BeC_6$ , can be understood in view of the magic numbers of total valence electrons of 10, 18, and 26 respectively. On the other hand, the particularly high stability of  $Be_2C_2$ ,  $Be_2C_4$ ,  $Be_2C_6$ ,  $Be_2C_8$ , and  $Be_3C_6$  clusters containing 12, 20, 28, 36, and 30 total valence electrons respectively, may be due to atomic structure effects.

#### 5.4 Conclusions

Structure and stability of  $Be_nC_m$  ( $n=1-10$ ;  $m=1, 2, \dots$ , to  $11-n$ ) clusters have been carried at the B3PW91/6-31+G\* Density Functional Theory level. The most stable planar cyclic conformations always show at least a set of two

carbon atoms between two beryllium atoms, while structures where beryllium atoms cluster together, or allow the intercalation of one carbon atoms between two of them generally seem to be the least stable ones. The stability of  $\text{Be}_n\text{C}_m$  ground clusters is discussed on the basis of their binding energy per atom, HOMO-LUMO gap, vertical ionization potential, vertical electron affinity, and second difference in energy per beryllium atom.  $\text{Be}_2\text{C}_8$ ,  $\text{Be}_3\text{C}_6$ ,  $\text{Be}_2\text{C}_6$ ,  $\text{BeC}_6$ ,  $\text{Be}_2\text{C}_4$ ,  $\text{BeC}_4$ ,  $\text{Be}_2\text{C}_2$ , and  $\text{BeC}_2$  are identified as clusters of 'magic numbers', and may be further considered in the assembly of more complex structures with unique properties for technological applications.



## CHAPTER 6

### THE INTERACTIONS OF C-BE CLUSTERS WITH HYDROGEN AND NOVEL C-BE BASED LITHIUM METAL HYDRIDES

In Chapters 4 and 5, we studied the pure beryllium and carbon-beryllium clusters respectively. After having got the information about their ground state geometries and the higher energy isomers at a relatively better level of theory (DFT, B3PW91) in those chapters, we employed the same level of theory to investigate into the stability of these clusters by looking at the electronic properties such as the binding energy per atom, second order difference in the energies, HOMO-LUMO gaps, vertical ionization potentials and the electron affinities.

In Chapter 6 we extend the results from the last two chapters to study the interactions of hydrogen molecule with the C-Be clusters studied in Chapter 5. Initially we look at the chemistry of the hydrogen molecule when it is placed at different sites of C-Be clusters like the 'on-top C site' and 'on-top Be site'. We look at the binding energies of hydrogen at different sites. In Section 6.3.2

we look a host of possible lithium based light metal hydrides and their thermodynamics are evaluated using their heats of formations. The crystal structure of a possible material with favorable thermodynamics is deduced and is proposed as a novel hydrogen storage material.

### 6.1 Introduction

It has been emphasized enough until now, the importance of studying clusters and their chemistry with hydrogen to evaluate their scope in the application for hydrogen storage. In this chapter, we study the behavior of the ground state C-Be clusters divulged in the previous chapter upon their interaction with hydrogen molecule. The hydrogen molecule is introduced at different positions like (i) 'on-top beryllium' with the hydrogen axis parallel to the plane of the cluster and (ii) 'on-top beryllium' with the hydrogen axis perpendicular to the plane of the cluster were examined and their binding energies on each of these positions is evaluated. There was also a third type of adsorption site 'on-top carbon' that we studied. We look into the isodensity surfaces of each of these clusters to see if there is any stronger physical bond formed by the hydrogen molecule with the C-Be cluster.

In the later part of this report, we study the lithium based C-Be metal hydrides. We focus on lithium based materials due to the advantage it has because of its low weight. It is well known that the gravimetric specifications are important DOE requirements for storage materials other than their thermodynamic requirement. That is the reason we keep to only light metal hydrides through out this project. We consider the heats of formation of these materials to look into thermodynamic stability. The chemical reaction between metal and hydrogen leads to the formation of a metal hydride. The energy released during this chemical reaction is called the formation enthalpy or the heat of formation ( $\Delta H_f$ ) of the metal hydride. The larger the heat of formation of a metal hydride, more stable it is, and higher is the temperature needed to desorp hydrogen from it. For a hydrogen storage material to be practically used, it must show promising thermodynamic properties and have sufficiently rapid kinetics of hydrogen charging and discharging. According to Alapati et al. [91] the  $\Delta H_f$  of a metal hydride should be between -30 and -60 kJ/Mol of  $H_2$ , for it to be useful as a hydrogen storage medium. A  $\Delta H$  less than -30 kJ/Mol will result in the hydride being not very easily reversible and a  $\Delta H$  greater than -60 kJ/Mol will lead to an extraordinary stability of the metal hydride,

which implies higher desorption temperatures. We have looked into the heats of formation of these novel carbon based metal hydrides.

## 6.2 Methodology

All the calculations reported here are conducted using DFT at the B3PW91/6-31+g\*\* theory level on  $C_nBe_{n-x}$   $n = 1$  to 11,  $x = 0$  to  $(n-1)$  using the G03 program [228]. Cluster equilibrium geometries, energies and Mulliken charge distribution are obtained for these clusters. Here, the clusters' behavior upon molecular hydrogen adsorption is explored. On each cluster, hydrogen molecule's behaviors on different cluster sites were studied. The electronic ground state energies of these structures are obtained and the  $H_2$  Binding Energy in these clusters is calculated along with their atomization energies. Isodensity surfaces were calculated using the visualization program gaussview. The binding energy of hydrogen molecule with each of these clusters is calculated using the equation below:

$$B.E. / H \text{ atom}((C_{n-x}Be_x) - H_2) = -\left(E_{[C_{n-x}Be_x]-H_2} - E_{[C_{n-x}Be_x]} - E_{H_2}\right) / 2.$$

Then the different carbon based lithium materials of the type  $LiC_nBe_yH_x$  where 'n' varies from 0 to 3 for every 'y' that varies from 1 to 3 are studied using the same theory level. Their heats of formation are calculated based on

their formation (or decomposition) reactions. The decomposition reaction for a metal hydride  $\text{LiC}_n\text{Be}_y\text{H}_x$  is taken as  $\text{LiH} + \text{C}_n\text{Be}_y + \text{H}_{x-1} \rightarrow \text{LiC}_n\text{Be}_y\text{H}_x$  as studied by Alapati et al. [91]. For each system, the normalized form of the above reaction is taken so as to obtain the heat of formation of 1 mol of  $\text{H}_2$ . The enthalpy of the above reaction is calculated as  $\Delta H = \sum_{\text{products}} E - \sum_{\text{reactants}} E$  where  $E$  is the total energy of each product/reactant as calculated using the same density functional B3PW91 and the basis set 6-31++G\*\*. The ground state geometry of each of these systems is also calculated at this level of theory.

Then Polymorph module of materials studio® [263] suite of programs from accelrys [263] is then used to define the crystal structure of the material that showed promise in our thermodynamic calculations. Polymorph uses a Monte Carlo simulated annealing algorithm to search the lattice energy hyper-surface for probable crystal packing alternatives and thus selects the ground state among possibly thousands of different possible structures.

### 6.3 Results and Discussion

#### 6.3.1 Interaction of Hydrogen Molecule with C-Be Clusters

The strongest adsorption of hydrogen molecule on these clusters in terms of the binding energy was observed 'on-top beryllium' with hydrogen molecule axis parallel to the plane of the CBe cluster. Instead of showing the all the clusters we studied, we show only one case which is symbolic of all the similar results. Figure 6.3-1 shows two cases when hydrogen is placed 'on-top beryllium' versus 'on-top carbon'. From this figure it is clearly seen that when hydrogen is nearer to beryllium there is only one isosurface which is indicative that there is a formation of physical bond between hydrogen molecule and  $C_3Be$  cluster. Whereas when hydrogen molecule is in the vicinity of carbon, there are two isosurfaces to show that there is no physical bond formation. This clearly shows that it is easier thermodynamically to desorb hydrogen from the vicinity of carbon than it is from the vicinity of beryllium. This result points to the hypothesis that, a metal hydride which consists of beryllium can be destabilized thermodynamically by introducing carbon in it as an impurity atom.

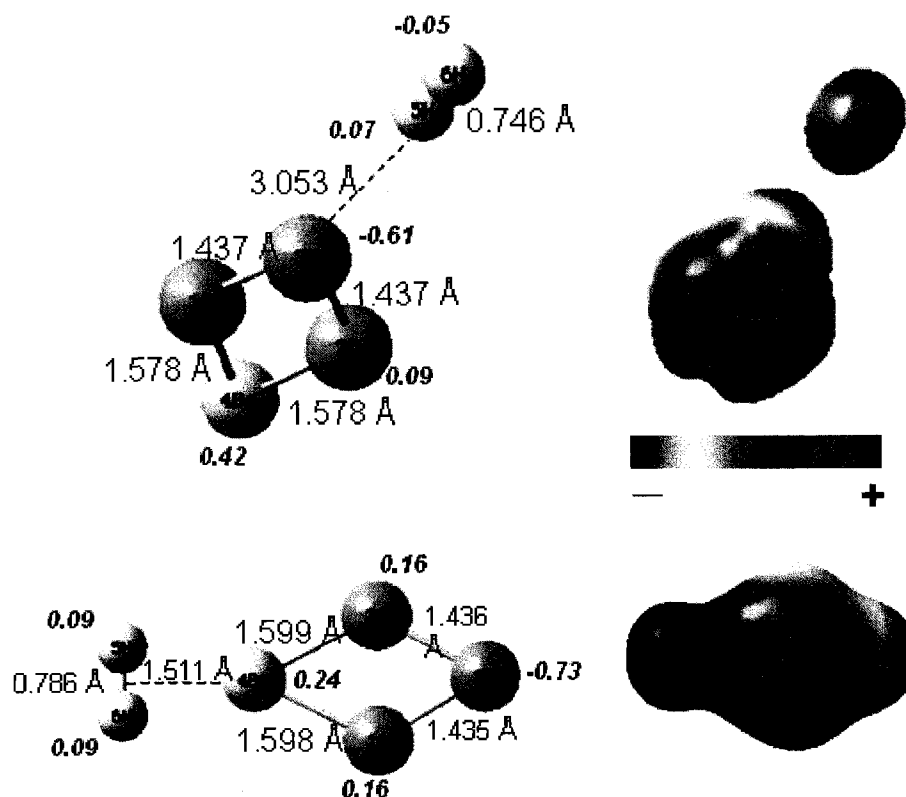


Figure 6.3-1 The behavior of hydrogen when it is placed on top of C (above) vs when it is placed on top of Be (below). Bond lengths are in Angstroms. Mulliken charge and Isodensity surfaces of each are also depicted.

### 6.3.2 Novel Li-C-Be Materials for Hydrogen Storage

After studying the C-Be + H<sub>2</sub> systems, we study the carbon-based lithium hydrides in search of the novel material for hydrogen storage. The procedure that is adopted here is to obtain the ground state configuration and the energetics of these systems with varying amounts of carbon and beryllium in them and their heats of formation calculated to get an understanding of the thermodynamics.

Figure 6.3-2 shows the ground states of some of the lithium-based materials studied.

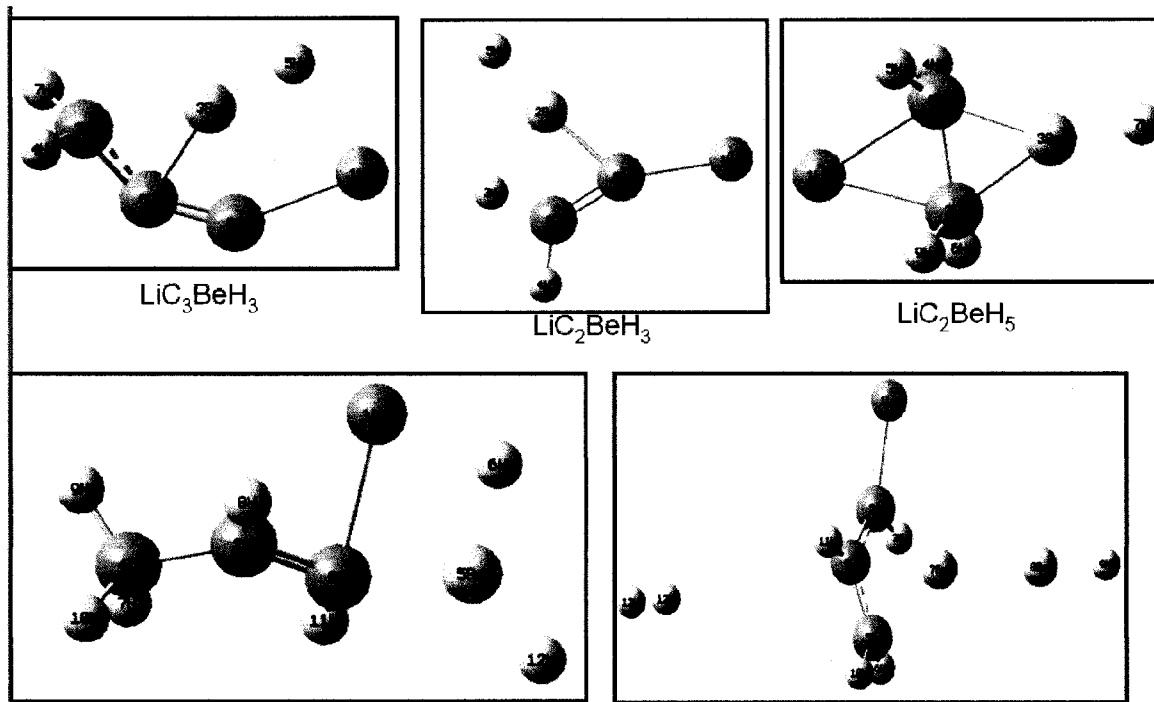


Figure 6.3-2 Ground states of some of the lithium based materials studied.

Once the ground state structures of all these structures is obtained, the heats of formation for different reaction schemes are calculated and are tabulated. The weight percentage of hydrogen in each of these metal hydrides is calculated according to the formula below:

Wt% of  $H_2$  in  $LiC_nBe_yH_x =$

$$\left[ \frac{x * (At.Wt)_H}{(At.Wt)_{Li} + n * (At.Wt)_C + y * (At.Wt)_{Be} + x * (At.Wt)_H} \right] * 100.$$



As mentioned earlier, a large number of metal hydrides of the type  $\text{LiC}_n\text{Be}_y\text{H}_x$  where 'n' varies from 0 to 3 for every 'y' that varies from 1 to 3 are studied. Their heats of formation are calculated based on their formation (or decomposition) reactions. Different reaction schemes were examined in the pursuit of the most favorable reaction scheme. The heats of formations are finally calculated using the equation

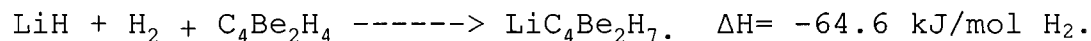
$$\Delta H = \sum_{\text{products}} E - \sum_{\text{reactants}} E,$$

according to the scheme  $\text{LiH} + \text{C}_n\text{Be}_y + \text{H}_{x-1} \rightarrow \text{LiC}_n\text{Be}_y\text{H}_x$ . Table 6.3-A lists some of the equations that we have studied.

Table 6.3-A Heats of formation of some of the reaction schemes examined.

System	Normalized Formation Reactions	$\Delta H_f$ (kJ/mol $\text{H}_2$ )	Wt % of Hydrogen
$\text{LiBeH}_3$	$\text{LiH} + \text{Be} + \text{H}_2 \rightarrow \text{LiBeH}_3$	-362	15.96
$\text{LiCBeH}_3$	$\text{LiH} + \text{CBe} + \text{H}_2 \rightarrow \text{LiCBeH}_3$	-1125	9.78
$\text{LiCBeH}_5$	$1/2\text{LiH} + 1/2\text{CBe} + \text{H}_2 \rightarrow 1/2\text{LiCBeH}_5$	-571	15.30
$\text{LiC}_2\text{BeH}_3$	$\text{LiH} + \text{C}_2\text{Be} + \text{H}_2 \rightarrow \text{LiC}_2\text{BeH}_3$	-478	7.05
$\text{LiC}_2\text{BeH}_5$	$1/2\text{LiH} + 1/2\text{C}_2\text{Be} + \text{H}_2 \rightarrow 1/2\text{LiC}_2\text{BeH}_5$	-311	11.22
$\text{LiC}_2\text{BeH}_7$	$1/3\text{LiH} + 1/3\text{C}_2\text{Be} + \text{H}_2 \rightarrow 1/3\text{LiC}_2\text{BeH}_7$	-215	12.61
$\text{LiC}_3\text{BeH}_3$	$\text{LiH} + \text{C}_3\text{Be} + \text{H}_2 \rightarrow \text{LiC}_3\text{BeH}_3$	-763	5.51
$\text{LiC}_3\text{BeH}_7$	$1/3\text{LiH} + 1/3\text{C}_3\text{Be} + \text{H}_2 \rightarrow 1/3\text{LiC}_3\text{BeH}_7$	-324	11.97
$\text{LiC}_3\text{BeH}_9$	$1/4\text{LiH} + 1/4\text{C}_3\text{Be} + \text{H}_2 \rightarrow 1/4\text{LiC}_3\text{BeH}_9$	-244	14.88

We studied more than 45 different reactions and have calculated the heats of reactions. In our search for the material with favorable thermodynamics, the following reaction shows some promise due to its heat of formation being within the acceptable range for metal hydrides.



On taking a closer look at the exact system involved in this reaction we find that it is,  $\text{LiC}_4\text{Be}_2\text{H}_5$ . Therefore, we have used the Monte Carlo simulated annealing program to come up with a crystal structure for it. Polymorph software uses the simulated annealing approach to search for a possible crystal structure among more than 14,000 different structures. This derived crystal structure is shown below in Figure 6.3-3. We find a monoclinic structure for this crystal with its lattice parameters as  $a=16.205 \text{ \AA}$ ,  $b=4.409 \text{ \AA}$ ,  $c= 9.188 \text{ \AA}$ ,  $\alpha= 90^\circ$ ,  $\beta=129.66^\circ$ ,  $\gamma=90^\circ$ .

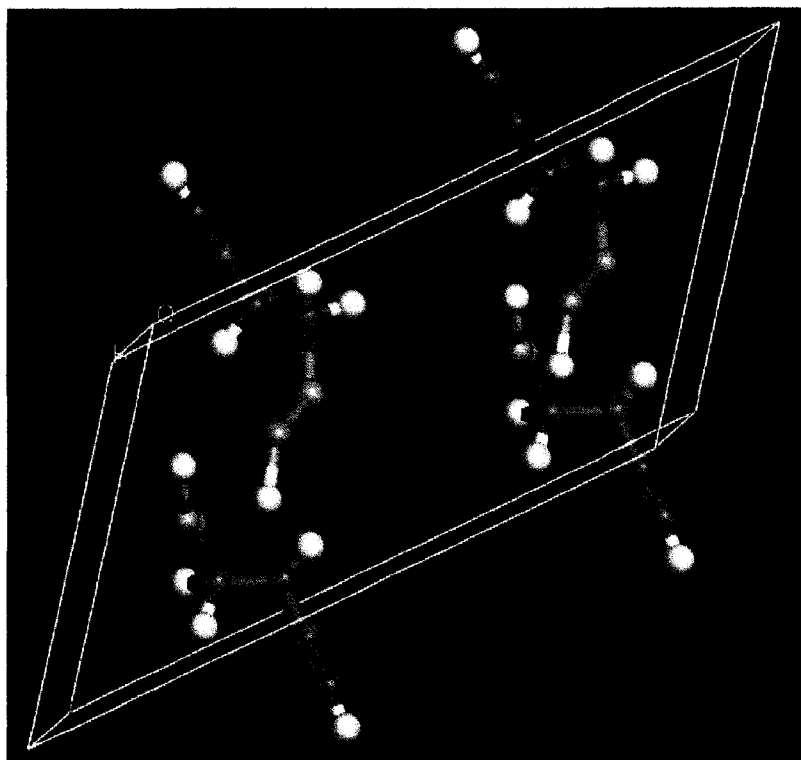


Figure 6.3-3 Crystal structure of  $\text{LiC}_4\text{Be}_2\text{H}_5$  structure.

Interestingly, the C-Be cluster unit present in this material, promising for hydrogen storage is the  $\text{C}_4\text{Be}_2$  which was found to be one among the 'magic clusters' when we looked into the C-Be clusters in Chapter 4.

#### 6.4 Conclusions

In Chapter 6, we looked into the interactions of hydrogen molecule with C-Be clusters. We have looked at the binding energies of hydrogen molecule with C-Be clusters at different sites. We see that hydrogen binds tightly to the vicinity of beryllium than to the vicinity of carbon.

Therefore it can be speculated that the carbon atoms present in the Be containing metal hydride, might be a cause for the easier extraction of hydrogen from it, or in other terms might be a good destabilizing agent.

The other conclusion we derive is that, our exhaustive study of more than 45 different reaction schemes leads to  $\text{LiC}_4\text{Be}_2\text{H}_5$  as a promising material for hydrogen storage.  $\text{C}_4\text{Be}_2$  unit observed inside this system is one among the C-Be 'magic clusters' we found while studying C-Be clusters. The lattice parameters of the crystal structure deduced for this system is  $a = 16.205 \text{ \AA}$ ,  $b = 4.409 \text{ \AA}$ ,  $c = 9.188 \text{ \AA}$ ,  $\alpha = 90^\circ$ ,  $\beta = 129.66^\circ$ ,  $\gamma = 90^\circ$ .

## CHAPTER 7

### DESTABILIZATION OF $\text{Li}_2\text{BEH}_4$ COMPLEX HYDRIDE BY CARBON DOPING

In Chapters 5 and 6 we studied the carbon-beryllium clusters, and looked into a novel class of lithium based C-Be hydrides depending upon their heats of formations respectively. In Chapters 7 and 8 we proceed with a more common approach of using carbon with metal hydrides. We use carbon as a dopant on the extended crystal systems and study the dehydrating thermodynamics of these modified systems.

#### 7.1 Introduction

The targets for storage materials set by DOE [14] puts forth basically two major types of handicaps in the proposed alternatives. One of them is that the material has to store at least 9 wt% of hydrogen and the other is that it should be able to release the stored hydrogen at the room temperature and pressure conditions (2015 US DOE targets). The former condition can in a way be addressed by using light metal hydrides as the choice of the storage

material which has high potential gravimetric storage capacities that outperform the DOE requirements [264]. However, their high dissociation temperatures associated with their slow hydriding/dehydriding kinetics act as a limiting factor in their practical application. Various destabilization techniques [91] for metal hydrides are proposed that reduce their dehydrogenation temperatures. Among them, introducing dopant species such as titanium [265] and other transition metals [266] is well researched. After Bogdanovic et al. [265] first reported the titanium doped alkali metal aluminum hydrides as potential novel reversible hydrogen storage materials in 1997, many [61,62,267-271] studies were performed on the doping of different transition metal in sodium and other alanates. Recently emphasis has shifted towards using graphite [272] as a dopant in light metal hydrides so as to reduce their dehydriding temperature and improve their kinetics. Graphite was also used as a co-dopant in Ti-doped sodium aluminum hydride by Wang et al. [117] to see its synergistic effects on their dehydrogenation and hydrogenation kinetics. They used the temperature programmed desorption curves to show that the dehydrogenation temperature decreased by as much as 15 °C for NaAlH<sub>4</sub> co-doped with 10 wt% graphite. Single-wall carbon nanotubes were also studied as catalysts for

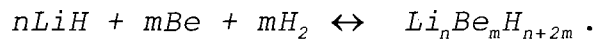
improving the hydrogen absorption and desorption properties of Ti/Zr-doped  $\text{NaAlH}_4$  by Dehouche et al. [118]. They reported that the sorption kinetics were enhanced by a factor of four for SWNT- $\text{NaAlH}_4$  and also the absorption and desorption kinetics of sodium alanate catalyzed by activated carbons and graphite showed improvement. Dal Toè et al. [116] used X-ray diffraction to study the  $\text{H}_2$  desorption/absorption kinetics of the magnesium hydride-graphite nanocomposites and reported that there is a clear improvement in the  $\text{MgH}_2$  ball-milled with graphite. Similar observations were made by Imamura et al. [110], much before all these later studies were performed.

Keeping in view the gravimetric prerequisites of the storage material, it can be asserted that graphite/carbon, rather than transition metals is a more adept dopant and that too in light metal hydrides. Among the class of complex metal hydrides [57], lithium-beryllium hydrides are the lightest reversible hydrides [260]. There have been several attempts [273,274] in the past aimed at solving the crystal structure of lithium beryllium hydride  $\text{Li}_2\text{BeH}_4$  which resulted in a rather poor quality X-ray diffraction data set. Theoretical calculations [275-277] performed based on these disputable data also resulted in superficial results to the extent that superconductivity was predicted for them

even at room temperatures [275]. More recently Bulychev et al. [278] synthesized the deuteride  $\text{Li}_2\text{BeD}_4$  by a high-pressure high-temperature technique and solved its crystal structure from X-Ray and neutron powder diffraction data. They established this crystal structure to belong to the space group  $\mathbf{P2}_1/c$  space group with the lattice parameters of  $a=7.06228 \text{ \AA}$ ,  $b= 8.3378 \text{ \AA}$ ,  $c=8.3465 \text{ \AA}$ ,  $\beta=93.577^\circ$ . Inside the  $\text{Li}_2\text{BeD}_4$  crystal lattice, they predicted the presence of isolated  $\text{BeD}_4$  tetrahedra and Li atoms situated in the interstitial spaces. They used the Electron Localization Function (ELF) distribution analysis to decipher the electronic bonding character in this crystal. They suggested a covalent Be-H bonding inside the  $[\text{BeH}_4]^{2-}$  anions and an ionic bond between  $\text{Li}^+--[\text{BeH}_4]^{2-}$  ions. They found no evidence of Li-H interactions. There was no theoretical calculation after this that could either establish or contradict these results. Prior to this study, lithium-beryllium hydrides and their hydrogen storage abilities were independently studied experimentally by Zaluska et al. [260]. These authors demonstrated the synthesis of lithium-beryllium hydrides by an approach employing mechanical alloying by ball milling. These authors also predicted that beryllium-hydrogen tetrahedra with covalent Be-H bond character are the main building blocks in these Be-based



hydrides. And they also commented that since lithium and beryllium are the lightest hydride forming metals, the reversible hydrogen capacity of these hydrides should exceed any other known hydride and reach almost 9 wt%. Their X-Ray diffraction results indicated that the hydrogenation/dehydrogenation in these hydrides proceeds according to the reversible reaction



Among the different n:m ratios that were examined, a ratio of 3:2 resulted in the maximum hydrogen capacity. Further thermodynamic study into these hydrides using Van't Hoff plot resulted in a value of -40 kJ/mol of H<sub>2</sub> for their enthalpy of formation ( $\Delta H$ ). It is very well known that for a metal hydride to be practically useful as a hydrogen storage material, its formation enthalpy ( $\Delta H$ ) should fall between the values of 30 kJ/mol and 60 kJ/mol [91]. This value of its  $\Delta H$  implies that the metal hydride could be used at temperatures as low as 150 °C. These hydrides also showed rather slow reaction kinetics which were emphasized by the authors to be in the need of improvement.

In Chapter 7 we attempt to address the question of high desorption temperature of lithium beryllium hydride Li<sub>2</sub>BeH<sub>4</sub>. We investigate the destabilization effect that carbon dopant has on Li<sub>2</sub>BeH<sub>4</sub> crystalline system. We perform

a detailed analysis of the local electronic structures in the presence of carbon impurity. In Section 7.3.1, we present the density functional theory optimized geometry of the metal hydride  $\text{Li}_2\text{BeH}_4$  and we compare it to the experimental results published earlier [260,278]. We present the total and the partial density of states plots for every species of atoms and complement them with the electron density maps of a unit cell to discuss the bonding nature in these hydrides. In Section 7.3.2, we present the results when a single carbon dopant atom is introduced in the  $2 \times 2 \times 1$  super cell of this metal hydride lattice. Different sites are explored for this dopant and energy cost involved in these processes is presented. In Section 7.3.3, dopant studies are further continued with the introduction of one more dopant atom in the lattice (two impurity atoms, in total). In Section 7.3.4, *ab initio* MD calculations on these metal hydrides, with and without the carbon dopant are discussed. We present the properties such as the bond populations at different time steps and compare these for systems with and without carbon impurity and discuss why the presence of impurity helps lower the desorption temperature.

## 7.2 Methodology

### 7.2.1 Theory Level

All the calculations presented in this chapter are performed using the plane wave pseudo potential implementation of Density Functional Theory (DFT) as applied in the program CASTEP<sup>®</sup>[279] module of the Materials Studio<sup>®</sup> suite from Accelrys [263]. Vanderbilt ultrasoft pseudopotentials [280] are used to represent the valence electrons. Generalized Gradient Approximation (GGA) within DFT as formulated by the Perdew and Wang (PW91) [136] correlation functional and the plane wave basis set is employed for all the calculations presented here.

### 7.2.2 Calculation Parameters

An energy cutoff of 1000 eV is used in these calculations of unit cells and an energy cutoff of 330 eV is used for super cell calculations. A convergence tolerance of  $1.0 \times 10^{-5}$  eV/atom is set with a k-point separation of  $0.04 \text{ \AA}^{-1}$  for all the calculations. Both the super cell and the unit cell calculations performed here are spin unpolarized. Cell optimization is done using the Broyden-Fletcher-Goldfarb-Shanno (BFGS) minimizer with fixed basis set quality.

### 7.2.3 Ab Initio MD parameters

In order to further study the local environment around the C dopant in the  $\text{Li}_2\text{BeH}_4$  crystal and also to investigate the time-evolution of this doped metal hydride crystal, *Ab-initio* Molecular Dynamics (DFT-MD) calculations as implemented in CASTEP<sup>®</sup> are performed at the temperatures of 373 K and 423 K on both the doped and pristine crystals. A time step of 1 femto second is employed for a total simulation time of 0.5 pico second. NPT ensemble (with a thermostat to maintain constant temperature and a barostat to maintain constant pressure) is used in all of these calculations.

### 7.2.4 Bond Nature

Electron density maps, in conjunction with the total (TDOS) and the partial density of states (PDOS) are used to analyze the bonding nature of these compounds. DOS calculations are based on Mulliken population analysis [281] which allows us to calculate the contribution from each energy band to a given atomic orbital. TDOS plots show the sum of all the contributions from the participating atomic species and the PDOS plots show the individual atomic contributions to the sum.

### 7.2.5 Bond Population Analysis

Bond population analysis are implemented in CASTEP<sup>®</sup> as described in the references by Segall et al. [282,283]. Due to the delocalized nature of the plane wave basis set states, a disadvantage of performing a plane wave calculation is that it provides no insight into the localization of the electrons in the system. Linear Combination of Atomic Orbitals (LCAO) basis sets, in contrast to these, provide a more natural way of specifying quantities such as atomic charges and bond populations. In CASTEP<sup>®</sup> population analysis is performed by applying the Mulliken formalism to the projected states obtained from the projection of the plane wave states onto a localized basis using a technique defined by Sanchez-Portal et al. [284]. This technique leads to the population analysis results comparable to those obtained by using localized LCAO basis sets. The bond population values reported on a scale from -1 to 1 represent an anti-bonding state for negative values and a bonding state for positive values with the bond strength and its degree of covalence proportional to the magnitude closer to 1. Even though the magnitude of these populations might not be of much physical significance, but the relative overlap population between two atoms in different compounds, under the

condition that a consistent basis set is used in their calculation, can yield useful information [282,283,285].

### **7.3 Results and Discussion**

#### **7.3.1 Crystal Structure of Pristine Li<sub>2</sub>BeH<sub>4</sub>**

As mentioned earlier, Bulychev et al. [278] used x-ray and neutron powder diffraction to experimentally resolve the crystal structure of lithium beryllium deuteride, Li<sub>2</sub>BeD<sub>4</sub>. Their **P2<sub>1</sub>/c** experimental crystal structure is initially used to construct the lithium beryllium hydride Li<sub>2</sub>BeH<sub>4</sub> unit cell. This crystal structure is further optimized using the density functional theory and the energy minimized conformation is obtained. The calculated and the reported experimental lattice parameters together with the structure of the optimized crystal and the important bond lengths in it are presented in Figure 7.3-1.

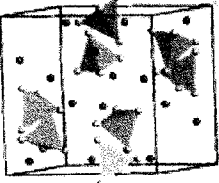
Li <sub>2</sub> BeH <sub>4</sub> Lattice structure	Li <sub>2</sub> BeH <sub>4</sub> Bond Lengths (Å)		Li <sub>2</sub> BeD <sub>4</sub> Bond Lengths (Å)		Li <sub>2</sub> BeH <sub>4</sub> Lattice Parameters	Li <sub>2</sub> BeD <sub>4</sub> Lattice Parameters
		Li-Be	2.680	Li-Be	2.61 - 2.85	a=6.970 Å
Be-H		1.450	Be-D	1.39 - 1.44	b=8.259 Å	b = 8.338 Å
Li-H		1.93 - 2.59	Li-D	1.83-2.27	c=8.368 Å	c = 8.346 Å
					$\alpha = \gamma = 90^\circ$	$\alpha = \gamma = 90^\circ$
					$\beta = 93.598^\circ$	$\beta = 93.577^\circ$

Figure 7.3-1 2x2x1 supercell of Li<sub>2</sub>BeH<sub>4</sub>, its calculated lattice parameters compared to the reported experimental parameters for Li<sub>2</sub>BeD<sub>4</sub> [278]. Purple atoms in the lattice structure are Li, solid green structures are BeH<sub>4</sub> tetrahedra with H atoms in white at the ends.

The calculated lattice parameters for Li<sub>2</sub>BeH<sub>4</sub>, a= 6.970 Å, b= 8.259 Å, c= 8.368 Å and  $\alpha=\gamma= 90^\circ$ ,  $\beta= 93.598^\circ$  are reasonable in comparison to the reported experimental lattice parameters of a= 7.062 Å, b= 8.338 Å, c= 8.346 Å, and  $\alpha=\gamma= 90^\circ$ ,  $\beta= 93.577^\circ$  reported for Li<sub>2</sub>BeD<sub>4</sub>. The calculated crystal structure of Li<sub>2</sub>BeH<sub>4</sub> contains the isolated BeH<sub>4</sub> tetrahedra (beryllium atom at the center, and each hydrogen atom at four different corners of the tetrahedra) and lithium atoms are contained in the interstitial spaces. All the BeH<sub>4</sub> tetrahedra are close to regular with the Be-H bond length in the range of 1.450 Å.

Total (TDOS) and partial (PDOS) density of states (Figure 7.3-2a) as well as the electron density maps (Figure 7.3-2b) are used to determine the nature of various

chemical bonds in this system. Since there is little contribution from the Li orbitals to the occupied states, it is likely that Li atom is ionized as a  $\text{Li}^+$  cation. The occupied states consist of s orbitals of beryllium and s orbitals of hydrogen and also form sharp peaks. This indicates that they are strongly localized around  $[\text{BeH}_4]$  complex. This localized electron distribution around the  $\text{BeH}_4$  complex can also be looked at from the electron density maps (Figure 7.3-2b). A detailed study on the bond orders using the Mülliken population analysis technique [281] is also performed. These studies reveal a Be-H bond population value ranging between 0.89-0.97, thus confirming the covalent Be-H bonding inside the  $[\text{BeH}_4]$  complex. The bonding between the Li atoms and the  $[\text{BeH}_4]$  complexes is established as ionic by looking at the effective charges on them which are balanced by  $(-1.91e)$  on  $[\text{BeH}_4]^{2-}$  and  $(+1.91e)$  on their two associated  $\text{Li}^{2+}$  cations.



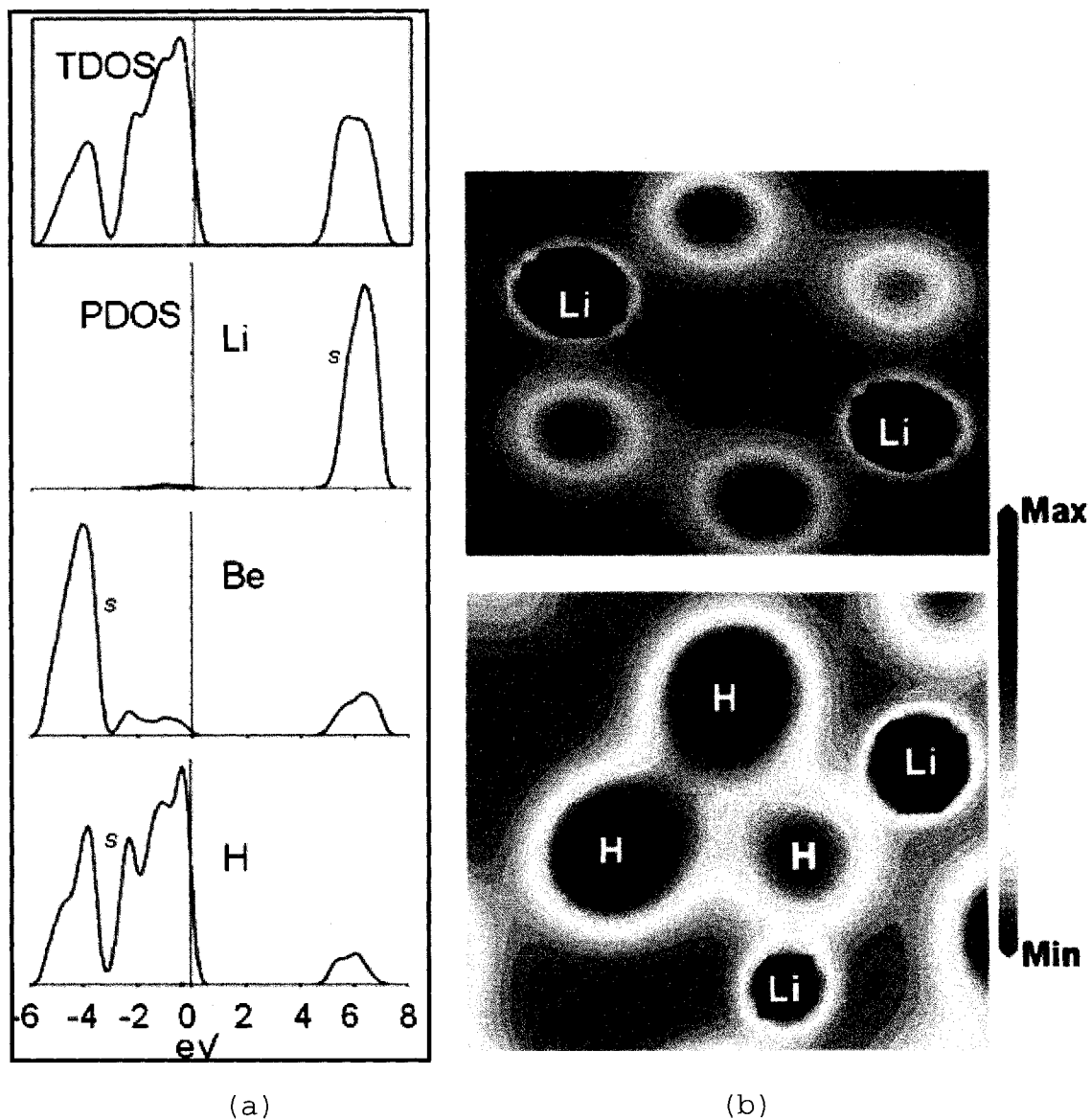


Figure 7.3-2 (a) Total and Partial DOS of  $\text{Li}_2\text{BeH}_4$  (b) Electron density maps of  $\text{Li}_2\text{BeH}_4$ .

### 7.3.2 Modified $\text{Li}_2\text{BeH}_4$ with a Single Carbon Dopant

After the unit cell of this lattice structure is calculated, a  $2 \times 2 \times 1$  super cell of this structure containing 56 atoms,  $8 * (\text{Li}_2\text{BeH}_4)$ , is constructed and optimized. The

(001) surface of this bulk structure is cleaved and a vacuum slab of around 10 Å is constructed on top of this. The purpose of this vacuum slab is to exclude the effects due to the periodic boundary conditions on the surface interactions at the top of this crystal structure. The effect of carbon as a dopant is studied by introducing it as an impurity on the different sites like the interstitial site and the native Li site of the crystal system. The energy required for dopant at different sites is calculated using the equations below.

Energy required for dopant at Native Li:

$$\left[ E(\text{Li}_{n-1}\text{CBe}_n\text{H}_{4n}) - E(\text{Li}_{n-1}\text{Be}_n\text{H}_{4n}) - E(\text{C}) \right] / N.$$

Energy required for dopant at interstitial site:

$$\left[ E(\text{Li}_n\text{CBe}_n\text{H}_{4n}) - E(\text{Li}_n\text{Be}_n\text{H}_{4n}) - E(\text{C}) \right] / N.$$

In the above equations,  $N$  is the total number of atoms. The energy cost required for introducing the carbon dopant as obtained from our calculations is -0.18 eV for native Li site and -0.15 eV for interstitial site. Since dopant introduction at interstitial site is energetically more favorable, further studies are continued with the dopant at interstitial site. Also the interstitial sites in the different layers of this metal hydride, for example, top, sub-surface and bulk layers are used for the

introduction of the carbon dopant. Substitution energies per atom for introducing a single dopant carbon atom in different layers are calculated using the above equation and are tabulated in Table 7.3-A.

Table 7.3-A Substitution energies in different layers of  $\text{Li}_2\text{BeH}_4$ .

Dopant Layer	Energy (eV)
Top	-0.15
Sub Surface	-0.15
Bulk	-0.16

In the presence of a carbon atom (Figure 7.3-3) in the top surface of this lattice, the two nearest neighboring tetrahedra to the carbon atom are seen to be distorted in such a way that the two Be-H bonds in each tetrahedra (previously in the range of 1.39 Å to 1.45 Å) are elongated in the range of 2.58 Å to 4.31 Å.

Similar kind of changes in the Be-H bonds in the  $[\text{Be-H}_4]$  tetrahedra which are nearest to the dopant atom are seen when the carbon dopant is placed in the other layers like the subsurface and the bulk of the lattice. The configurations which depict the changes in the crystal when the carbon atom is placed in the sub-surface and the bulk of the lattice are not shown here for brevity.

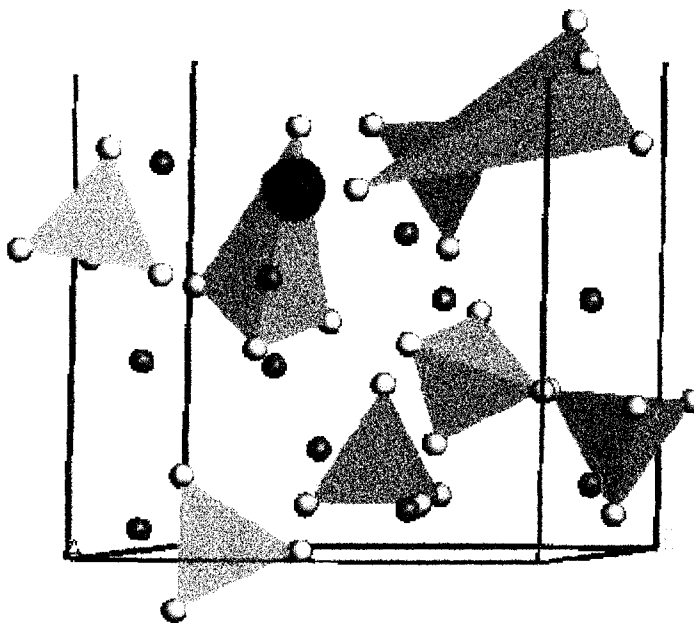


Figure 7.3-3  $\text{Li}_2\text{BeH}_4$  crystal structure when carbon atom is placed in the top surface of the crystal. Distorted tetrahedra near the bulky brown atom show the elongation in the Be-H bond.

Table 7.3-B lists the different bond lengths in the native lattice (without carbon) and compares them to the bond lengths when carbon is placed at different sites. It is also seen that when the carbon dopant is placed in the subsurface layer, both the Be-H bonds that are elongated are from the same  $\text{BeH}_4$  tetrahedra. Irrespective of whether they are from the same  $\text{BeH}_4$  unit or not (in case of other dopant layers), in each case, one carbon atom is seen to affect at least two nearest hydrogen atoms.

Table 7.3-B Different bond lengths when the carbon atom is in different layers in the  $8^*(\text{Li}_2\text{BeH}_4)$  supercell lattice.

Bonds	Native Super Cell (Å)	C in Surface (Å)	C in Subsurface (Å)	C in Bulk (Å)
Be - H (Nearest Neighbors)	1.425 - 1.45	2.58 - 4.31	2.4 - 2.81	2.44 - 2.52
Li - Be	2.68 - 2.78	2.41 - 2.42	2.6 - 2.8	2.28
Be - H	1.425 - 1.45	1.45 - 1.61	1.43 - 1.58	1.48 - 1.65

From Table 7.3-B it can be observed that the change in the Be-H bond lengths of the nearest neighboring  $[\text{BeH}_4]$  unit when carbon atom is in the subsurface and the bulk of the crystal lattice, is not as prominent as it is when the dopant (carbon) is in the surface layer. Nevertheless, there is a considerable difference of the order of 1.0-1.5 Å in the bond lengths, suggesting a considerable decrease in their bond strengths. Also, the Be-H bond lengths of the  $[\text{BeH}_4]$  tetrahedra other than the nearest neighbors show an increase in their lengths not as significant as the nearest neighbors.

On a closer look at the region of interest near the dopant atom in the trajectory file of these simulations (Figure 7.3-4), it can be seen that these Be-H bonds which are seen to be elongated by 1 to 3 Å are not only elongated

but these bonds are broken in the presence of carbon and a C-Be-H complex (Figure 7.3-4b) is seen to form.

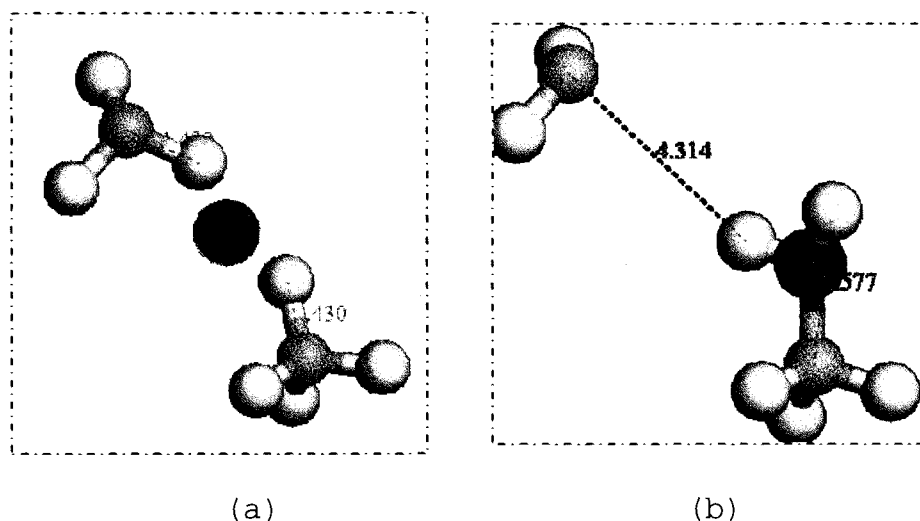


Figure 7.3-4 Region of interest in the crystal lattice of Figure 7.3-2 (a) before and (b) after the simulation.

In order to confirm the formation of any type of complexes and also to look further into the chemistry that is taking place in the lattice upon doping with carbon, we have performed the analysis on the electronic density of states. These total and partial density plots are shown in Figure 7.3-5. From this figure and comparing it to the DOS plots in Figure 7.3-2a which show density of states without any impurity, we see that there is an extra peak (denoted by peak I) in TDOS with carbon dopant. On the analysis of the contributions to this peak it is observed that it mainly comprises of p-orbitals of carbon and s-orbitals of

beryllium and hydrogen. Thus this analysis proves that there is indeed the formation of C-Be-H complexes in the local environment of the dopant atom.

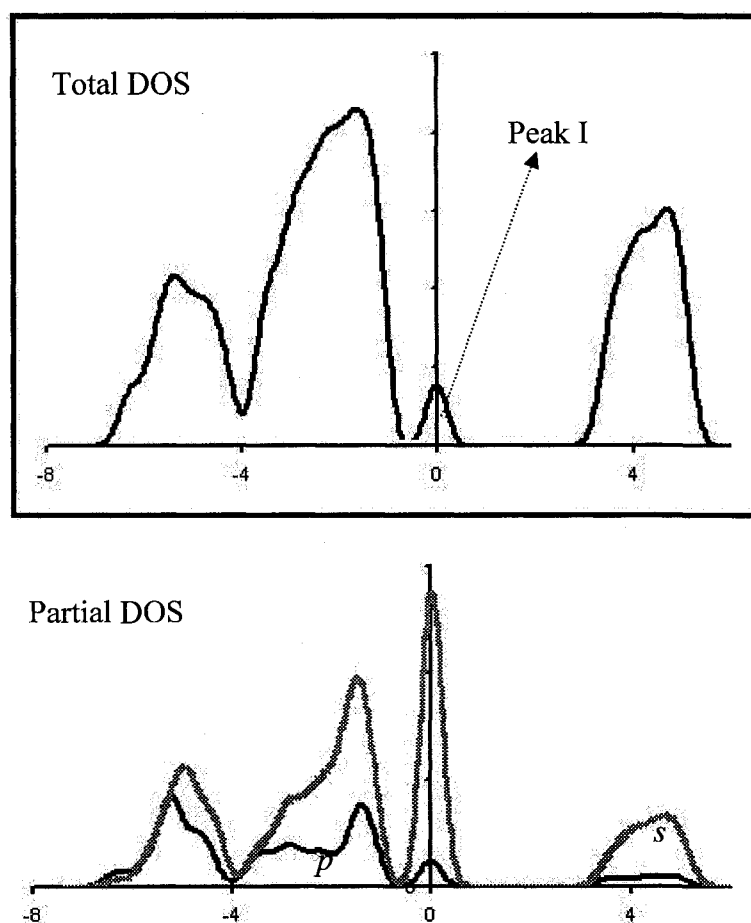


Figure 7.3-5 Total and partial DOS when carbon is doped in the top layer of  $\text{Li}_2\text{BeH}_4$  lattice.

Similar peaks are observed in the DOS plots of the subsurface and top doped lattices which are not shown here.

The strengths of different bonds are analyzed by calculating overlap population in the bonds in C-Be-H

compounds. The bond populations of various notable bonds with their bond lengths are given in Table 7.3-C. From this table it can be seen that the Be-C and C-H bond strengths of nearest neighbors to dopant have a comparatively strong physical bond which again points to the formation of the C-Be-H complex.

Table 7.3-C Overlap bond populations and bond lengths of important bonds in the presence of a carbon dopant.

Bond	Population	Length (Å)
H30-C1	0.92	1.11
H25-C1	0.91	1.12
Be8-C1	0.87	1.8
H22-Be6	0.74	1.47
H6-Be2	0.77	1.48

Another very interesting point to note in the presence of the carbon dopant is that bond strength of the Be-H bonds in the non neighboring Be-H complexes of the crystal (last two rows of Table 7.3-C) have considerably reduced even though their lengths appear to have remained constant. This decrease in the bond strength is highly indicative of the decrease in the temperature required for the release of hydrogen from this crystal in the presence of carbon impurity. The decrease in the Be-H bond strength of  $[\text{BeH}_4]^{2-}$  units causes a destabilization effect and this



will help in a reduction of the desorption temperature. A similar Al-H bond weakening was measured in computational studies by Íñiguez et al. [75] for the Ti doped NaAlH<sub>4</sub> system.

### 7.3.3 Li<sub>2</sub>BeH<sub>4</sub> with Two Carbon Dopant Atoms

To further investigate into the role of carbon impurity and also to see if the quantity of dopant introduced has any effect, we introduced two carbon dopant atoms simultaneously placed in the three different combinations of surface/subsurface, surface/bulk and subsurface/bulk of the Li<sub>2</sub>BeH<sub>4</sub> crystal Lattice. We computed the energy cost involved in the inducement of second impurity at different sites by using the equation

$$\frac{[E((Li_2BeH_4)_n C_2) - E((Li_2BeH_4)_n C) - E(C)]}{N},$$

where N is the total number of atoms. We find that this value is approximately the same for all the different sites studied and that is equal to 0.13 eV.

Figure 7.3-6 shows a scheme of the corresponding crystal lattices when the dopant is in these sites. It can be seen from this figure that each of the two dopant carbon atoms helps up to two hydrogen atoms in 'getting released' from the strongly bound [BeH<sub>4</sub>] units.

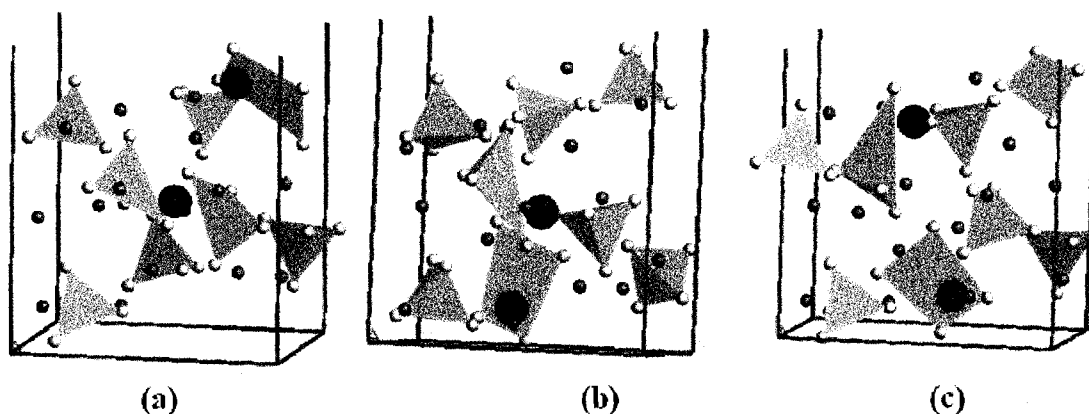


Figure 7.3-6 Carbon in the (a) surface/subsurface, (b) subsurface/bulk, and (c) surface/bulk in the  $\text{Li}_2\text{BeH}_4$  crystal Lattice. Distorted tetrahedra represent  $\text{BeH}_4$  units with elongated Be-H bonds.

#### 7.3.4 Ab Initio Molecular Dynamics

In order to further study the local environment around the C dopant in the  $\text{Li}_2\text{BeH}_4$  crystal and also to investigate the time-evolution of this doped metal hydride crystal, *ab initio* Molecular Dynamics (DFT-MD) calculation is performed at the temperatures of 373 K and 423 K on both the doped and pristine crystals. A time step of 1 femto second is employed for a total simulation time of 0.5 pico second. NPT ensemble is used in these calculations. There are two main conclusions obtained in these studies.

(a) The fact that C-Be-H compounds are observed even after a time of 0.5 ps confirms that these compounds are indeed formed and are stable.

(b) By calculating the DOS and the bond populations, at different time steps (0.125 ps, 0.25 ps, 0.375 ps and 0.5 ps) it is observed that there is a decrease in the non neighboring Be-H bond strengths which translates into a clear reduction of the stability and the resulting decrease in the desorption temperature of these modified metal hydrides. Also this study reveals that there is a reduction in the ionic interactions of  $\text{Li}^{2+}$  and  $[\text{BeH}_4]^{2-}$  which might also have a reducing effect on the stability of these compounds.

#### **7.4 Conclusions**

After studying the beryllium and C-Be clusters in considerable detail, and looking into a possible novel light metal hydride based on these complexes in the Chapters 4, 5 and 6 respectively, here we have looked into a more common approach to the use of carbon with metal hydrides. As has been discussed in Chapter 2 on related work in metal hydrides, carbon based materials such as graphite or carbon nanotubes have been used as a dopant with different metal hydrides to produce a 'destabilizing' effect on them and thereby reducing the desorption temperatures. Despite there being experimental work on the doping of graphite in metal hydrides like sodium alanate,

there are no first principles calculations on them that could aid in understanding the internal chemistry upon doping with C. Here, we have studied the carbon doping in the lightest complex metal hydride, which is lithium beryllium hydride,  $\text{Li}_2\text{BeH}_4$  in considerable detail.

After deciding the crystal structure of pristine  $\text{Li}_2\text{BeH}_4$  which is in considerable agreement with the experimental results, we have introduced the carbon impurities in different quantities. The energy cost for the impurity in interstitial is lesser than on native Li, and that is the reason why further calculations are performed with dopant in interstitial sites. Upon the introduction of carbon dopant, we see that in the vicinity of the dopant C-Be-H complexes are being formed. Each carbon atom influences upto two nearest hydrogen atoms. This effects into the weakening of non neighboring Be-H bonds, which results in the decrease of the desorption temperature. A further study of the bonding character performed also reveals that the reduction in the ionic interaction of  $\text{Li}^+$  ions with  $[\text{BeH}_4]^{2-}$ , together with the earlier mentioned factor may be the reasons behind the destabilization of the hydride and the reduction of desorption temperatures.

## CHAPTER 8

### DESTABILIZATION OF OTHER COMPLEX HYDRIDES BY CARBON DOPING AND THE THERMODYNAMICS OF DESTABILIZED REACTIONS

#### 8.1 Introduction

The main difference between general metal hydrides and the complex metal hydrides is that complex metal hydrides typically contain more than one type of metal or metalloid [286]. The bonding scheme in them is such that they exhibit ionic bonding between the positive metal ion and the negative molecular anion complex. These molecular anion complexes contain the hydrides with significant covalent bonding between the hydrogen atom at the corners of a tetrahedron and the second metal or metalloid atom. In general, complex metal hydrides have the formula  $M_xN_yH_n$ , where  $M$  is an alkali metal cation or cation complex and  $N$  is a metal or metalloid. These are light-weight storage materials that, typify a good compromise between hydrogen content, desorption temperature and reaction enthalpy [287]. The noted examples of complex metal hydrides are the

'Alanates,  $M-AlH_4$ ', the 'Borohydrides,  $M-BH_4$ ', the 'amides  $M-NH_2$ ' etc., classes of hydrides. The lithium beryllium hydrides  $Li_2BeH_4$  studied in Chapter 7 are also complex hydrides. In Chapter 8, the concept of carbon doping is extended to three more famous complex metal hydrides - two borohydrides (of lithium,  $LiBH_4$  and of sodium,  $NaBH_4$ ) and an alanate (of lithium,  $LiAlH_4$ ).

Complex metal hydrides were previously referred to as classical metal hydrides [288]. These are also known as 'one-pass' hydrogen storage systems which means that hydrogen evolves upon their contact with water [20]. The reason for a special interest in alanates and borates is their light weight and their large capacity of hydrogen atoms per metal atom [20]. Despite these appealing characteristics, the factors that keep them from their practical implementation are the thermodynamic stability and unfavorable kinetics.

As discussed in Section 7.1, alanates, especially sodium alanate,  $NaAlH_4$  is one of the most researched and documented materials for hydrogen storage. The facts that are in favor of sodium aluminum hydride are theoretical reversible hydrogen storage capacity of 5.6 wt%, low cost and its availability in bulk [20]. However, they are not considered as rechargeable hydrogen carriers due to their

irreversibility and poor kinetics. Bogdanovic and Schwickardi [289] demonstrated that upon doping with proper titanium compounds, the dehydriding of aluminum hydrides could be kinetically enhanced. This report triggered a lot [61,62,266,268-271] of work on this titanium modified alanates and related studies. Here we study lithium alanate modified with carbon doping. Lithium alanate's theoretical hydrogen capacity is 10.5 wt%. Unfortunately, it has an extremely high equilibrium pressure of hydrogen, even at room temperature [20]. In the past, there have been both experimental [69,290-294] and theoretical [91] studies on  $\text{LiAlH}_4$ . The detailed crystal structure of  $\text{LiAlH}_4$  is well known. It crystallizes in the monoclinic  $\alpha$ - $\text{LiAlH}_4$ -type structure with space group  $P2_1/c$  and four formula units per unit cell [291]. The desorption of  $\text{LiAlH}_4$  proceeds in two steps [20]:



Titanium doping, as in the case of other alanates is performed also in the case of lithium aluminum hydrides [292-295]. When  $\text{LiAlH}_4$  is ball milled with titanium compounds, part of the hydrogen is released already under the conditions of ball milling [55]. The reversible storage

up to 1.8 wt% has been reported for titanium catalyzed  $\text{LiAlH}_4$  [294].

The importance of boron and its compounds in the context of hydrogen storage systems is documented [296].  $\text{LiBH}_4$ , first synthesized by Schlesinger and Brown [297], has the highest gravimetric storage capacity among all the complex metal hydrides with a value of 18.4 wt% [55]. The temperature range for major decomposition of  $\text{LiBH}_4$  is 400-600 °C with the start being at 320 °C [55]. There have been different studies reported which suggest different additives to be used that reduce the desorption temperatures of  $\text{LiBH}_4$ . Züttel et al. use  $\text{SiO}_2$  powder as an additive in  $\text{LiBH}_4$  and report that it reduces the decomposition onset temperature and that 9 wt% of hydrogen is released below 400 °C [298,299]. Vajo et al. report that  $\text{LiBH}_4$  can reversibly store 8-10 wt% hydrogen at temperatures of 315-400°C by addition of  $\text{MgH}_2$  including 2-3 mol%  $\text{TiCl}_3$  [93]. Cho et al. [108] have used the CALPHAD thermodynamic analysis approach and report that the decomposition temperature of  $\text{LiBH}_4$  goes down from 400°C to 170°C upon reaction with  $\text{MgH}_2$ . In the same reference, they also report that another reaction with the same borohydride,  $\text{LiBH}_4+\text{Al}$  also shows a significant decrease in the decomposition temperature. However, their study shows that the decrease



in the decomposition temperature for  $\text{NaBH}_4+\text{Al}$  is not as significant as that for the previous reaction. Another interesting study of  $\text{LiBH}_4$  related compounds is performed recently by Wang et al. [300], where they study the effect of single wall carbon nanotubes on the reversible hydrogen storage properties of  $\text{LiBH}_4\text{-MgH}_2$  composite. They report that the mechanical milling of 10 wt% purified SWNTs additive with  $\text{LiBH}_4\text{-MgH}_2$  composite helps release 10 wt% hydrogen within 20 minutes at 450 °C. This dehydriding rate is reported[300] to be over twice faster than that of neat  $\text{LiBH}_4\text{-MgH}_2$  composite. Other than unfavorable desorption thermodynamics, other factors that hinder the use of  $\text{LiBH}_4$  are (i) despite attempts being made to synthesize it from its elements even up to elevated temperatures up to 650 °C and pressure of 150 bar  $\text{H}_2$ , they have failed till date [299] and (ii) it is an expensive compound [301]. The same considerations valid for  $\text{LiBH}_4$  are also applicable to  $\text{NaBH}_4$ . It was Aiello et al. [302] that showed  $\text{LiBH}_4$  and  $\text{NaBH}_4$  have the potential to store hydrogen. Millenium Cell has already commercialized  $\text{NaBH}_4$  in the Hydrogen on Demand™ process. Amendola et al. [303,304] and Aiello et al. [302] demonstrated the possibility of  $\text{NaBH}_4$  for a safe and portable hydrogen gas generator. In its unmodified form, the thermodynamic properties are definitely not favorable

for reversible storage with a heat of formation value of -123.9 kJ/mol at 298 K [55].

In Chapter 8 we extend the concept of carbon doping studied in the case of  $\text{Li}_2\text{BeH}_4$  in the previous chapter to an extended set of complex hydride materials from the classes of alanates and borates. In particular we study lithium and sodium borohydrides, lithium alanate. We show here that the doping of these complex hydrides has effects very similar to the ones described in Chapter 7 on lithium beryllium hydrides. We present here that carbon doping can be used as a destabilizing scheme for these complex hydrides and discuss what effect it has on the bond lengths and strengths of  $[\text{BH}_4]^-$  and  $[\text{AlH}_4]^-$  respectively. As in Chapter 7, we first use DFT to establish the crystal structures of pristine  $\text{LiBH}_4$ ,  $\text{NaBH}_4$  and  $\text{LiAlH}_4$  respectively starting from their experimental structures. The bonding nature of each metal hydride is discussed with the help of the total and partial density of states plots and the electron density maps. These are presented in Section 8.3.1. After this, one and two carbon atom dopants are studied in the super cells each of these hydrides in the respective Sections 8.3.2 and 8.3.3. The energy requirement in introducing the dopant at different sites and different layers is examined. In Section 8.3.4 we move forward from the chemistry of the

dopant inside the lattice and what effect it has in terms of electronic structure, to look into the exact thermodynamic effect that this dopant produces in the destabilized reactions. We plot the Van't Hoff plots for the destabilized reactions and deduce the  $\Delta H$  of these systems. This leads the way further into the establishment of desorption temperatures of each of these modified hydrides at equilibrium pressure which generally is accepted as 1 bar.

## **8.2 Methodology**

All the calculations presented in Chapter 8 are performed using the plane wave pseudopotential implementation of DFT as implemented in the CASTEP<sup>®</sup> [279] module of the Materials Studio<sup>®</sup> suite from Accelrys [263]. Vanderbilt ultrasoft pseudopotentials [280] are used to represent the valence electrons. Generalized Gradient Approximation (GGA) within DFT as formulated by the Perdew and Wang (PW91) [136] correlation functional and the plane wave basis set is employed for all the calculations presented here. A detailed description of the calculation methodology and its parameters are discussed in Chapter 7.

## 8.3 Results and Discussion

### 8.3.1 Pristine Crystal Structures

The published experimental information on each of the complex hydrides,  $\text{LiBH}_4$ ,  $\text{NaBH}_4$ , and  $\text{LiAlH}_4$  are used to construct their respective initial unit cells. These are further optimized using the DFT at the GGA functional PW91 level of theory using very strong convergence criterions. Thus the theoretical minimum energy conformation is obtained. The crystal structure and the involved bonding nature in its constituent atoms are deciphered using the total and partial density of states (TDOS and PDOS). Sections 8.3.1.1 through 8.3.1.4 describe the results of each complex hydride crystal.

#### 8.3.1.1 $\text{LiBH}_4$ structure

The experimental crystal structure parameters and the atomic positions for  $\alpha$ -phase of lithium borohydride are taken from the work by Soulie et al. [305]. These authors have used the synchrotron X-Ray powder diffraction to look into the lattice parameters of this structure. At room temperature, they established  $\text{LiBH}_4$  to be of orthorhombic symmetry with space group  $Pnma$  and the lattice parameters,  $a=7.17858(4)$  Å,  $b=4.43686(2)$  Å,  $c=6.80321(4)$  Å [305]. This data is used in the present work for the construction of

the initial structure. The ground state  $\text{LiBH}_4$  is then calculated using DFT. The calculated structural parameters and bond lengths are well in agreement with the values reported by Soulie et al. [305]. The calculated lattice parameters together with the experimental data (from ref [305]) and a picture of the unit cell are shown in the Figure 8.3-1.

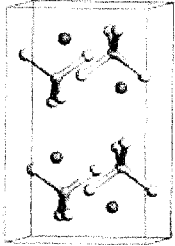
LiBH <sub>4</sub> Lattice Structure	Experimental LiBH <sub>4</sub> Bond Lengths <sup>a</sup> (Å)		Calculated LiBH <sub>4</sub> Bond Lengths (Å)		Experimental LiBH <sub>4</sub> Lattice Parameters <sup>a</sup> (Å)	Calculated LiBH <sub>4</sub> Lattice Parameters(Å)
		Li-B	2.446	Li-B	2.352	a = 7.1786
B-H		1.216-1.223	B-H	1.221-1.226	b = 4.4369	b = 4.3912
Li-H		2.104 - 2.47	Li-H	2.102 - 3.57	c = 6.8032	c = 6.6014
					$\alpha = \beta = \gamma = 90^\circ$	$\alpha = \beta = \gamma = 90^\circ$

Figure 8.3-1 Unit cell of  $\text{LiBH}_4$ , its calculated lattice parameters compared to the experimental parameters.

The total and the partial DOS and the electron density maps of  $\text{LiBH}_4$  are shown in Figures 8.3-2a and b respectively. These are used further to determine the bonding nature in this crystal system. From the DOS plots in Figure 8.3-2a, it can be seen that the valence band of  $\text{LiBH}_4$  is mainly contributed by the  $s$  orbitals of hydrogen and the  $s$  and  $p$  orbitals of boron. The electronic states with peaks containing the  $s$  orbitals of lithium are in the

conduction band. This suggests the existence of the electronic states strongly localized around  $[\text{BH}_4]^-$  anion complex and the  $\text{Li}^+$  cations being dispersed in the interstitial of the crystal. This fact is further established by the highly localized electron distribution around the  $[\text{BH}_4]^-$  complex, which can be looked at from the electron density maps (Figure 8.3-2b).

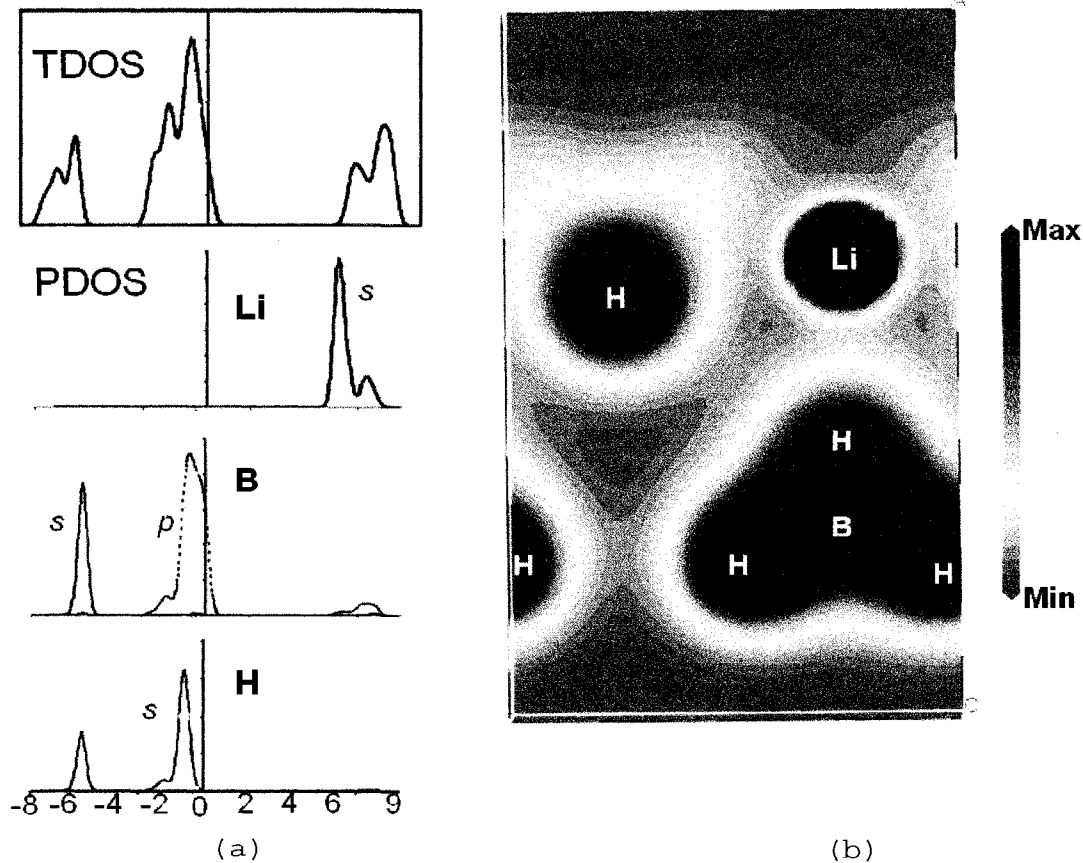


Figure 8.3-2 (a) Total/Partial DOS of  $\text{LiBH}_4$  (b) Electron density Maps for  $\text{LiBH}_4$ .

A detailed bond order study using the Mülliken population analysis technique [281] is also performed. These results show that a high bond population of around 1 is found between B-H bonds. This corroborates the fact that the B-H bonding in  $[\text{BH}_4]^-$  anion complex is covalent.

The bonding between the Li atoms and the  $[\text{BH}_4]$  complexes is established as ionic by looking at the effective charges on them which are balanced by  $(-1.04e)$  on  $[\text{BH}_4]^-$  and  $(+1.06e)$  on their associated  $\text{Li}^+$  cations.

#### **8.3.1.2 NaBH<sub>4</sub> structure**

The experimental data from the work by Fischer et al. [306] has been used for the initial building of the sodium borohydride crystal structure. With their neutron diffraction experiments, they resolved the crystal structures of both the lower and higher temperature structures of  $\text{NaBD}_4$ . The DFT calculated parameters are in good agreement with the reported results. They are both listed in Figure 8.3-3 together with the picture of the unit cell and the involved bond lengths.

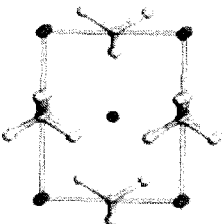
NaBH <sub>4</sub> Lattice Structure	Experimental NaBH <sub>4</sub> Bond Lengths (Å)		Calculated NaBH <sub>4</sub> Bond Lengths (Å)		Experimental NaBH <sub>4</sub> Lattice Parameters		Calculated NaBH <sub>4</sub> Lattice Parameters	
		Na-B	2.931	Na-B	2.944	a = 4.346	a = 4.358	
B-H		1.228	B-H	1.223	b = 4.346	b = 4.358		
Na-H		2.44-3.77	Na-H	2.38-3.78	c = 5.862	c = 5.888		
					$\alpha = \beta = \gamma = 90^\circ$	$\alpha = \beta = \gamma = 90^\circ$		

Figure 8.3-3 Unit cell of NaBH<sub>4</sub>, its calculated lattice parameters compared to the reported experimental parameters.

As in the previous case, the total and partial density of states, the electron density maps, Mülliken bond population analysis together with the effective charges are used to decipher the bonding nature between different types of atoms in the crystal. Due to the similarity in the results of this system with the previous twice mentioned results (once in the case of Li<sub>2</sub>BeH<sub>4</sub>, the other in the case of LiBH<sub>4</sub>), we do not repeat them again here to preserve the clarity and brevity. It is sufficient here to mention that we observe the ionic interactions between Na<sup>+</sup> ion and the [BH<sub>4</sub>]<sup>-</sup> ions with covalent interactions within the latter units.

### 8.3.1.3 LiAlH<sub>4</sub> structure

The experimental data from the work by Fischer et al.[306] have been used for the initial building of the sodium borohydride crystal structure. With their neutron



diffraction experiments, they resolved the crystal structures of both the lower and higher temperature structures of  $\text{NaBD}_4$ . The DFT calculated parameters are very well in agreement with the reported results. They are both listed in Figure 8.3-4 together with the picture of the unit cell and the involved bond lengths.

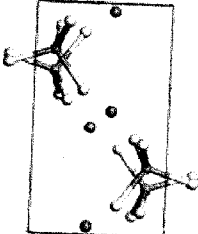
LiAlH <sub>4</sub> Lattice Structure	Experimental LiAlH <sub>4</sub> Bond Lengths (Å)		Calculated LiAlH <sub>4</sub> Bond Lengths (Å)		Experimental LiAlH <sub>4</sub> Lattice Parameters (Å)		Calculated LiAlH <sub>4</sub> Lattice Parameters (Å)	
		Li-Al	3.20	Li-Al	3.25	a = 4.817	a = 4.834	
Al-H		1.60 - 1.65	Al-H	1.62 - 1.64	b = 7.802	b = 7.834		
Li-H		1.94	Li-H	1.86 - 1.99	c = 7.821	c = 7.808		
					$\alpha = \gamma = 90^\circ, \beta = 112.23^\circ$	$\alpha = \gamma = 90^\circ, \beta = 111.66^\circ$		

Figure 8.3-4 Unit cell of  $\text{LiAlH}_4$ , its calculated lattice parameters compared to the reported experimental parameters.

### 8.3.2 Modified Hydrides with a Single Carbon Dopant

After the unit cell of this lattice structure is calculated, a  $2 \times 2 \times 1$  super cell of this structure containing 48 atoms,  $\text{Li}_8\text{B}_8\text{H}_{32}$ , is constructed and optimized. The (001) surface of this bulk structure is cleaved and a vacuum slab of around 10 Å is constructed on top of this. The purpose of this vacuum slab is to exclude the effects due to the periodic boundary conditions on the surface interactions at

the top of this crystal structure. The effect of carbon as a dopant is studied by introducing it as an impurity in different sites like the interstitial site and the native Li site of the crystal system. The energy required for dopant at different sites is calculated using the equations below.

Energy required for dopant at native Li

$$\frac{[E (Li_{n-1}CB_nH_{4n}) - E (Li_{n-1}B_nH_{4n}) - E(C)]}{N}$$

Energy required for dopant at interstitial site

$$\frac{[E (Li_nCB_nH_{4n}) - E (Li_nB_nH_{4n}) - E(C)]}{N}$$

In the above equations, N is the total number of atoms. The energy cost required for introducing the carbon dopant in the Native Li site and also introducing dopant in interstitial site as obtained from our calculations is - 0.20 eV each.

Since dopant introduction at both the interstitial site and native site is equally probable, further studies are continued with only the dopant at interstitial site. Also the interstitial sites in the different layers of this metal hydride, for example, top, subsurface and bulk layers are used for the introduction of the carbon dopant. Substitution energies per atom for introducing a single

dopant carbon atom in different layers are calculated using the equation below and are tabulated in Table 8.3-A.

$$\frac{[E (\text{LiBH}_4)_n \text{C} - E (\text{LiBH}_4)_n - E(\text{C})]}{N}$$

It can be seen from Table 8.3-A that the dopant introduction is almost equally likely, in terms of energy, in the interstitial sites of all three layers. DFT optimization of this metal hydride crystal with the presence of a carbon atom (Figure 8.3-5) in the top layer of this lattice reveals that the two nearest neighboring  $\text{BH}_4$  tetrahedra to the carbon impurity atom are distorted in such a way that the two B-H bonds in each tetrahedra (previously in the range of 1.21 Å to 1.45 Å) are elongated to the range of 1.24 Å to 2.21 Å.

Table 8.3-A Substitution energy required in different layers of  $\text{LiBH}_4$ .

Dopant Layer	Energy (eV)
Top	-0.20
Sub Surface	-0.19
Bulk	-0.19

Similar kinds of elongations in the Be-H bond lengths are observed when the dopant is in subsurface or the bulk layer. Table 8.3-B lists the different bond lengths in the

doped and undoped crystal. This elongation of the nearest neighbor Be-H bonds due to the presence of carbon suggests a decrease in these bond strengths, thereby reducing the desorbing temperatures.

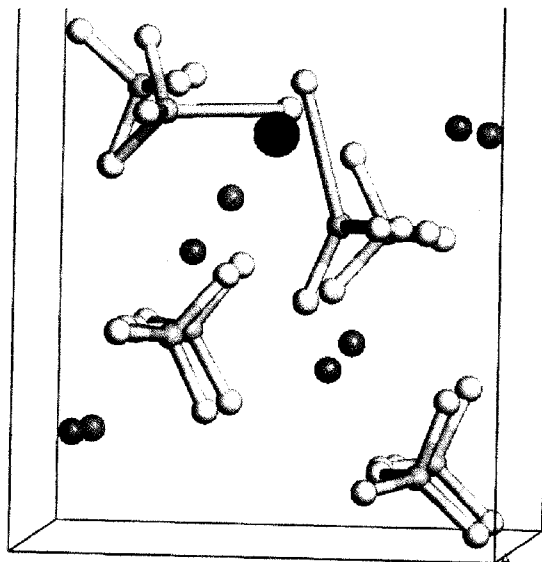


Figure 8.3-5  $\text{LiBH}_4$  crystal structure when carbon atom is placed in the top surface of the crystal. Purple atoms are Li, solid green structures are  $\text{BH}_4$  tetrahedra with H atoms in white at the ends, carbon atom is the bulky brown atom. Elongated B-H bonds are highlighted.

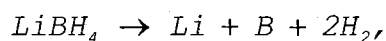
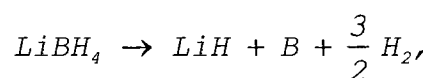
Table 8.3-B Different bond lengths when the carbon atom is in different sites in the  $(\text{LiBH}_4)_*8$  lattice.

Bonds	Native Super Cell (Å)	C on Surface (Å)	C in Subsurface (Å)	C in Bulk (Å)
B - H (Nearest Neighbors)	1.21-1.23	1.21-2.24	1.22-2.25	1.25-2.20
Li - B	2.10-2.15	2.05-2.28	2.12-2.23	2.28
B - H	1.21-1.23	1.21-1.24	1.21-1.23	1.21-1.23

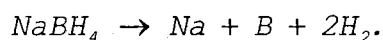
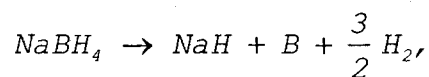
Similar types of elongations are observed when carbon is doped in  $\text{NaBH}_4$  and  $\text{LiAlH}_4$ . They are not shown here in order to avoid redundancy.

### 8.3.3 Thermodynamics of Destabilized Reactions

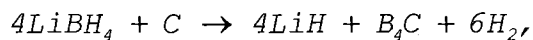
The general decomposition reactions proposed in the literature for the systems  $\text{LiBH}_4$  and  $\text{NaBH}_4$  are following.



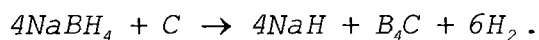
and



The systems  $\text{LiBH}_4$  and  $\text{NaBH}_4$  can decompose according to any of the reactions above. In light of the information obtained so far, the following destabilized reactions are proposed for  $\text{LiBH}_4$  and  $\text{NaBH}_4$  respectively.



and



For these destabilized reactions and also for the decomposition reactions already mentioned, Van't Hoff plots have been calculated to study the thermodynamics of these systems. For the compounds which were not calculated using

the DFT methods, thermodynamic data from the JANAF tables [307] was used. These are shown in the Figures 8.3-6 (for  $\text{LiBH}_4$ ) and 8.3-7 (for  $\text{NaBH}_4$ ) below:

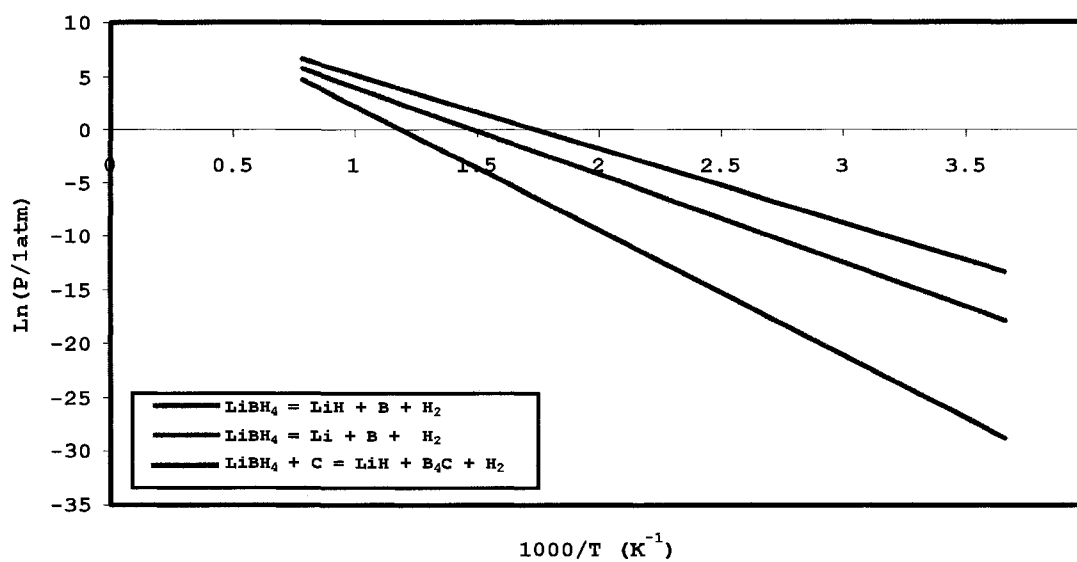


Figure 8.3-6 Van't Hoff Plots for destabilized  $\text{LiBH}_4$  system.

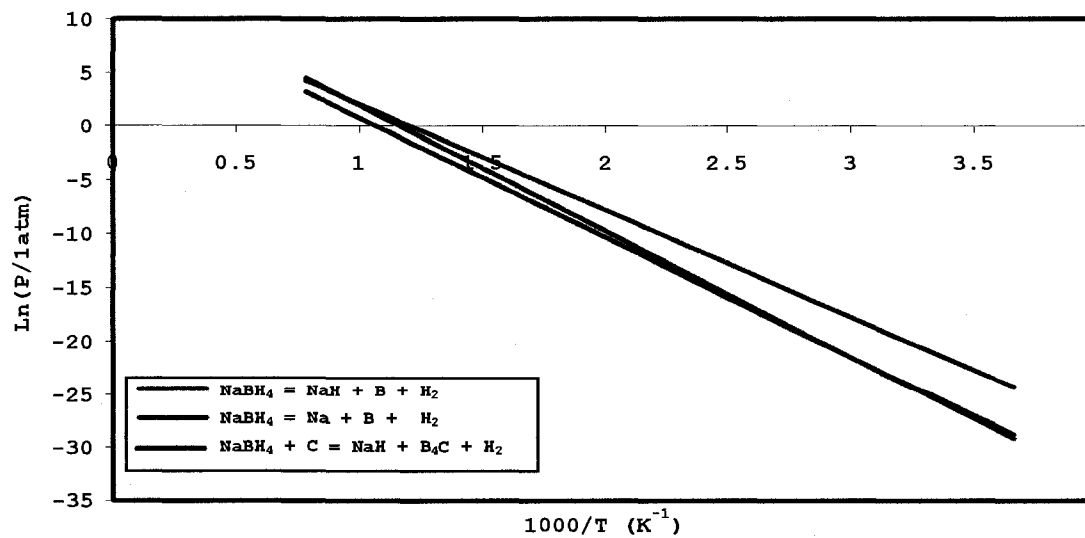


Figure 8.3-7 Van't Hoff Plots for destabilized  $\text{NaBH}_4$  system.

From these Van't Hoff plots we deduce the desorption temperatures required in each case, that is with and without the dopant and list them in the tables 8.3-C (for  $\text{LiBH}_4$ ) and 8.3-D ( $\text{NaBH}_4$ ) below.

Table 8.3-C  $\Delta H$  values and the desorption temperatures at equilibrium pressure of 1 bar for  $\text{LiBH}_4$ , with and without carbon dopant.

Reaction	$\Delta H$ (kJ/mol $\text{H}_2$ )	$T_{\text{calc}}$ (1 bar) ( $^{\circ}\text{C}$ )
$\text{LiBH}_4 = \text{Li} + \text{B} + 2\text{H}_2$	96.96	567
$\text{LiBH}_4 = \text{LiH} + \text{B} + 3/2\text{H}_2$	68.21	400
$4\text{LiBH}_4 + \text{C} = 4\text{LiH} + \text{B}_4\text{C} + 6\text{H}_2$	57.83	300

Table 8.3-D  $\Delta H$  values and the desorption temperatures at equilibrium pressure of 1 bar for  $\text{NaBH}_4$ , with and without carbon dopant.

Reaction	$\Delta H$ (kJ/mol $\text{H}_2$ )	$T_{\text{calc}}$ (1 bar) ( $^{\circ}\text{C}$ )
$\text{NaBH}_4 = \text{Na} + \text{B} + 2\text{H}_2$	97.52	585
$\text{NaBH}_4 = \text{NaH} + \text{B} + 3/2\text{H}_2$	92.76	654
$4\text{NaBH}_4 + \text{C} = 4\text{NaH} + \text{B}_4\text{C} + 6\text{H}_2$	82.39	554

As we can see from the desorption temperatures of both the destabilized  $\text{LiBH}_4$  and  $\text{NaBH}_4$ , we see that there is marked decrease in the carbon-destabilized  $\text{LiBH}_4$  of almost 100  $^{\circ}\text{C}$ . The decomposition of pure  $\text{LiBH}_4$  takes place at around 400  $^{\circ}\text{C}$ , where as the presence of C improves it to 300  $^{\circ}\text{C}$ . Anyway, the difference in the case of  $\text{NaBH}_4$  is not

so pronounced. We still observe a reduction of around 100 °C in the desorption temperature for  $\text{NaBH}_4$ , but the difference is not sufficient enough to be able to make the use of this hydride possible in the room temperature. This is not so surprising in the case of  $\text{NaBH}_4$ , due to its very well known stability [308].

#### **8.4 Conclusions**

In this chapter we have extended the type of calculations performed on lithium beryllium hydrides in Chapter 7 to three more complex hydrides namely lithium borohydride, sodium borohydride and lithium aluminum hydride. In all these cases we observe similar kind of results when they are doped with carbon. There is an elongation in the B-H or Al-H bond lengths respectively of both the neighboring and the non-neighboring units of dopant atom. We have constructed the Van't Hoff plots for the cases of the destabilized reactions of  $\text{LiBH}_4$  and  $\text{NaBH}_4$  and we observe that, in each case there is a decrease of a maximum of 100°C in the desorption temperatures of both the cases. One observatory point that needs to be clarified here is that, in our calculations of Van't Hoff plots we have not taken into consideration the vibrational corrections to the entropy.



In any case, it is well known that, the desorption temperatures values obtained without taking vibrational corrections are not very much inaccurate compared to the values with the corrections.

## CHAPTER 9

### CONCLUSIONS AND FUTURE WORK

#### 9.1 Conclusions

In this dissertation *ab initio* computational modeling techniques are used to test the viability of employing carbon doped light metal hydrides as a suitable storage method for hydrogen gas onboard transportation vehicles. The calculations suggest that carbon, which is a comparatively light weight material, is a good option as a dopant which can thermodynamically destabilize hydrides so as to reduce the decomposition temperatures.

The present study is initially started with the study of clusters due to the importance of the understanding of clusters needed to design novel materials for hydrogen storage. The geometrical and electronic properties of pure beryllium clusters have been studied by using a B3PW91 density functional. With the aid of analysis of electronic properties like the second-order difference in the energies, the HOMO-LUMO gaps and also the vertical ionization potentials, it is seen that  $Be_n$  with  $n=4$  and 10

exhibit extra stability. This is established also by the closed electronic shell theory. The  $\text{Be}_n\text{C}_m$  type clusters' studies are then performed in an exhaustive way. All the electronic as well as structural properties of these systems are reported. Thus the role of carbon in the stability of pure Be clusters is looked into. The 'magic clusters' of  $\text{Be}_n\text{C}_m$  type are deduced. The interactions of hydrogen molecule with these C-Be ground state clusters are then studied. The binding energies of these clusters to hydrogen are calculated and it is observed that hydrogen is bound stronger to the vicinity of beryllium than to the vicinity of carbon when it is in the C-Be system. This leads to the hypothesis that carbon can be doped into metal hydrides that have beryllium in it so as to reduce the desorption temperatures of these hydrides.

A lot of different reaction schemes are then looked into and their heats of reactions measured. With these studies, it is established that  $\text{LiC}_4\text{Be}_2\text{H}_5$  might be a novel material which can have a reasonable release temperature with a decent amount of hydrogen in it.

The extended system calculations are performed on the doping of carbon in the crystal systems of  $\text{Li}_2\text{BeH}_4$ ,  $\text{LiBH}_4$ ,  $\text{NaBH}_4$ , and  $\text{LiAlH}_4$ . The results imply that there is a clear destabilizing effect due to the carbon doping in all these

complex hydrides. *Ab Initio* MD calculations are also performed to see what types of complexes are formed. An investigation into the chemistry of the destabilizing effect suggest that the cause for this is not just the weakening of the Be-H or B-H bonds after doping, but also the decrease in the ionic interactions between Li-B or Li-Be. Van't Hoff plots of the destabilized reactions show the reduction of desorption temperature at least by 100°C in the case of LiBH<sub>4</sub> and NaBH<sub>4</sub>.

## 9.2 Future Work

One issue that needs to be addressed is the vibrational corrections to the zero point energies so that they are incorporated in the correct manner in the construction of Van't Hoff plots. In any case, it is known that these will not change the final result of the desorption temperature significantly.

Even though these systems were destabilized, they still do not seem to reach to a point where hydrogen is released from them at room temperatures. This issue needs to be examined further. Carbon as a destabilizing agent could perhaps be used with some other dopant so as to further reduce the temperatures down to room temperature.

The present study performs a detailed analysis of the thermodynamics of these destabilized systems, but it still needs to be determined if they exhibit favorable kinetics. It will be good to see if the hydrogen can be released from these systems fast enough.

The novel material  $\text{LiC}_4\text{Be}_2\text{H}_5$  that we looked into theoretically, and for which, developed the crystal structure needs to be synthesized experimentally to see if it is practically feasible.

## REFERENCES

1. Momirlan, M.; Veziroglu, T. N., The properties of hydrogen as fuel tomorrow in sustainable energy system for a cleaner planet. *International Journal of Hydrogen Energy* **2005**, 30, 795-802.
2. Momirlan, M.; Veziroglu, T. N., Current status of hydrogen energy. *Renewable and Sustainable Energy Reviews* **2002**, 6, 141-179.
3. Johnston, B.; Mayo, M. C.; Khare, A., Hydrogen: the energy source for the 21st century. *Technovation* **2005**, 25, 569-585.
4. Hoffman, P., *Tomorrow's energy: Hydrogen, Fuel Cells and the prospects for a Cleaner Planet*. Paperback ed.; The MIT Press: Cambridge, 2002.
5. Penner, S. S., Steps toward the hydrogen economy. *Energy* **2006**, 31, 33-43.
6. Marban, G.; Valdes-Solis, T., Towards the hydrogen economy? *International Journal of Hydrogen Energy* **2007**, 32, 1625-1637.
7. Zumerchik, J., *Macmillan Encyclopedia of Energy*. Macmillan Reference USA: New York, 2000.
8. Lovins, A. B. *Twenty Hydrogen Myths*; Rocky Mountain Institute: 20 June 2003, 2003.
9. Blanchette, S., A hydrogen economy and its impact on the world as we know it. *Energy Policy* **2008**, 36, 522-530.
10. Lide, D. R., *CRC Handbook of Chemistry and Physics*. 88th (Internet Version) ed.; CRC Press/ Taylor and Francis: Boca Raton, FL, 2008.

11. <http://home.att.net/~cat6a/fuels-VII.htm>. (April 30th, 2008),
12. Pinkerton, F. E.; Wicke, B. G., Bottling the Hydrogen Genie. *The Industrial Physicist* **2004**, 10, (1), 20-24.
13. Hoogers, G., *Fuel Cell Technology Handbook*. CRC Press: Boca Raton, Fl, 2006.
14. *Basic research needs for the hydrogen economy, Report of the basic energy sciences workshop on hydrogen production, storage, and use*, <http://www.sc.doe.gov/bes/hydrogen.pdf>; May 13-15, 2003.
15. Ritter, J. A.; Ebner, A. D.; Wang, J.; Zidan, R., Implementing a hydrogen economy. *Materials Today* **2003**, 6, (9), 18-23.
16. Zuttel, A., Hydrogen storage methods. *Naturwissenschaften* **2004**, 91, 157-172.
17. Ross, D. K., Hydrogen storage: The major technological barrier to the development of hydrogen fuel cell cars. *Vacuum* **2006**, 80, 1084-1089.
18. Sherif, S. A.; Barbir, F.; Veziroglu, T. N., Towards a Hydrogen Economy. *The Electricity Journal* **2005**, 18, (6), 62-76.
19. Tzimas, E.; Filiou, C.; Peteves, S. D.; Veyret, J.-B. *Hydrogen Storage: State-of-the-art and future perspective*; Institute for Energy, European Commission, Joint Research Center: Petten, The Netherlands, 2003.
20. Sakintuna, B.; Lamari-Darkrim, F.; Hirsher, M., Metal hydride materials for solid hydrogen storage: A review. *International Journal of Hydrogen Energy* **2007**, 32, 1121-1140.
21. Rosi, N. L.; Eckert, J.; Eddaoudi, M.; Vodak, D. T.; Kim, J.; O'Keeffe, M.; Yaghi, O. M., Hydrogen storage in microporous metal-organic frameworks. *Science* **2003**, 300, 1127-1129.

22. Strobel, R.; Garcke, J.; Moseley, P. T.; Jorissen, L.; Wolf, G., Hydrogen storage by carbon materials. *Journal of Power sources* **2006**, 159, 781-801.
23. Kroto, H. W.; Heath, J. R.; O'Brien, S. C.; Curl, R. F.; Smalley, R. E., C60: Buckminsterfullerene. *Nature* **1985**, 318, 162-163.
24. Iijima, S., Helical microtubules of graphitic carbon. *Nature* **1991**, 354, 56-58.
25. Burchell, T. D., *Carbon Materials for Advanced Technologies*. Elsevier Science Ltd.: 1999.
26. Osawa, E., *Perspectives of Fullerene Nanotechnology*. Kluwer Academic Publishers: 2002.
27. Dillon, A. C.; Heben, M. J., Hydrogen storage using carbon adsorbents: past, present and future. *Applied Physics A* **2001**, 172, (2), 133-142.
28. Dillon, A. C.; Jones, K. M.; Bekkedahl, T. A.; Kiang, C. H.; Bethune, D. S.; Heben, M. J., Storage of hydrogen in single-walled carbon nanotubes. *Nature* **1997**, 386, 377-379.
29. Chambers, A.; Park, C.; Baker, R. T. K.; Rodriguez, N. M., Hydrogen storage in graphite nanofibers. *Journal of Physical Chemistry B* **1998**, 102, (22), 4253-4256.
30. Sankaran, M.; Viswanathan, B., Hydrogen storage in boron substituted carbon nanotubes. *Carbon* **2007**, 45, 1628-1635.
31. Sankaran, M.; Viswanathan, B.; Murthy, S. S., Boron substituted carbon nanotubes- How appropriate are they for hydrogen storage? *International Journal of Hydrogen Energy* **2008**, 33, 393-403.
32. Sankaran, M.; Viswanathan, B., The role of heteroatoms in carbon nanotubes for hydrogen storage. *Carbon* **2006**, 44, (13), 2816-2821.



33. David, E., An overview of advanced materials for hydrogen storage. *Journal of Materials Processing Technology* **2005**, 162-163, 169-177.
34. Buchner, H.; Povel, R., The daimler-benz hydride vehicle project. *International Journal of Hydrogen Energy* **1982**, 7, (3), 259-266.
35. Liang, G.; Huot, J.; Boily, S.; Neste, A. V.; Schulz, R., Catalytic effect of transition metals on hydrogen sorption in nanocrystalline ball milled  $MgH_2$ -Tm (Tm=Ti, V, Mn, Fe and Ni) systems. *Journal of Alloys and Compounds* **1999**, 292, (1-2), 247-252.
36. Sagara, T.; Klassen, J.; Ganz, E., Computational study of hydrogen binding by metal-organic framework-5. *Journal of Chemical Physics* **2004**, 121, (24), 12543-12547.
37. Rowsell, J. L. C.; Eckert, J.; Yaghi, O. M., Characterization of  $H_2$  binding sites in prototypical metal-organic frameworks by inelastic neutron scattering. *Journal of American Chemical Society* **2005**, 127, (42), 14904-14910.
38. Buda, C.; Dunietz, B. D., Hydrogen physisorption on the organic linker in metal organic frameworks: *Ab initio* computational study. *Journal of Physical Chemistry B* **2006**, 110, 10479-10484.
39. Yang, Q.; Zhong, C., Understanding hydrogen adsorption in metal - organic frameworks with open metal sites: A computational study. *The Journal of Physical Chemistry B* **2006**, 110, 655-658.
40. Wicks, G. G.; Hueng, L. K.; Schumacher, R. F., Microspheres and microworlds. *American Ceramics Society Bulletin* 87, (6), 23-28.
41. Shelby, J.; Hall, M. Glass microspheres for hydrogen storage.  
[http://www.hydrogen.energy.gov/pdfs/review05/stp\\_47\\_hall.pdf](http://www.hydrogen.energy.gov/pdfs/review05/stp_47_hall.pdf)  
(December, 04, 2008.),

42. Kiran, B.; Jena, P.; Li, X.; Grubisic, A.; Stokes, S. T.; Ganteför, G. F.; Bowen, K. H.; Burgert, R.; Schnöckel, H., Magic rule for  $Al_nH_m$  magic clusters. *Physical Review Letters* **2007**, 98, 266802-1 - 266802-4.
43. deHeer, W. A., The physics of simple metal clusters: experimental aspects and simple models. *Reviews of Modern Physics* **1993**, 65, (3), 611-676.
44. Watari, N.; Ohnishi, S.; Ishii, Y., Hydrogen storage in Pd clusters. *Journal of Physics: Condensed Matter* **2000**, 12, (30), 6799-6823.
45. Williamson, A. J.; Reboledo, F. A. Nanostructured materials for hydrogen storage (Patent No. 7303736 ) The Regents of the University of California. 2007.
46. Wagemans, R. W. P. Magnesium for hydrogen storage : from micrometer to nanometer. Universiteit Utrecht, Utrecht, 2006.
47. Broom, D. P.; Kemali, M.; Ross, D. K., Magnetic properties of commercial metal hydride battery materials *Journal of Alloys and Compounds* **1999**, 293-295, 255-259.
48. Joubert, J.-M.; Cerný, R.; Latroche, M.; Leroy, E.; Guénee, L.; Percheron-Guégan, A.; Yvon, K., A structural study of the homogeneity domain of  $LaNi_5$ . *Journal of Solid State Chemistry* **2002**, 166, (1), 1-6.
49. Joubert, J.-M.; Černý, R.; Latroche, M.; Percheron-Guégan, A.; Schmitt, B., Hydrogenation of  $LaNi_5$  studied by in situ synchrotron powder diffraction. *Acta Materialia* **2006**, 54, (3), 713-719.
50. Joubert, J.-M.; Latroche, M.; Cerný, R.; Bowman Jr., R. C.; Percheron-Guégan, A.; Yvon, K., Crystallographic study of  $LaNi_{5-x}Sn_x$  ( $0.2 \leq x \leq 0.5$ ) compounds and their hydrides. *Journal of Alloys and Compounds* **1999**, 293-295, 124-129.
51. Joubert, J.-M.; Latroche, M.; Cerný, R.; Percheron-Guégan, A.; Yvon, K., Hydrogen cycling induced degradation in  $LaNi_5$ -type materials. *Journal of Alloys and Compounds* **2002**, 330-332, 208-214.

52. Yvon, K., Complex transition-metal hydrides. *Chimia* **1998**, 52, 613-619.
53. Schlapbach, L.; Züttel, A., Hydrogen-storage materials for mobile applications. *Nature* **2001**, 414, (6861), 353-358.
54. Bogdanovic', B.; Sandrock, G., Catalyzed complex metal hydrides. *Materials Research Society Bulletin* **2002**, 27, 712.
55. Schüth, F.; Bogdanovic, B.; Felderhoff, M., Light metal hydrides and complex hydrides for hydrogen storage. *Chemical Communications* **2004**, 2249-2258.
56. Cento, C.; Gilson, P.; Bilgili, M.; Masci, A.; Zheng, Q.; Prosini, P. P., How carbon affects hydrogen desorption in NaAlH<sub>4</sub> and Ti-doped NaAlH<sub>4</sub>. *Journal of Alloys and Compounds* **2007**, 437, (1-2), 360-366.
57. Slattery, D. K.; Hampton, M. D. In *Complex Hydrides for Hydrogen Storage*, U. S. DOE Hydrogen Program Review, 2002; 2002.
58. Bogdanovic', B.; Schwickardi, M., Ti-doped alkali metal aluminium hydrides as potential novel reversible hydrogen storage materials. *Journal of Alloys and Compounds* **1997**, 253-254, 1-9.
59. Bogdanovic', B.; Schwickardi, M., Ti-doped NaAlH<sub>4</sub> as a hydrogen storage - preparation by Ti-catalyzed hydrogenation of aluminum powder in conjunction with sodium hydride. *Applied Physics A* **2001**, 72, 221-223.
60. Bogdanovic', B.; Brand, R. A.; Marjanovic', A.; Schwickardi, M.; Tölle, J., Metal-doped sodium aluminium hydrides as potential new hydrogen storage materials. *Journal of Alloys and Compounds* **2000**, 302, (1-2), 36-58.
61. Sandrock, G.; Gross, K.; Thomas, G., Effect of Ti-catalyst content on the reversible hydrogen storage properties of the sodium alanates. *Journal of Alloys and Compounds* **2002**, 339, (1-2), 299-308.

62. Sun, D.; Kiyobayashi, T.; Takeshita, H. T.; Kuriyama, N.; Jensen, C. M., X-ray diffraction studies of titanium and zirconium doped NaAlH<sub>4</sub>: elucidation of doping induced structural changes and their relationship to enhanced hydrogen storage properties. *Journal of Alloys and Compounds* **2002**, 337, (1-2), L8-L11.
63. Gross, K. J.; Guthrie, S.; Takara, S.; Thomas, G., In-situ X-ray diffraction study of the decomposition of NaAlH<sub>4</sub>. *Journal of Alloys and Compounds* **2000**, 297, (1-2), 270-281.
64. Colbe, J. M. B. v.; Bogdanovic, B.; Felderhoff, M.; Pommerin, A.; Schüth, F., Recording of hydrogen evolution—a way for controlling the doping process of sodium alanate by ball milling. *Journal of Alloys and Compounds* **2004**, 370, (1-2), 104-109.
65. Bruster, E. L.; Dobbins, T. A.; Tittsworth, R.; Anton, D. In *X-ray Absorption Spectroscopy of Ti doped NaAlH<sub>4</sub> at the Titanium K-edge*, Materials Research Society Symposium - Proceedings, 2005; 2005.
66. Dobbins, T. A.; Bruster, E. L.; Oteri, E. U.; Ilavsky, J., Ultrasmall-angle X-ray scattering (USAXS) studies of morphological trends in high energy milled NaAlH<sub>4</sub> powders. *Journal of Alloys and Compounds* **2007**, 446-447, 248-254.
67. Dobbins, T. A.; Tittsworth, R.; Speakman, S.; Schneibel, J. In *Synchrotron X-ray Absorption Spectroscopy (XAS) for Understanding Dopant Effects in Ti-doped NaAlH<sub>4</sub>*, Advanced Materials for Energy Conversion, 2006; Chandra, D.; Petrovic, J. J.; Bautista, R.; Imam, A., Eds. TMS Publishers: 2006; pp 263-270.
68. Haber, J. A.; Crane, J. L.; Buhro, W. E.; Frey, C. A.; Sastry, S. M. L.; Balbach, J. J.; Conradi, M. S., Chemical synthesis of nanocrystalline titanium and nickel aluminides from the metal chlorides and lithium aluminum hydride. *Advanced Materials* **1996**, 8, (2), 163-166.
69. Balema, V. P.; Wiench, J. W.; Dennis, K. W.; Pruski, M.; Pecharsky, V. K., Titanium catalyzed solid-state transformations in LiAlH<sub>4</sub> during high-energy ball-milling. *Journal of Alloys and Compounds* **2001**, 329, (1-2), 108-114.

70. Majzoub, E. H.; Gross, K. J., Titanium-halide catalyst-precursors in sodium aluminum hydrides. *Journal of Alloys and Compounds* **2003**, 356-357, 363-367.
71. Gross, K. J.; Majzoub, E. H.; Spangler, S. W., The effects of titanium precursors on hydriding properties of alanates. *Journal of Alloys and Compounds* **2003**, 356-357, 423-428.
72. Dathara, G. K. P.; Mainardi, D. S., Structure and dynamics of Ti-Al-H compounds in Ti-doped NaAlH<sub>4</sub> *Molecular Simulation* **2008**, 34, (2), 201-210.
73. Løvvik, O. M.; Opalka, S. M., Density functional calculations of Ti-enhanced NaAlH<sub>4</sub> *Physical Review B* **2005**, 71, 054103-1 - 054103-10.
74. Vegge, T., Equilibrium structure and Ti-catalyzed H<sub>2</sub> desorption in NaAlH<sub>4</sub> nanoparticles from density functional theory. *Physical Chemistry Chemical Physics* **2006**, 8, 4853 - 4861.
75. Íñiguez, J.; Yildirim, T.; Udovic, T. J.; Sulic, M.; Jensen, C. M., Structure and hydrogen dynamics of pure and Ti-doped sodium alanate. *Physical Review B* **2004**, 70, 060101-060105.
76. Chen, P.; Xiong, Z.; Luo, J.; Lin, J.; Tan, K. L., Interaction of hydrogen with metal nitrides and imides. *Nature* **2002**, 420, (6913), 302-304.
77. Chen, P.; Xiong, Z.; Luo, J.; Lin, J.; Tan, K. L., Interaction between Lithium amide and Lithium hydride. *Journal of Physical Chemistry B* **2003**, 107, (39), 10967-10970.
78. Hu, Y. H.; Ruckenstein, E., H<sub>2</sub> storage in Li<sub>3</sub>N. Temperature-programmed hydrogenation and dehydrogenation. *Industrial & Engineering Chemistry Research* **2003**, 42, (21), 5135-5139.
79. Ichikawa, T.; Isobe, S.; Hanada, N.; Fujii, H., Lithium nitride for reversible hydrogen storage. *Journal of Alloys and Compounds* **2004**, 365, (1-2), 271-276.

80. Nakamori, Y.; Orimo, S.-i., Destabilization of Li-based complex hydrides. *Journal of Alloys and Compounds* **2004**, 370, (1-2), 271-275.
81. Nakamori, Y.; Kitahara, G.; Orimo, S., Synthesis and dehydriding studies of Mg-N-H systems. *Journal of Power Sources* **2004**, 138, (1-2), 309-312.
82. Ichikawa, T.; Hanada, N.; Isobe, S.; Leng, H.; Fujii, H., Mechanism of novel reaction from  $\text{LiNH}_2$  and  $\text{LiH}$  to  $\text{Li}_2\text{NH}$  and  $\text{H}_2$  as a promising hydrogen storage system. *Journal of Physical Chemistry B* **2004**, 108, (23), 7887-7892.
83. Luo, W.,  $(\text{LiNH}_2\text{-MgH}_2)$ : a viable hydrogen storage system. *Journal of Alloys and Compounds* **2004**, 381, (1-2), 284-287.
84. Leng, H. Y.; Ichikawa, T.; Hino, S.; Hanada, N.; Isobe, S.; Fujii, H., New metal-N-H system composed of  $\text{Mg}(\text{NH}_2)_2$  and  $\text{LiH}$  for hydrogen storage. *Journal of Physical Chemistry B* **2004**, 108, (26), 8763-8765.
85. Xiong, Z.; Wu, G.; Hu, J.; Chen, P., Ternary imides for hydrogen storage. *Advanced Materials* **2004**, 16, (17), 1522-1525.
86. Zhang, C.; Alavi, A., A First-Principles Investigation of  $\text{LiNH}_2$  as a Hydrogen-Storage Material: Effects of Substitutions of K and Mg for Li. *Journal of Physical Chemistry B* **2006**, 110, 7139-7143.
87. Orimo, S.; Nakamori, Y.; Kitahara, G.; Miwa, K.; Ohba, N.; Noritake, T.; Towata, S., Destabilization and enhanced dehydriding reaction of  $\text{LiNH}_2$ : an electronic structure viewpoint *Applied Physics A* **2004**, 79, (7), 1765-1767.
88. Nakamori, Y.; Orimo, S., Li-N based hydrogen storage materials. *Materials Science and Engineering B* **2004**, 108, (1-2), 48-50.
89. Reilly, J. J.; Wiswall, R. H., Reaction of hydrogen with alloys of magnesium and copper. *Inorganic Chemistry* **1967**, 6, (12), 2220-2223.

90. Reilly, J. J.; Wiswall, R. H., Reaction of hydrogen with alloys of magnesium and nickel and the formation of  $Mg_2NiH_4$ . *Inorganic Chemistry* **1968**, 7, (11), 2254-2256.
91. Alapati, S. V.; Johnson, J. K.; Sholl, D. S., Identification of Destabilized Metal Hydrides for Hydrogen Storage Using First Principles Calculations. *Journal of Physical Chemistry B* **2006**, 110, 8769-8776.
92. Vajo, J. J.; Mertens, F.; Ahn, C. C.; Robert C. Bowman, J.; Fultz, B., Altering hydrogen storage properties by hydride destabilization through alloy formation: LiH and  $MgH_2$  destabilized with Si. *Journal of Physical Chemistry B* **2004**, 108, (37), 13977-13983.
93. Vajo, J. J.; Skeith, S. L.; Mertens, F., Reversible Storage of Hydrogen in Destabilized  $LiBH_4$ . *Journal of Physical Chemistry B* **2005**, 109, (9), 3719-3722.
94. Pinkerton, F. E.; Meisner, G. P.; Meyer, M. S.; Balogh, M. P.; Kundrat, M. D., Hydrogen desorption exceeding ten weight percent from the new quaternary hydride  $Li_3BN_2H_8$ . *Journal of Physical Chemistry B* **2005**, 109, (1), 6-8.
95. Aoki, M.; Miwa, K.; Noritake, T.; Kitahara, G.; Nakamori, Y.; Orimo, S.; Towata, S., Destabilization of  $LiBH_4$  by mixing with  $LiNH_2$ . *Applied Physics A* **2005**, 80, (7), 1409-1412.
96. Noritake, T.; Aoki, M.; Towata, S.; Ninomiya, A.; Nakamori, Y.; Orimo, S., Crystal structure analysis of novel complex hydrides formed by the combination of  $LiBH_4$  and  $LiNH_2$ . *Applied Physics A* **2006**, 83, (2), 277-279.
97. Ichikawa, T.; Hanada, N.; Isobe, S.; Leng, H.; Fujii, H., Composite Materials based on Light Elements for Hydrogen Storage. *Materials Transactions* **2005**, 46, (01), 1-14.
98. Nakamori, Y.; Kitahara, G.; Ninomiya, A.; Aoki, M.; Noritake, T.; Towata, S.-i.; Orimo, S.-i., Guidelines for developing amide-based hydrogen storage materials. *Materials Transactions* **2005**, 46, (09), 2093-2097.

99. Luo, W.; Sickafoose, S., Thermodynamic and structural characterization of the Mg-Li-N-H hydrogen storage system. *Journal of Alloys and Compounds* **2006**, 407, (1-2), 274-281.
100. Vajo, J. J.; Olson, G. L., Hydrogen Storage in destabilized chemical systems. *Scripta Materialia* **2007**, 56, 829-834.
101. Vajo, J. J.; Salguero, T. T.; Gross, A. F.; Skeith, S. L.; Olson, G. L., Thermodynamic destabilization and reaction kinetics in light metal hydride systems. *Journal of Alloys and Compounds* **2007**, 446-447, 409-414.
102. Yang, J.; Sudik, A.; Siegel, D. J.; Halliday, D.; Drews, A.; III, R. O. C.; Wolverton, C.; Lewis, G. J.; Sachtler, J. W. A.; Low, J. J.; Faheem, S. A.; Lesch, D. A.; Ozolins, V., Hydrogen storage properties of  $2\text{LiNH}_2 + \text{LiBH}_4 + \text{MgH}_2$ . *Journal of Alloys and Compounds* **2007**, 446-447, 345-349.
103. Barison, S.; Agresti, F.; Russo, S. L.; Maddalena, A.; Palade, P.; Principi, G.; Torzod, G., A study of the  $\text{LiNH}_2\text{-MgH}_2$  system for solid state hydrogen storage *Journal of Alloys and Compounds* **2008**, 459, (1-2), 343-347.
104. Lim, J.-H.; Shim, J.-H.; Lee, Y.-S.; Cho, Y. W.; Lee, J., Dehydrogenation behavior of  $\text{LiBH}_4/\text{CaH}_2$  composite with  $\text{NbF}_5$ . *Scripta Materialia* **2008**, 59, (12), 1251-1254.
105. Pinkerton, F. E.; Meyer, M. S., Reversible hydrogen storage in the lithium borohydride-calcium hydride coupled system. *Journal of Alloys and Compounds* **2008**, 464, (1-2), L1-L4.
106. Alapati, S. V.; Johnson, J. K.; Sholl, D. S., Predicting Reaction Equilibria for Destabilized Metal Hydride Decomposition Reactions for Reversible Hydrogen Storage *Journal of Physical Chemistry B* **2007**, 111, (4), 1584-1591.
107. Velikokhatnyi, O. I.; Kumta, P. N., Energetics of the lithium-magnesium imide-magnesium amide and lithium hydride reaction for hydrogen storage: An ab initio study *Materials Science and Engineering B* **2007**, 140, (1-2), 114-122.



108. Cho, Y. W.; Shim, J.-H.; Lee, B.-J., Thermal destabilization of binary and complex metal hydrides by chemical reaction: A thermodynamic analysis. *Computer Coupling of Phase Diagrams and Thermochemistry* **2006**, 30, 65-69.
109. Imamura, H.; Sakasai, N., Hydriding characteristics of Mg-based composites prepared using a ball mill. *Journal of Alloys and Compounds* **1995**, 231, (1-2), 810-814.
110. Imamura, H.; Sakasai, N.; Kajii, Y., Hydrogen absorption of Mg-Based composites prepared by mechanical milling: Factors affecting its characteristics *Journal of Alloys and Compounds* **1996**, 232, (1-2), 218-223.
111. Imamura, H.; Sakasai, N.; Fujinaga, T., Characterization and hydriding properties of Mg-graphite composites prepared by mechanical grinding as new hydrogen storage materials. *Journal of Alloys and Compounds* **1997**, 253-254, 34-37.
112. Imamura, H.; Takesue, Y.; Tabata, S.; Shigetomi, N.; Sakata, Y.; Susumu Tsuchiya, Hydrogen storage composites obtained by mechanical grinding of magnesium with graphite carbon. *Chemical Communications* **1999**, (22), 2277-2278.
113. Imamura, H.; Takesue, Y.; Akimoto, T.; Tabata, S., Hydrogen-absorbing magnesium composites prepared by mechanical grinding with graphite: effects of additives on composite structures and hydriding properties. *Journal of Alloys and Compounds* **1999**, 293-295, 564-568.
114. Imamura, H.; Tabata, S.; Takesue, Y.; Sakata, Y.; Kamazaki, S., Hydriding-dehydriding behavior of magnesium composites obtained by mechanical grinding with graphite carbon. *International Journal of Hydrogen Energy* **2000**, 25, (9), 837-843.
115. Imamura, H.; Tabata, S.; Shigetomi, N.; Takesue, Y.; Sakata, Y., Composites for hydrogen storage by mechanical grinding of graphite carbon and magnesium. *Journal of Alloys and Compounds* **2002**, 330-332, 579-583.

116. Toè, S. D.; Russo, S. L.; Maddalena, A.; Principi, G.; Saber, A.; Sartori, S.; Spataru, T., Hydrogen desorption from magnesium hydride-graphite nanocomposites produced by ball milling. *Materials Science and Engineering B* **2004**, 108, (1-2), 24-27.
117. Wang, J.; Ebner, A. D.; Prozorov, T.; Zidan, R.; Ritter, J. A., Effect of graphite as a co-dopant on the dehydrogenation and hydrogenation kinetics of Ti-doped sodium sodium aluminum hydride. *Journal of Alloys and Compounds* **2005**, 395, 252-262.
118. Dehouche, Z.; Lafi, L.; Grimard, N.; Goyette, J.; Chahine, R., The catalytic effect of single-wall carbon nanotubes on the hydrogen sorption properties of sodium alanates. *Nanotechnology* **2005**, 16, 402-409.
119. Pukazhselvan, D.; Gupta, B. K.; Srivastava, A.; Srivastava, O. N., Investigations on hydrogen storage behavior of CNT doped NaAlH<sub>4</sub>. *Journal of Alloys and Compounds* **2005**, 403, (1-2), 312-317.
120. Jensen, F., *Introduction to Computational Chemistry*. 2nd ed.; John Wiley & Sons Ltd: West Sussex, England, 2007.
121. Goldstein, H.; Poole, C. P.; Safko, J. L., *Classical Mechanics*. 3rd Edition (Hardcover) ed.; Addison Wesley: 2001; p 680.
122. Koch, W.; Holthausen, M. C., *A Chemist's Guide to Density Functional Theory*. 2nd Edition ed.; Wiley-CVH: 2001.
123. Foreman, J.; Frisch, A., *Exploring Chemistry with Electronic Structure Methods*. Gaussian Inc.,: Pittsburg, PA.
124. Hohenberg, P.; Kohn, W., Inhomogeneous electron gas. *Physical Review* **1964**, 136, B864 - B871.
125. Kohn, W.; Sham, L. J., Self-Consistent Equations Including Exchange and Correlation Effects. *Physical Review* **1965**, 140, A1133-A1138.

126. Young, D. C., *Computational Chemistry: A practical Guide for Applying Techniques to Real-World Problems*. John Wiley & Sons, Inc.: 2001.
127. OpenCourseWare, 3.320 Atomistic Modeling of Materials, Massachusetts Institute of Technology (MIT), <http://ocw.mit.edu/3-320S05>. In 2005.
128. Ceperley, D. M.; Alder, B. J., Ground state of the electron gas by a stochastic method. *Physics Review Letters* **1980**, 45, 566-569.
129. Nogueira, F.; Castro, A.; Marques, M. A. L., A Tutorial on Density Functional Theory. In *A Primer in Density Functional Theory*, Springer-Verlag: Berlin Heidelberg, 2003; pp 218-256.
130. Fiolhais, C.; Fernando Nogueira; Marques, M. A. L., *A Primer in Density Functional Theory*. Springer-verlag: Berlin Heidelberg, 2003.
131. Vosko, S. H.; Wilk, L.; Nusair, M., Accurate spin-dependent electron liquid correlation energies for local spin density calculations: a critical analysis. *Canadian Journal of Physics* **1980**, 58, (8), 1200-1211.
132. Perdew, J. P.; Zunger, A., Self-interaction correction to density-functional approximations for many-electron systems. *Physical Review B* **1981**, 23, 5048-5079.
133. Becke, A. D., Density-functional exchange-energy approximation with correct asymptotic behavior. *Physical Review A* **1988**, 38, 3098-3100.
134. Lee, C.; Yang, W.; Parr, R. G., Development of the Colle-Salvetti correlation-energy formula into a functional of the electron density. *Physical Review B* **1988**, 37, 785-789.
135. Levy, M., In *The Single-Particle Density in Physics and Chemistry*, Hardcover ed.; March, N. H.; Deb, B. M., Eds. Academic Press: London, 1987; p 385.

136. Perdew, J. P.; Wang, Y., Accurate and simple analytic representation of the electron-gas correlation energy. *Physical Review B* **1992**, 45, 13244-13249.
137. Perdew, J. P.; Burke, K.; Ernzerhof, M., Generalized Gradient Approximation Made Simple. *Physics Review Letters* **1996**, 77, 3865-3868.
138. Becke, A. D., Density-functional thermochemistry. III. The role of exact exchange. *Journal Of Chemical Physics* **1993**, 98, (7), 5648.
139. Stephens, P. J.; Devlin, F. J.; Chabalowski, C. F.; Frisch, M. J., Ab Initio Calculation of Vibrational Absorption and Circular Dichroism Spectra Using Density Functional Force Fields. *Journal of Physical Chemistry* **1994**, 98, (45), 11623 - 11627.
140. Ashcroft, N. W.; Mermin, N. D., *Solid State Physics*. 1st Hardcover ed.; Brooks Cole.
141. Phillips, J. C., Energy-band interpolation scheme based on a pseudopotential. *Physical Review* **1958**, 112, 685-695.
142. Phillips, J. C.; Kleinman, L., New method for calculating wave functions in crystals and molecules. *Physical Review* **1959**, 116, 287-294.
143. Cohen, M. L.; Heine, V., The fitting of pseudopotentials to experimental data and their subsequent application. In *Solid State Physics*, Ehrenreich, H.; Seitz, F.; Turnbull, D., Eds. Academic Press: New York, 1970; Vol. 24, p 37.
144. Hamann, D. R.; Schlüter, M.; Chiang, C., Norm-conserving pseudopotentials. *Physics Review Letters* **1979**, 43, 1494-1497.
145. Bachelet, G. B.; Hamann, D. R.; Schlüter, M., Pseudopotentials that work: From H to Pu. *Physical Review B* **1982**, 26, 4199-4228.

146. Kerker, G. P., Non-singular atomic pseudopotentials for solid state applications. *Journal of Physics C: Solid State Physics* **1980**, 13, (9), L189-L194.
147. Vanderbilt, D., Soft self-consistent pseudopotentials in a generalized eigenvalue formalism. *Physical Review B* **1990**, 41, 7892-7895.
148. McQuarrie, D. A., *Statistical Mechanics*. 2nd ed.; University Science books: 2000.
149. Alder, B. J.; Wainwright, T. E., Phase transition for a hard sphere system. *Journal Of Chemical Physics* **1957**, 27, (5), 1208-1209.
150. Rahman, A., Correlations in the motions of atoms in liquid argon. *Physical Review* **1964**, 136A, 405-411.
151. Rahman, A.; Stillinger, F. H., Molecular dynamics study of liquid water. *Journal Of Chemical Physics* **1971**, 55, 3336-3359.
152. Deuffhard, P.; Hermans, J.; Leimkuhler, B.; Mark, A. E.; Reich, S.; Skeel, R. D., *Computational Molecular Dynamics: Challenges, Methods, Ideas*. Springer-Verlag: Berlin, 1997.
153. Allen, M. P.; Tildesley, D. J., *Computer Simulation of Liquids*. Oxford University press: New York, 1987.
154. Marx, D., An Introduction to Ab Initio Molecular Dynamics Simulations. In *Computational Nanoscience: Do it yourself*, Grotendorst, J.; Blugel, S.; Marx, D., Eds. John von Neumann Institute for Computing: Julich, 2006.
155. Iftimie, R.; Minary, P.; Tuckerman, M. E., *Ab initio molecular dynamics: Concepts, recent developments, and future trends*. *Proceedings of National Academy of Sciences* **2005**, 102, (19), 6654-6659.
156. Rafii-Tabar, H., Computational modelling of thermo-mechanical and transport properties of carbon nanotubes. *Physics Reports* **2004**, 390, 235-452.

157. Car, R.; Parrinello, M., Unified approach for molecular dynamics and density-functional theory. *Physical Review Letters* **1985**, 55, (22), 2471-2474.
158. Metropolis, N.; Rosenbluth, A. W.; Rosenbluth, M. N.; Teller, A. N.; Teller, E., Equation of state calculations by fast computing machines. *Journal Of Chemical Physics* **1953**, 21, 1087-1092.
159. Mainardi, D. S. Understanding the mechanisms of catalysis on mono- and bimetallic nanoparticles. University of South Carolina, 2003.
160. Metropolis, N., The beginning of the Monte Carlo method. *Los Alamos Science* **1987**, 12, 125-130.
161. Kumar, V.; Esfarjani, K.; Kawazoe, Y., *Clusters and Nanomaterials*. Springer-verlag: Berlin, 2002.
162. Jena, P.; Behera, S. N., *Clusters and Nanostructured Materials*. Nova Science: New York, 1996.
163. Pastor, G. M., Electronic properties of divalent-metal clusters. *Zeitschrift fur physik D - Atoms, Molecules and Clusters* **1991**, 19, 165-167.
164. Wang, J.; Wang, G.; Zhao, J., Density functional study of beryllium clusters, with gradient correction. *Journal of Physics: Condensed Matter* **2001**, 13, L753-L758.
165. Chen, M. D.; Li, X. B.; Yang, J.; Zhang, Q. E., A density functional study on beryllium-doped carbon dianion clusters  $C_nBe^{2-}$  ( $n = 4-14$ ). *Journal of Physical Chemistry A* **2006**, 110, 4502-4508.
166. Chen, M. D.; Li, X. B.; Yang, J.; Zhang, Q. E.; Au, C. T., Parity alternation in the linear ground-state beryllium-doped carbon clusters  $BeC_n^-$  ( $n = 1-8$ ). *International Journal of Mass Spectrometry* **2006**, 253, 30.
167. Zaluska, A.; Zaluski, L.; Ström-Olsen, J. O., Lithium-beryllium hydrides: the lightest reversible metal hydrides. *J. Alloys Compd.* **2000**, 307, 157-166.

168. Bondybey, V. E., Electronic structure and bonding of  $\text{Be}_2$ . *Chemical Physics Letters* **1984**, 109, (5), 436-441.
169. Bondybey, V. E.; English, J. H., Laser vaporization of beryllium: gas phase spectrum and molecular potential of  $\text{Be}_2$ . *Journal of Chemical Physics* **1984**, 80, (1), 568-570.
170. Kolchin, A. M.; Hall, R. W., Electronic properties of small neutral and charged beryllium clusters. *Journal of Chemical Physics* **2000**, 113, (10), 4083-4092.
171. Lee, T. J.; Rendell, A. P.; Taylor, P. R., Theoretical investigations of the structures and binding energies of  $\text{Be}_n$  and  $\text{Mg}_n$  ( $n=3-5$ ) clusters. *Journal of Chemical Physics* **1990**, 92, (1), 489-495.
172. Lengsfeld, B. H.; McLean, A. D.; Yoshimine, M.; Liu, B., The binding energy of the ground state of  $\text{Be}_2$ . *Journal of Chemical Physics* **1983**, 79, (4), 1891.
173. Harrison, R. J.; Handy, N. C., Full CI results for  $\text{Be}_2$  and  $(\text{H}_2)_2$  in large basis sets. *Chemical Physics Letters* **1983**, 98, 97-101.
174. Sosa, C.; Noga, J.; Barlett, R. J., A study of the  $\text{Be}_2$  potential curve using the full (CCSDT) coupled-cluster method: The importance of  $T_4$  clusters. *Journal of Chemical Physics* **1988**, 88, 5974-5976.
175. Harrison, R. J.; Handy, N. C., The binding energies of small Be clusters *Chemical Physics Letters* **1986**, 123, 321-326.
176. Beyer, M. K.; Kaledin, L. A.; Kaledin, A. L.; Heaven, M. C.; Bondybey, V. E., Density functional calculations of beryllium clusters  $\text{Be}_n$ ,  $n=2-8$ . *Chemical Physics* **2000**, 262, 15-23.
177. Srinivas, S.; Jellinek, J., Structural and electronic properties of small beryllium clusters: A theoretical study. *Journal of Chemical Physics* **2004**, 121, (15), 7243-7252.

178. Cerowski, V.; Rao, B. K.; Khanna, S. N.; Jena, P.; Ishil, S.; Ohno, K.; Kawazoe, Y., Evolution of the electronic structure of Be Clusters. *Journal of Chemical Physics* **2005**, 123.
179. Pecul, M.; Jaszunski, M.; Larsen, H.; Jorgensen, P., Singlet excited states of Be<sub>2</sub>. *Journal of Chemical Physics* **2000**, 112, (8), 3671-3679.
180. Klopper, W.; Almlöf, J., Towards the one-particle basis set limit of second-order correlation energies: MP2-R12 calculations on small Be<sub>n</sub> and Mg<sub>n</sub> clusters (n=1-4). *Journal of Chemical Physics* **1993**, 99, (7), 5167-5177.
181. Kaplan, I. G.; Roszak, S.; Leszczynski, J., Nature of binding in the alkaline-earth clusters: Be<sub>3</sub>, Mg<sub>3</sub>, and Ca<sub>3</sub>. *Journal of Chemical Physics* **2000**, 113, 6245-6252.
182. Murray, C. W.; Handy, N. C.; Amos, R. D., A study of O<sub>3</sub>, S<sub>3</sub>, CH<sub>2</sub>, and Be<sub>2</sub> using Kohn-Sham theory with accurate quadrature and large basis sets. *Journal of Chemical Physics* **1993**, 98, 7145.
183. Kawai, R.; Weare, J. H., From Vander waals to metallic bonding: the growth of Be clusters. *Physical Review Letters* **1990**, 65, (1), 80-83.
184. Khanna, S. N.; Reuse, F.; Buttet, J., Stability and observability of charged beryllium clusters. *Physical Review Letters* **1988**, 61, (5), 535-539.
185. Blaisten-Barojas, E.; Khanna, S. N., Development of a first-principles many-body potential for beryllium. *Physical Review Letters* **1988**, 61, (13), 1477-1480.
186. Foresman, J. B.; Head-Gordon, M.; Pople, J. A.; Frisch, M. J., Toward a systematic molecular orbital theory for excited states. *Journal of Physical Chemistry* **1992**, 96, (1), 135-149.
187. Pople, J. A.; Head-Gordon, M.; Raghavachari, K., Quadratic configuration interaction. A general technique for determining electron correlation energies. *Journal of Chemical Physics* **1987**, 87, 5968.



188. Møller, C.; Plesset, M. S., Note on an Approximation Treatment for Many-Electron Systems. *Physical Review* **1934**, 46, (7), 618-622.
189. Sudhakar, P. V.; Lammertsma, K., Bond Properties of Be<sub>3-7</sub> clusters. *Journal of Chemical Physics* **1993**, 99, (10), 7929-7937.
190. Pople, J. A.; Krishnan, R.; Schlegel, H. B.; Binkley, J. S., Electron correlation theories and their application to the study of simple reaction potential surfaces. *International Journal of Quantum Chemistry* **1978**, 14, (5), 545-560.
191. Oritz, G.; Ballone, P., Bonding properties of IIA and IIB dimers in density functional theory with gradient corrections to the local density approximation *Zeitschrift für Physik D Atoms, Molecules and Clusters* **1991**, 19, 169-171.
192. Marino, M. M.; Ermler, W. C., Electronic states and geometries of small Be clusters. *Journal of Chemical Physics* **1987**, 86, 6283-6294.
193. Song, B.; Yao, C.-H.; Cao, P.-l., Density-functional study of structural and electronic properties of Ga<sub>n</sub>N (*n*=1-19) clusters. *Physical Review B* **2006**, 74, (035306).
194. deHeer, W. A.; Knight, W. D.; Chou, M. Y.; Cohen, M. L., Electronic shell structure and metal clusters. *Solid State Physics* **1987**, 40, 94.

195. Frisch, M. J.; Trucks, G. W.; Schlegel, H. B.; Scuseria, G. E.; Robb, M. A.; Cheeseman, J. R.; Montgomery Jr, J. A.; Vreven, T.; K. N. Kudin; J. C. Burant; J. M. Millam; S. S. Iyengar; J. Tomasi; V. Barone; B. Mennucci; M. Cossi; G. Scalmani; N. Rega; G. A. Petersson; H. Nakatsuji; M. Hada; M. Ehara; K. Toyota; R. Fukuda; J. Hasegawa; M. Ishida; T. Nakajima; Y. Honda; O. Kitao; H. Nakai; M. Klene; X. Li; J. E. Knox; H. P. Hratchian; J. B. Cross; C. Adamo; J. Jaramillo; R. Gomperts; R. E. Stratmann; O. Yazyev; A. J. Austin; R. Cammi; C. Pomelli; J. W. Ochterski; P. Y. Ayala; K. Morokuma; G. A. Voth; P. Salvador; J. J. Dannenberg; V. G. Zakrzewski; S. Dapprich; A. D. Daniels; M. C. Strain; O. Farkas; D. K. Malick; A. D. Rabuck; K. Raghavachari; J. B. Foresman; J. V. Ortiz; Q. Cui; A. G. Baboul; S. Clifford; J. Cioslowski; B. B. Stefanov; G. Liu; A. Liashenko; P. Piskorz; I. Komaromi; R. L. Martin; D. J. Fox; T. Keith; M. A. Al-Laham; C. Y. Peng; A. Nanayakkara; M. Challacombe; P. M. W. Gill; B. Johnson; W. Chen; M. W. Wong; C. Gonzalez; Pople, J. A. *Gaussian 03, Revision C.02*, Gaussian, Inc: Wallingford, CT, 2004.
196. Seminario, J. M., *Recent Developments and Applications of Modern Density Functional Theory*. Elsevier Science Publishers: Amsterdam, 1996; Vol. 4.
197. Zhao, Y.; Li, N.; Xu, W. G.; Li, Q. S., Structure and stability of  $\text{Be}_5$ ,  $\text{Be}_5^+$ , and  $\text{Be}_5^-$  clusters. *Journal of Physical Chemistry A* **2004**, 108, 4887-4894.
198. Zhao, Y.; Li, N.; Xu, W. G.; Li, Q. S., Structure and stability of  $\text{Be}_6$ ,  $\text{Be}_6^+$ , and  $\text{Be}_6^-$  clusters. *International Journal of Quantum Chemistry* **2007**, 107, 81-91.
199. Pacchioni, G.; Koutecký, J., On the nature of the bonding in  $\text{Mg}_4$  and  $\text{Ca}_4$  clusters. *Journal of Chemical Physics* **1982**, 77, (11), 5850-5851.
200. Moore, C. *Atomic Energy Levels*; National Bureau of Standards, US: 1971; p 35/V.I.
201. Tozer, D. J.; Handy, N. C., On the determination of excitation energies using density functional theory. *Physical Chemistry Chemical Physics* **2000**, 2, 2117-2121.

202. Knight, W. D.; Clemenger, K.; deHeer, W. A.; Saunders, W. A.; Chou, M. Y.; Cohen, M. L., Electronic shell structure and abundances of sodium clusters. *Physical Review Letters* **1984**, 52, (24), 2141-2143.
203. Ge, G.-x.; Yan, Y.-l.; Ren, F.-z.; Lei, X.-l.; Yang, Z.; Zhao, W.-j.; Wang, Q.-l.; Luo, Y.-h., Density functional theory study of structure and electronic properties of  $\text{MgBe}_n$  ( $n=2-12$ ) clusters. *Chinese Journal of Chemical Physics* **2007**, 20, (5), 518-524.
204. Kumar, V.; Esfarjani, K.; Kawazoe, Y., *Clusters and Nanomaterials*. Springer-verlag: Berlin, 2002.
205. Alonso, J. A., Electronic and atomic structure, and magnetism of transition-metal clusters. *Chemical Reviews* **2000**, 100, (2), 637-678.
206. Alonso, J. A., *Structure and Properties of Atomic Nanoclusters*. Imperial College Press London, 2006.
207. Borg, X. *Magic numbers derived from variable phase nuclear model*; Blaze Labs Research: 2006.
208. Pradhan, P.; Ray, A. K., A density functional study of the structure and energetics of small hetero-atomic silicon-carbon nanoclusters. *Journal of Molecular Structure* **2004**, 716, (1-3), 109-130.
209. Mainardi, D. S.; Balbuena, P. B., Monte Carlo simulation of Cu-Ni nanoclusters: surface segregation studies. *Langmuir* **2001**, 17, (6), 2047-2050.
210. Mainardi, D. S.; Balbuena, P. B., Surface segregation in bimetallic nanoclusters: geometric and thermodynamic effects. *International Journal of Quantum Chemistry* **2001**, 85, (4/5), 580-591.
211. Mainardi, D. S.; Balbuena, P. B., Hydrogen and oxygen adsorption on  $\text{Rh}_n$  ( $n = 1 - 6$ ) clusters. *Journal of Physical Chemistry A* **2003**, 107, (48), 10370-10380

212. Derosa, P. A.; Seminario, J. M.; Balbuena, P. B., Properties of small bimetallic Ni-Cu clusters. *Journal of Physical Chemistry A* **2001**, 105, (33), 7917 - 7925.
213. Balbuena, P. B.; Derosa, P. A.; Seminario, J. M., Density functional theory study of copper clusters. *Journal of Physical Chemistry B* **1999**, 103, (15), 2830 - 2839.
214. Gong, X. G., Structure and stability of cluster-assembled solid  $\text{Al}_{12}\text{C}(\text{Si})$ : A first-principles study. *Physical Review B* **1997**, 56, 1091-1094.
215. Gong, X. G.; Kumar, V., Enhanced stability of magic clusters: A case study of icosahedral  $\text{Al}_{12}\text{X}$ , X=B, Al, Ga, C, Si, Ge, Ti, As. *Physics Review Letters* **1993**, 70, 2078-2081.
216. Gong, X. G.; Kumar, V., Electronic structure and relative stability of icosahedral Al-transition-metal clusters. *Physical Review B* **1994**, 50, 17701-17704.
217. Khanna, S. N.; Jena, P., Assembling crystals from clusters. *Physical Review Letters* **1992**, 69, (11), 1664-1667.
218. Kumar, V.; Bhattacharjee, S.; Kawazoe, Y., Silicon-doped icosahedral, cuboctahedral, and decahedral clusters of aluminum. *Physical Review B* **2000**, 61, (12), 8541-8547.
219. Kumar, V.; Kawazoe, Y., Hund's rule in metal clusters: Prediction of high magnetic moment state of  $\text{Al}_{12}\text{Cu}$  from first-principles calculations. *Physical Review B* **2001**, 64, (11), 115405-115410.
220. Kumar, V.; Sundararajan, V., Ab initio molecular-dynamics studies of doped magic clusters and their interaction with atoms. *Physical Review B* **1998**, 57, (8), 4939-4942.
221. Seitsonen, A. P.; Laasonen, K.; Nieminen, R. M.; Klein, M. L., Structure of  $\text{CaAl}_{12}$ . *Journal of Chemical Physics* **1995**, 103, 8075-8080.

222. Seitsonen, A. P.; Puska, M. J.; Alatalo, M.; Nieminen, R. M.; Milman, V.; Payne, M. C., Crystals from metallic clusters: A first-principles calculation. *Physical Review B* **1993**, 48, (3), 1981-1983.
223. Rohmer, M.; Wiemann, C.; Munzinger, M.; Guo, L.; Aeschlimann, M.; Bauer, M., Local correlation of photoemission electron microscopy and STM at a defined cluster substrate system. *Applied Physics A* **2005**, 82, (1), 87-93.
224. Ebehardt, W.; Fayet, P.; Cox, D.; Fu, Z.; Kaldor, A.; Sondericker, D., Core level photoemission from monosize mass selected Pt clusters deposited on SiO<sub>2</sub> and amorphous carbon. *Physica Scripta* **1990**, 41, (6), 892-895.
225. Wang, L. S.; Niu, B.; Lee, Y. T.; Shirley, D. A., High resolution photoelectron spectroscopy of clusters of group V elements. *Physica Scripta* **1990**, 41, 867-869.
226. Cheshnovsky, O.; Uang, S. H.; Pettiette, C. C.; Craycraft, M. J.; Smalley, R. E., Magnetic time-of-flight photoelectron spectrometer for mass-selected negative cluster ions. *Review of Scientific Instruments* **1987**, 58, 2131-2137.
227. Ervin, K. M.; Ho, J.; Lineberger, W. C., Electronic and vibrational structure of transition metal trimers: Photoelectron spectra of Ni<sub>3</sub><sup>-</sup>, Pd<sub>3</sub><sup>-</sup> and Pt<sub>3</sub><sup>-</sup>. *Journal of Chemical Physics* **1988**, 89, 4514-4521.
228. Akola, J.; Manninen, M.; Hakkinen, H.; Landman, U.; Li, X.; Wang, L. S., Photoelectron spectra of aluminum cluster anions: Temperature effects and *ab initio* simulations. *Physical Review B* **2000**, 62, 13216-13228.
229. Knickelbein, M. B., Reactions of transition metal clusters with small molecules. *Annual Review of Physical Chemistry* **1999**, 115, 50-79.
230. Nakatsuji, N.; Nakai, H.; Hada, M., Catalytic Reactions of Transition Metal Clusters and Surfaces from Ab Initio Theory. In *Metal-Ligand Interactions: from Atoms, to Clusters, to Surfaces*, Salahub, D. R.; Russo, N., Eds. Kluwer Academic: Dordrecht, The Netherlands, 1992; p 251.

231. Tomanek, D.; Schulter, M. A., Growth Regimes of Carbon Clusters. *Physical Review Letters* **1991**, 67, (17), 2331-2334.
232. Ray, A. K., A Hartree-Fock Study of Carbon Clusters. *Journal of Physics B: Atomic and Molecular Physics* **1987**, 20, (19), 5233-5239.
233. Martin, J. M. L., Accurate *ab initio* total atomization energies of the  $C_n$  clusters ( $n=2-10$ ). *Journal of Chemical Physics* **1995**, 102, (20), 8270-8273.
234. Raghavachari, K.; Binkley, J. S., Structure, stability, and fragmentation of small carbon clusters. *Journal of Chemical Physics* **1987**, 87, (4), 2191-2197.
235. Martin, J. M. L.; Francois, J. P.; Gijbels, R., On the heat of formation of  $C_5$  and higher carbon clusters. *Journal of Chemical Physics* **1991**, 95, (12), 9420-9421.
236. Jones, R. O.; Seifert, G., Structure and bonding in carbon clusters  $C_{14}$  to  $C_{24}$ : chains, rings, bowls, plates, and cages. *Physical Review Letters* **1997**, 79, (3), 443-446.
237. Jones, R. O., Density functional study of carbon clusters  $C_{2n}$  ( $2 < n < 16$ ). I. Structure and bonding in the neutral clusters. *Journal of Chemical Physics* **1999**, 110, (11), 5189-5200.
238. Martin, J. M. L.; Taylor, P. R., Structure and vibrations of small carbon clusters from coupled-cluster calculations. *Journal of Physical Chemistry A* **1996**, 100, 6047-6056.
239. Joswig, J. O.; Springborg, M.; Seifert, G., Structural and electronic properties of small titanium-carbon clusters (metcars). *Physical Chemistry Chemical Physics* **2001**, 3, 5130-5134.
240. Belbruno, J. J.; Tang, Z. C.; Smith, R.; Hobday, S., The structure and energetics of carbon-nitrogen clusters. *Molecular Physics* **2001**, 99, (11), 957-967.

241. Duncan, M. A., Synthesis and characterization of metal-carbide clusters in the gas phase. *Journal of Cluster Sciences* **1997**, 8, (2), 239-266.
242. Sun, S.; Cao, Y.; Sun, Z.; Tang, Z.; Zheng, L., Experimental and theoretical studies on carbon-nitrogen clusters  $C_{2n}N_7^-$ . *Journal of Physical Chemistry A* **2006**, 110, 8064-8072.
243. Largo, A.; Redondo, P.; Barrientos, C., Theoretical study of  $AlC_n$ ,  $AlC_n^+$ , and  $AlC_n^-$  ( $n = 1-7$ ) clusters. *Journal of Physical Chemistry A* **2002**, 106, (16), 4217-4225.
244. Presilla-Márquez, J. D.; Graham, W. R. M., Vibrational spectra of penta-atomic silicon-carbon clusters. II. linear  $Si_2C_3$  *Journal of Chemical Physics* **1994**, 100, (1), 181-185.
245. Zhang, C., A theoretical study of structure and stability of dianions  $BeC_{2n}^{2-}$  ( $n=2-6$ ). *Journal of Molecular Structure* **2006**, 759, 201-207.
246. Klein, J.; Middleton, R., Observation of  $BeC^{2-n}$ , a particularly abundant gaseous dianion. *Nuclear Instruments and Methods in Physics Research B* **1999**, 159, (1-2), 8-21.
247. Guo, B. C.; Kerns, K. P.; Castleman Jr., A. W.,  $Ti_8C^{12+}$ -Metallo-Carbohedrenes: A new class of molecular clusters? *Science* **1992**, 255, (5050), 1411-1413.
248. Guo, B. C.; Wei, S.; Purnell, J.; Buzza, S.; Castleman Jr., A. W., Metallo-Carbohedrenes [ $M_8C^{12+}$  ( $M = V, Zr, Hf,$  and  $Ti$ )]: A class of stable molecular cluster Ions. *Science* **1992**, 256, (5056), 515-516.
249. Wei, S.; Guo, B. C.; Purnell, J.; Buzza, S.; Castleman Jr., A. W., Metallo-Carbohedrenes: formation of multicage structures. *Science* **1992**, 256, (5058), 818-820.
250. Qiao-yan, C.; Bao-xing, L.; Jian, Y., Stability of carbon-doped silicon clusters: FP-LMTO molecular dynamics calculation. *Journal of Molecular Structure* **2007**, 806, (1-3), 67-76.

251. Millar, T. J.; Leung, C. M.; Herbst, E., How abundant are complex interstellar molecules? *Astronomy and Astrophysics* **1987**, 183, (1), 109-117.
252. Kroto, H. W.; Heath, J. R.; O'Brien, S. C.; Curl, R. F.; Smalley, R. E., C-60 - Buckminsterfullerene. *Nature* **1985**, 318, (162-163).
253. Schimmel, H. G.; Kearley, G. J.; Nijkamp, M. G.; Visser, C. T.; De Jong, K. P.; Mulder, F. M., Hydrogen adsorption in carbon nanostructures: comparison of nanotubes, fibers, and coals. *Chemistry - A European Journal* **2003**, 9, (19), 4764-4770.
254. Türker, L., AM1 treatment of  $(\text{Li}+\text{nH}_2)\text{n}=0-5@C60$  systems. *International Journal of Hydrogen Energy* **2003**, 28, (2), 223-228.
255. Türker, L., Hydrogen storage capacity of Be@C115 system. *Journal of Molecular Structure* **2005**, 723, 105-110.
256. Zhu, Z. H.; Lu, G. Q.; Smith, S. C., Comparative study of hydrogen storage in Li- and K-doped carbon materials--theoretically revisited. *Carbon* **2004**, 42, 2509-2514.
257. Viswanathan, B.; Sankaran, M.; Scibioh, M. A., Carbon nanomaterials - are they appropriate candidates for hydrogen storage? *Bulletin of the Catalysis Society of India* **2003**, 2, 12-32.
258. Türker, L.; Gümüs, S., Hydrogen storage capacity of Mg@C120 system. *Journal of Molecular Structure* **2005**, 719, 103-107.
259. Türker, L.; Eroglu, I.; Yucel, M.; Gunduz, U., Hydrogen storage capability of carbon nanotube Be@C120. *International Journal of Hydrogen Energy* **2004**, 29, 1643-1647.
260. Zaluska, A.; Zaluski, L.; Ström-Olsen, J. O., Lithium-beryllium hydrides: the lightest reversible metal hydrides. *Journal of Alloys and Compounds* **2000**, 307, 157-166.



261. Ghouri, M. M.; Yareeda, L.; Mainardi, D. S., Geometry and stability of  $\text{Be}_n\text{C}_m$  ( $n = 1-10$ ;  $m = 1, 2, \dots$ , to  $11 - n$ ) clusters. *Journal of Physical Chemistry A* **2007**, 111, (50), 13133-13147.
262. Song, B.; Yao, C. H.; Cao, P. L., Density-functional study of structural and electronic properties of  $\text{Ga}_n\text{N}$  ( $n=1-19$ ) clusters. *Phys. Rev. B* **2006**, 74, (035306).
263. Accelrys Software Inc. *Materials Studio*®, version 4.2; San Diego, CA, 2006.
264. Woolf, H.; Brown, I.; Bowden, M., Light metal hydrides - Potential hydrogen storage materials. *Current Applied Physics* **2008**, 8, 459-462.
265. Bogdanovic, B.; Schwickardi, M., Ti-doped alkali metal aluminium hydrides as potential novel reversible hydrogen storage materials. *Journal of Alloys and Compounds* **1997**, 253, 1-9.
266. Anton, D. L., Hydrogen desorption kinetics in transition metal modified  $\text{NaAlH}_4$ . *Journal of Alloys and Compounds* **2003**, 356-357, 400-404.
267. Jensen, C. M.; Gross, K. J., Development of catalytically enhanced sodium aluminum hydride as a hydrogen-storage material *Applied Physics A: Materials Science & Processing* **2001**, 72, (2), 213-219.
268. Meisner, G. P.; Tibbetts, G. G.; Pinkerton, F. E.; Olk, C. H.; Balogh, M. P., Enhancing low pressure hydrogen storage in sodium alanates. *Journal of Alloys and Compounds* **2002**, 337, (1-2), 254-263.
269. Sandrock, G.; Reilly, J.; Graetz, J.; Zhou, W.-M.; Johnson, J.; Wegrzyn, J., Alkali metal hydride doping of  $\alpha\text{-AlH}_3$  for enhanced  $\text{H}_2$  desorption kinetics. *Journal of Alloys and Compounds* **2006**, 421, (1-2), 185-189.
270. Morioka, H.; Kakizaki, K.; Chung, S.-C.; Yamada, A., Reversible hydrogen decomposition of  $\text{KAlH}_4$ . *Journal of Alloys and Compounds* **2003**, 353, (1-2), 310-314.

271. Dompablo, M. E. A. y. d.; Ceder, G., First principles investigations of complex hydrides  $AMH_4$  and  $A_3MH_6$  (A=Li, Na, K, M=B, Al, Ga) as hydrogen storage systems. *Journal of Alloys and Compounds* **2004**, 364, (1-2), 6-12.

272. Zaluska, A.; Zaluski, L.; Ström-Olsen, J. O., Sodium alanates for reversible hydrogen storage *Journal of Alloys and Compounds* **2000**, 298, (1-2), 125-134.

273. Bell, N. A.; Coates, G. E., Lithium and sodium beryllium hydrides. *Journal of the Chemical Society A* **1968**, 1968, 628-631.

274. Ashby, E. C.; Prasad, H. S., Alkali metal ate complexes and complex metal hydrides of beryllium. *Inorganic Chemistry* **1975**, 14, (12), 2869-2874.

275. Overhauser, A. W., Crystal structure of lithium beryllium hydride *Physical Review B* **1987**, 35, 411-414.

276. Selvam, P.; Yvon, K., Comment on "Crystal structure of lithium beryllium hydride". *Physical Review B* **1989**, 39, 12329-12330.

277. Cantrell, J. S.; Beiter, T. A.; Souers, P. C.; Barry, P., Crystallographic studies of compounds from the  $LiH+BeH_2$  system. *Journal of the Less Common Metals* **1991**, 172-174, (1), 213-219.

278. Bulychev, B. M.; Shpanchenko, R. V.; Antipov, E. V.; Sheptyakov, D. V.; Bushmeleva, S. N.; Balagurov, A. M., Synthesis and crystal structure of lithium beryllium deuteride  $Li_2BeD_4$ . *Inorganic Chemistry* **2004**, 43, 6371-6376.

279. Segall, M. D.; Lindan, P. J. D.; Probert, M. J.; Pickard, C. J.; Hasnip, P. J.; Clark, S. J.; Payne, M. C., First-principles simulation: ideas, illustrations and the CASTEP code. *Journal of Physics: Condensed Matter* **2002**, 14, (11), 2717-2744.

280. Vanderbilt, D. Vanderbilt Ultra-Soft Pseudopotential Site. <http://www.physics.rutgers.edu/~dhv/uspp/> (September 23, 2008.),

281. Mulliken, R. S., Electronic population analysis on LCAO-MO molecular wave functions. *Journal of Chemical Physics* **1955**, 10, 1833-1840.
282. Segall, M. D.; Pickard, C. J.; Shah, R.; Payne, M. C., Population analysis in plane wave electronic structure calculations. *Molecular Physics* **1996**, 89, 571-577
283. Segall, M. D.; Shah, R.; Pickard, C. J.; Payne, M. C., Population analysis of plane-wave electronic structure calculations of bulk materials. *Physical Review B* **1996**, 54, 16317-16320.
284. Sanchez-Portal, D.; Artacho, E.; Soler, J. M., Projection of plane-wave calculations into atomic orbitals. *Solid State Communication* **1995**, 95, 685-690.
285. Winkler, B.; Pickard, C. J.; Segall, M. D.; Milman, V., Density functional study of charge ordering in Cs<sub>2</sub>Au(I)Au(III)Cl<sub>6</sub> under pressure. *Physical Review B* **2001**, 63, 14103.
286. Wiberg, N.; Holleman, A. F.; Wiberg, E., *Inorganic Chemistry*. 1 ed.; Academic Press: San Diego, 2001.
287. Cento, C.; Gilson, P.; Bilgili, M.; Masci, A.; Zheng, Q.; Prosini, P. P., How carbon affects hydrogen desorption in NaAlH<sub>4</sub> and Ti-doped NaAlH<sub>4</sub>. *Journal of Alloys and Compounds* **2007**, 437, 360-366.
288. Aiello, R.; Matthews, M. A.; Reger, D. L.; Collins, J. E., Production of hydrogen gas from novel chemical hydrides. *International Journal of Hydrogen Energy* **1998**, 23, (12), 1103-1108.
289. Bogdanovic', B.; Schwickardi, M., Ti-doped alkali metal aluminium hydrides as potential novel reversible hydrogen storage materials. *Journal of Alloys and Compounds* **1997**, 253, 1-9.
290. Zaluski, L.; Zaluska, A.; Ström-Olsen, J. O., Hydrogenation properties of complex alkali metal hydrides fabricated by mechano-chemical synthesis. *Journal of Alloys and Compounds* **1999**, 290, (1), 71-78.

291. Hauback, B. C.; Brinks, H. W.; Fjellvåg, H., Accurate structure of LiAlD<sub>4</sub> studied by combined powder neutron and X-ray diffraction. *Journal of Alloys and Compounds* **2002**, 346, (1-2), 184-189.
292. Balema, V. P.; Dennis, K. W.; Pecharsky, V. K., Rapid solid-state transformation of tetrahedral [AlH<sub>4</sub>]<sup>-</sup> into octahedral [AlH<sub>6</sub>]<sub>3</sub><sup>-</sup> in lithium aluminohydride *Chemical Communications* **2000**, 1669.
293. Balema, V. P.; Pecharsky, V. K.; Dennis, K. W., Solid state phase transformations in LiAlH<sub>4</sub> during high-energy ball-milling. *Journal of Alloys and Compounds* **2000**, 313, 69-74.
294. Chen, J.; Kuriyama, N.; Xu, Q.; Takeshita, H. T.; Sakai, T., Reversible hydrogen storage via titanium-catalyzed LiAlH<sub>4</sub> and Li<sub>3</sub>AlH<sub>6</sub>. *Journal of Physical Chemistry B* **2001**, 105, (45), 11214-11220.
295. Balema, V. P.; Wiench, J. W.; Dennis, K. W.; Pruski, M.; Pecharsky, V. K., Titanium catalyzed solid-state transformations in LiAlH<sub>4</sub> during high-energy ball-milling. *Journal of Alloys and Compounds* **2001**, 329, 108-114.
296. Fakioglu, E.; Yürüm, Y.; Veziroglu, T. N., A review of hydrogen storage systems based on boron and its compounds. *International Journal of Hydrogen Energy* **2004**, 29, (13), 1371-1376.
297. Schlesinger, H. I.; Brown, H. C., Metallo borohydrides. III. lithium borohydride. *Journal of American Chemical Society* **1940**, 62, 3429-3435.
298. Züttel, A.; Rentsch, S.; Fischer, P.; Wenger, P.; Sudan, P.; Mauron, P.; Emmenegger, C., Hydrogen storage properties of LiBH<sub>4</sub>. *Journal of Alloys and Compounds* **2003**, 356, 515-520.
299. Züttel, A.; Wenger, P.; Rentsch, S.; Sudan, P.; Mauron, P.; Emmenegger, C., LiBH<sub>4</sub> a new hydrogen storage material. *Journal of Power Sources* **2003**, 118, 1-7.

300. Wang, P.-J.; Fang, Z.-Z.; Ma, L.-P.; Kang, X.-D.; Wang, P., Effect of SWNTs on the reversible hydrogen storage properties of  $\text{LiBH}_4\text{-MgH}_2$  composite. *International Journal of Hydrogen Energy* **2008**, Article In Press.
301. Grochala, W.; Edwards, P. P., Thermal decomposition of the non-interstitial hydrides for the storage and production of hydrogen. *Chemical Reviews* **2004**, 104, 1283 - 1316.
302. Aiello, R.; Sharp, J. H.; Matthews, M. A., Production of hydrogen from chemical hydrides via hydrolysis with steam. *International Journal of Hydrogen Energy* **1999**, 24, (12), 1123-1130.
303. Amendola, S. C.; Sharp-Goldman, S. L.; Janjua, M. S.; Spencer, N. C.; Kelly, M. T.; Petillo, P. J.; Binder, M., A safe, portable, hydrogen gas generator using aqueous borohydride solution and Ru catalyst. *International Journal of Hydrogen Energy* **2000**, 25, (10), 969-975.
304. Amendola, S. C.; Sharp-Goldman, S. L.; Janjua, M. S.; Spencer, N. C.; Kelly, M. T.; Petillo, P. J.; Binder, M., An ultrasafe hydrogen generator: aqueous, alkaline borohydride solutions and Ru catalyst. *Journal of Power Sources* **2000**, 85, (5), 186-189.
305. Soulié, J.-P.; Renaudin, G.; Cerný, R.; Yvon, K., Lithium boro-hydride  $\text{LiBH}_4$ : I. Crystal structure *Journal of Alloys and Compounds* **2002**, 346, (1-2), 200-205.
306. Fischer, P.; Zuttel, A., Order-Disorder Phase Transition in  $\text{NaBD}_4$ . *Materials Science Forum* **2004**, 443-444, 287-290.
307. Chase, M. W.; (U.S.), N. I. o. S. a. T., NIST-JANAF Thermochemical Tables. In American Institute of Physics: 1998.
308. Vajeeston, P.; Ravindran, P.; Vidya, R.; Fjellvag, H.; Kjekshus, A., Design of Potential Hydrogen-Storage Materials Using First-Principle Density-Functional Calculations. *Crystal Growth & Design* **2004**, 4, (3), 471-477.